A Thesis Submitted for the Degree of

Doctor of Philosophy (Ph.D.)

Speciality : Mechanics

Prepared at Process and Material Sciences Laboratory (LSPM)

Large plastic deformation of crystals : stability analysis and attractors

PhD candidate : Jalal SMIRI

PhD thesis to be defended on the December 19th 2024 before a jury composed of :

Referees

Bilen Emek ABALI	Uppsala University, Sweden
Fabrice RICHARD	Franche-Comté University, France

Examination Committee

Aylin AHADI	Lund University, Sweden
Maurine MONTAGNAT	Grenoble University, France
Joseph PAUX	Sorbonne Paris Nord University, France

Thesis Adviser and Co-Adviser

Ioan R IONESCU	Sorbonne Paris Nord University, France
Oguz Umut SALMAN	Sorbonne Paris Nord University, France

Declaration

Author's declaration: aware of legal responsibility I hereby declare that I have written this dissertation myself and all the contents of the dissertation have been obtained by legal means.

Abstract

This thesis focuses on employing Crystal Plasticity (CP) models to study the microstructural evolution in mono- and polycrystalline materials under extreme loading conditions associated with large deformations. CP provides a powerful tool to model dislocation interactions, lattice rotation, void growth, and size-dependent effects, offering insights into critical deformation mechanisms such as strain localization, shear band formation, and void evolution. By adopting an Eulerian framework, this work overcomes the challenges of mesh distortion in traditional methods, allowing accurate simulations of large deformations. High-resolution CP simulations achieved through a re-meshing technique, are used to explore the role of dislocation density and lattice orientation attractors, as well as the mechanisms behind void growth and shape evolution during deformation.

The prediction of attractors for lattice orientations in velocity gradient process is of great interest in understating the final texture of a poly-crystal. We have done a stability analysis of a simpler problem (2-D with 3 slip systems) in order to developed a theoretical strategy able to predict the lattice orientations attractors for large strains. Two numerical simulations illustrate the theory: deformation of a poly-crystal under a homogeneous velocity gradient loading and the void evolution of a mono-crystal under a non-homogeneous velocity gradient loading.

We have developed a stability analysis of slip rate driven processes for some established dislocation density-based models, including the Kocks and Mecking (KM) model and its variants, aiming to identify conditions for stationary states in active slip systems and evaluate their linear stability. Our analysis can be generalized to any type of dislocation density model, providing a broader framework for understanding the stability of such systems. Interestingly, from a size independent model we uncover size-dependent effects manifesting through initial dislocation density variations, particularly in FIB-prepared samples, influencing the material's softening or hardening responses. Some numerical simulations of micro-pillar compression

have been performed to address the behavior of materials at nano-scale dimensions.

The mechanisms of void growth and coalescence are key contributors to the ductile failure of crystalline materials, occurring through large plastic flow around pre-existing voids or nucleated cavities at second-phase particles. The main goal is to analyze growth of flat voids in single crystals (HCP, FCC) using Eulerian deformation crystal plasticity finite element simulations to better understand the void growth. The proposed model not only captures the onset of yielding but also accurately predicts the evolution of void shapes. The model is applied to experimental studies, which observed that an initially circular void in an HCP crystal evolves into a polyhedral cavity in a radial loading. Two processes are studied: radial loading applied on a hexagonal close-packed (HCP) crystal, and tensile loading on a face-centered cubic (FCC) crystal. These cases illustrate the model's capability in different crystallographic structures and loading conditions, thereby demonstrating its broader applicability.

Finally, we derive some formulas for calculating true stress in cases where slip/kink bands form during mechanical loading in compression experiments on pillars. Specifically, we consider a localization, observed frequently in experiments as single band oriented in arbitrary directions with respect to the vertical axis of the pillar, for which we derive a formula and employ it to assess the reliability of previous experimental results. These formulas are very simple and need only the engineering stress data, some geometric data (aspect ratio), and some mechanical data (elastic limit) which are very simple to get from the experimental results. They provide a valuable tool for accurately interpreting the mechanical behavior of materials under compressive loads and for drawing appropriate conclusions based on the true stress values.

Résumé en français

Cette thèse porte sur l'utilisation de modèles de plasticité cristalline (PC) pour étudier l'évolution microstructurale des matériaux mono- et polycristallins soumis à des conditions de chargement extrêmes associées à de grandes déformations. La plasticité cristalline constitue un outil puissant pour modéliser les interactions de dislocations, la rotation du réseau cristallin, la croissance des cavités et les effets de taille, offrant ainsi une meilleure compréhension des mécanismes de déformation critiques tels que la localisation des déformations, la formation de bandes de cisaillement et l'évolution des cavités. En adoptant une approche eulérienne, ce travail surmonte les difficultés liées à la distorsion de maillage rencontrées dans les méthodes traditionnelles, permettant des simulations précises des grandes déformations. Des simulations à haute résolution en plasticité cristalline, rendues possibles grâce à une technique de remaillage, sont utilisées pour explorer le rôle des attracteurs de densité de dislocations et d'orientation du réseau cristallin, ainsi que les mécanismes derrière la croissance et l'évolution des formes des cavités lors de la déformation.

La prédiction des attracteurs d'orientations cristallines dans les processus de déformation pilotés par le gradient de vitesse est cruciale pour comprendre la texture finale d'un polycristal. Nous avons réalisé une analyse de stabilité sur un problème simplifié (2D avec trois systèmes de glissement) afin de développer une stratégie théorique capable de prédire les attracteurs d'orientations cristallines à grande déformation. Deux simulations numériques illustrent cette théorie : la déformation d'un polycristal sous un chargement de gradient de vitesse homogène et l'évolution d'une cavité dans un monocristal sous un gradient de vitesse non homogène.

Nous avons développé une analyse de stabilité pour les processus pilotés par les taux de glissement pour certains modèles établis basés sur la densité de dislocations, y compris le modèle de Kocks et Mecking (KM) et ses variantes, afin d'identifier les conditions menant à des états stationnaires dans les systèmes de glissement actifs et d'évaluer leur stabilité linéaire. Notre analyse peut être généralisée à tout type

de modèle de densité de dislocations, fournissant ainsi un cadre plus large pour comprendre la stabilité de ces systèmes. Il est intéressant de noter qu'à partir d'un modèle qui ne considère pas les effets d'échelle, nous révélons des effets dépendants de la taille se manifestant à travers des variations initiales de la densité de dislocations, en particulier dans les échantillons préparés par FIB, influençant les réponses d'adoucissement ou de durcissement des matériaux. Des simulations numériques de compression de micro piliers ont été réalisées pour aborder le comportement des matériaux à des dimensions nano/micrométriques.

Les mécanismes de croissance et de coalescence des cavités sont des facteurs clés dans la rupture ductile des matériaux cristallins, se produisant à travers un écoulement plastique important autour de cavités préexistantes ou de cavités nucléées sur des particules de seconde phase. L'objectif principal est d'analyser la croissance de cavités plates dans des monocristaux (HCP, FCC) en utilisant des simulations par éléments finis en plasticité cristalline avec une déformation eulérienne pour mieux comprendre la croissance des cavités. Le modèle proposé permet non seulement de capturer le début de l'écoulement plastique, mais aussi de prédire avec précision l'évolution des formes des cavités. Le modèle est appliqué à des études expérimentales ayant observé qu'une cavité initialement circulaire dans un cristal HCP évolue vers une cavité polyédrique sous un chargement radial. Deux configurations sont étudiées : un chargement radial appliqué sur un cristal à structure hexagonal compact (HCP) et un chargement en traction sur un cristal cubique à faces centrées (FCC). Ces cas illustrent la capacité du modèle à s'adapter à différentes structures cristallographiques et conditions de chargement, démontrant ainsi sa large applicabilité.

Enfin, nous dérivons des formules pour calculer la contrainte réelle dans les situations où des bandes de glissement ou des bandes en genou se forment lors des tests de compression sur des piliers. Plus précisément, nous considérons une localisation, souvent observée expérimentalement, sous forme d'une bande unique orientée dans des directions arbitraires par rapport à l'axe vertical du pilier. Nous en dérivons une formule et l'utilisons pour évaluer la fiabilité des résultats expérimentaux précédents. Ces formules sont très simples et nécessitent uniquement les données de contrainte conventionnelle nominale, quelques données géométriques (rapport d'aspect) et des données mécaniques (limite élastique), faciles à obtenir à partir des résultats expérimentaux. Elles constituent un outil précieux pour interpréter avec précision le comportement mécanique des matériaux sous des charges de compression et pour

tirer des conclusions appropriées sur les valeurs de contrainte réelle.

Acknowledgements

First and foremost, I would like to express my deepest gratitude to **Ioan R. Ionescu** and **Umut Salman**, my Ph.D. supervisors, for their constant support, invaluable guidance, and immense patience throughout this journey. Their constructive feedback and thoughtful discussions have enriched my research experience, both scientifically and personally. Their expertise and encouragement have been instrumental in shaping this research, and I feel privileged to have had the opportunity to work under their mentorship.

I extend my heartfelt thanks to the members of my defense jury for their time and valuable insights: **Bilen Emek Abali** and **Fabrice Richard**, who served as referees. I am also sincerely grateful to **Aylin Ahadi**, **Maurine Montagnat**, and **Joseph Paux** for kindly accepting to examine this work as members of the examination committee.

Special thanks go to my colleagues and fellow researchers at LSPM, whose collaboration, assistance, and camaraderie have made this endeavor more enjoyable and rewarding. I would also like to extend my appreciation to the administrative at LSPM for their support in facilitating my research.

I would like to acknowledge the financial support provided through the doctoral contract from the Galilée Doctoral School, without which this research would not have been possible. Lastly, I am eternally grateful to my family and friends, whose love, patience, and encouragement have been my constant source of strength throughout this journey. Your unwavering belief in me has made all the difference.

Contents

List of Notations

Symbol	Description
$\mathbf{a} \otimes \mathbf{b} = a_i b_j$	Tensorial product of two vectors
$\mathbf{A} : \mathbf{B} = A_{ij} B_{ij}$	Scalar product of two second-order tensors
t	Time
x_1, x_2, x_3	Eulerian coordinates
x, y, z	Eulerian coordinates
$\boldsymbol{e}_1, \boldsymbol{e}_2, \boldsymbol{e}_3$	Eulerian coordinates basis
r, φ, z	Eulerian cylindrical coordinates
$\boldsymbol{e}_r, \boldsymbol{e}_\varphi, \boldsymbol{e}_z$	Eulerian cylindrical coordinates basis
div	Divergence with respect to the current configuration
∇	Gradient with respect to the current configuration
ρ^{mass}	Mass density
p	Pressure
$\boldsymbol{v}$	Velocity
$\boldsymbol{\sigma}$	Cauchy stress tensor
$\boldsymbol{\sigma}'$	Deviatoric Cauchy stress
τ^s	Resolved shear stress of the slip system s
τ_c^s	Critical resolved shear stress of the slip system s
τ_0	Intrinsic lattice resistance
$\boldsymbol{D}$	Rate of deformation tensor
$\boldsymbol{W}$	Spin tensor
$\dot{\gamma}^s$	Slip rate of the slip system s
$\boldsymbol{F}$	Deformation gradient
$\boldsymbol{F}_e$	Elastic part of deformation gradient
$\boldsymbol{P}$	(visco-)plastic part of deformation gradient
Continued on next page	

Symbol	Description
$\boldsymbol{R}$	Rotation of the crystal axes
$\boldsymbol{I}$	Identity matrix
N	Number of slip systems
$\boldsymbol{b}_s$	Slip direction in the s-th system
$\boldsymbol{m}_s$	Normal to slip direction in the s-th system
$\boldsymbol{M}_s$	Symmetric part of $\boldsymbol{b}_s \otimes \boldsymbol{m}_s$
$\boldsymbol{Q}_s$	Skew part of $\boldsymbol{b}_s \otimes \boldsymbol{m}_s$
η_s	Viscosity coefficient in the s-th system
$J(\dot{\gamma}^1, \dot{\gamma}^2, ..., \dot{\gamma}^N)$	Internal plastic dissipation power
$\boldsymbol{n}$	Normal vector on the crystal domain boundary
$\boldsymbol{S}$	Stress vector imposed on the boundary
$\boldsymbol{V}$	Velocity imposed on the boundary
θ	angle of the $\boldsymbol{b}_1$ axis with the Eulerian axis $\boldsymbol{e}_1$
ϕ	The angle between the slipping sytem 1 and 2
θ^{st}	Stationary orientation
ρ_s	Dislocation density of the system s
α	Dimensionless parameter describing the mean strength of obstacles encountered by mobile dislocations
b	Burgers vector modulus
d^{sp}	Dimensionless interaction matrix for slip system interactions
$\mathcal{M}^s$	The dislocation multiplication rate in the s-th system
$\mathcal{A}^s$	The dislocation annihilation rate in the s-th system
$\tilde{\rho}_{sat}$	dislocation density attractor
$\tau_{c,sat}^s$	The yield stregth attractor
D_m	the average grain size
E	Young modulus
ν_{pois}	Poisson's ratio
μ_e, λ_e	Lamé coefficients
σ_Y	Yield Von-Mises stress

Chapter 1

Introduction

Metallic materials used in structural applications are commonly produced as polycrystals, composed of numerous grains, each with its own unique crystallographic orientation. This results in varying degrees of plastic deformation across the grains, influenced by factors such as each grain's orientation, geometry, interaction with neighboring crystals, and the applied loading conditions [53]. Beyond this intergranular deformation heterogeneity, intragranular heterogeneity also emerges during plastic deformation, manifesting as localized, continuous, or discontinuous orientation spreads within individual grains [114].

The study of localized deformation patterns and the resulting microstructures is essential for advancing the understanding of phenomena such as strain localization [52, 102], fracture [74], shear banding [101, 90], and recrystallization [108].

To predict and analyze plasticity, there are three main computational approaches as depicted in Figure 1.1 : Molecular Dynamics (MD), Discrete Dislocation Dynamics (DDD), and Crystal Plasticity (CP). MD models atomic-scale phenomena but is limited to very small volumes(e.g., atomistic behavior of single dislocations), while DDD tracks individual dislocations at the mesoscale but becomes computationally expensive for large systems. CP, on the other hand, offers a continuum approach that efficiently models dislocation glide mechanisms and interactions between dislocations, predicting texture evolution, slip system activation, and hardening. CP strikes a balance between accuracy and computational efficiency, making it suitable for modeling deformation across a wide range of length scales, from grain scale to bulk materials.

Crystal Plasticity (CP) has garnered significant attention for its ability to model key phenomena such as dislocation interactions, lattice orientation evolution under
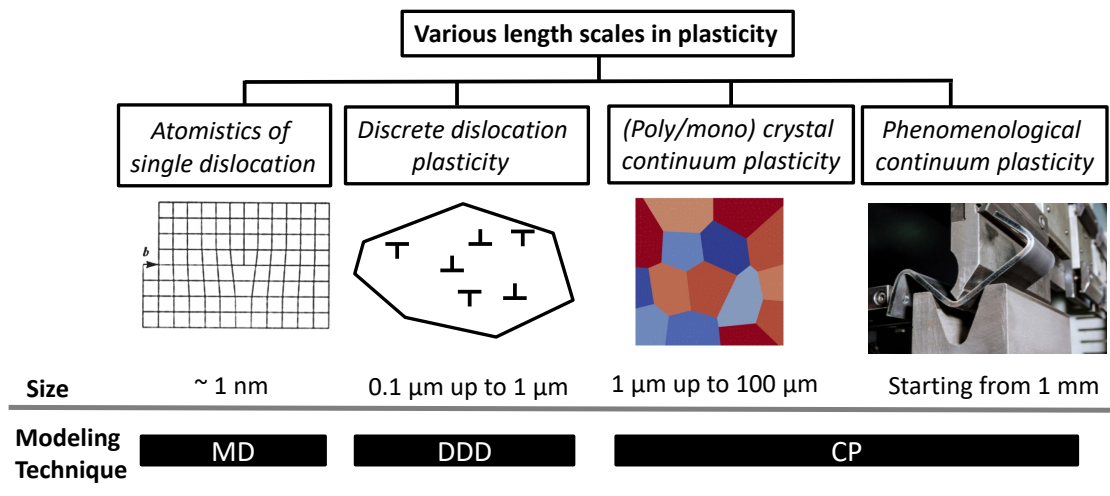
Figure 1.1: Modeling Techniques and Length Scales in Plasticity: A schematic illustration representing plasticity across scales, from the nanoscale (atomistic behavior of single dislocations) to the macroscale (phenomenological continuum plasticity), along with their corresponding modeling approaches.
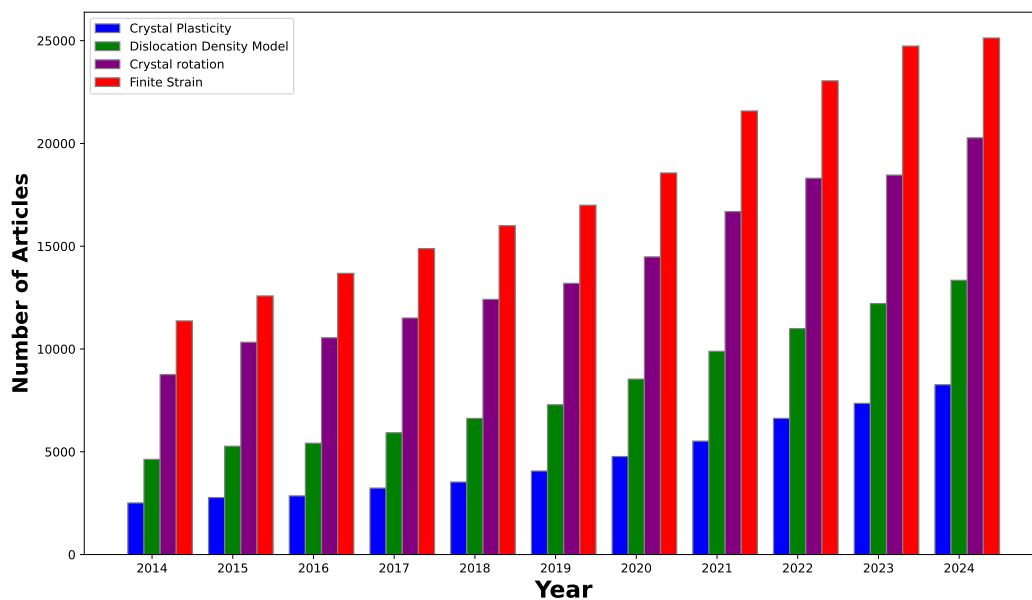
Figure 1.2: Evolution of the number of articles related to the keywords "Crystal Plasticity","Dislocation Density Model", "Crystal rotation" and "Finite strain" published since 2014 (Source: Science Direct).

high level of deformation. To highlight the growing interest in these areas, a Fig. 1.2 is included, showing the rise in publications since 2014 related to keywords such as "Crystal Plasticity","Dislocation Density Model", "Crystal rotation" and "Finite strain"(source: ScienceDirect).

Moreover, CP has proven valuable in studying size-dependent effects, particularly the "smaller is stronger" trend. This capability has been well-demonstrated in micropillar compression simulations, where CP effectively captures microstructural behavior under varying conditions. CP has also been instrumental in investigating cavity growth and coalescence, which are critical in understanding material failure mechanisms.

The primary focus of this thesis is on the evolution of dislocation density and crystal orientation at high levels of deformation in mono/polycrystalline materials. By investigating how these features change under severe plastic deformation, this study aims to enhance the understanding of how materials behave under extreme loading conditions. This analysis is critical for understanding mechanisms like strain localization, shear band formation, and the resulting hardening or softening of materials. Numerical simulations and rigorous mathematical analysis are employed throughout the work to predict how microstructures evolve, including material hardening, shear band formation, and strain localization.

Moreover, the research bridges theoretical modeling with practical applications by providing a new perspective on the key processes driving plastic deformation in crystalline materials. The findings from this study are expected to advance the understanding of crystal plasticity and contribute valuable tools for predicting material behavior under extreme conditions.

The level of detail and accuracy in crystal plasticity simulations heavily depends on the simulation's resolution. While low-resolution simulations may be sufficient for predicting macro-scale behaviors like stress-strain responses, higher-resolution simulations are required to capture the intricacies of deformation localization at small scale. High-resolution models with hundreds of thousands of elements per crystal [36]are needed, especially since many of these localization phenomena become prominent at large strains.

Conventionally, large deformation simulations are performed in a Lagrangian framework, where the mesh follows the deforming material. While effective for moderate strains, as deformation progresses, mesh distortion introduces significant errors and ultimately leads to simulation failure. To address these challenges, this

thesis adopts an Eulerian approach, which is particularly effective for simulating extreme deformations. In the Eulerian formulation, a fixed grid allows materials to flow through without distorting the mesh, making it ideal for analyzing complex material behavior during severe plastic deformation.

The elastic-(visco-)plastic model needs a permanent interplay between both Eulerian (more appropriate for plasticity) and Lagrangian (more appropriate for elasticity) descriptions. However, in applications involving large deformations of metals the elastic component of the deformation is small with respect to the inelastic one, and can be neglected by using a rigid-(visco)plastic approach (see for instance [56, 71, 69]). This simplified model takes important theoretical and numerical advantages by using only one (Eulerian) configuration.

This thesis aims to comprehensively analyze how dislocation density and crystal orientation evolve during large deformations. Our objective is to align the insights from this analysis with experimental observations and offer a robust framework for investigating the stability and localization phenomena in crystalline materials subjected to very large deformations. This work starts from the Eulerian framework in modeling large deformations in crystal plasticity introduced by [14] and uses the high-resolution numerical methods developed in [15]. Building on this foundational work, the model was later adopted and further advanced in [110] to investigate the effects of disorder and crystal orientation on the mechanical response of FCC crystal micropillars under compression.

Chapter 2 recall from [15, 14] the Eulerian approach to large deformation crystal plasticity, outlining its formulation in both 3D and 2D (in-plane) contexts, along with the numerical integration strategy. This foundational chapter covers key elements such as the momentum balance equation, the incompressibility condition, the flow rule, lattice rotation equation and potential models for dislocation density evolution, setting the stage for the analyses in later chapters.

Chapter 3 investigates lattice orientation attractors in both single and polycrystalline (HCP, FCC) materials, focusing on how lattice orientations evolve under velocity-gradient-driven processes. The chapter explores the stable orientation states that crystals adopt during deformation, offering insights into texture development and material behavior under uniform loading. To study orientation stability, the Eulerian rate-dependent crystal plasticity model is employed in the context of accumulative channel-die compression.

Chapter 4 shifts the focus to dislocation density attractors in slip-driven pro-

cesses, analyzing the evolution of dislocation structures toward stable configurations. The concept of attractors is explored to understand their role in strain hardening and material strengthening/softening. The stability of dislocation density-based models is also assessed, with micropillar compression simulations showing strong alignment with experimental observations and highlighting size-dependent effects.

Chapter 5 covers the evolution of intragranular voids in monocrystals, focusing on void growth and shape evolution under large deformations. The mechanisms behind void growth and their dependence on material properties and deformation conditions are analyzed using Eulerian crystal plasticity simulations. This chapter builds on prior research by offering new insights into both void growth and shape evolution at the onset of yielding and during large-scale deformation.

Chapter 6 of the manuscript, recently published in [117], will focus on calculating true stress in localized plastic deformation during micro- and nanoscale compression experiments. It will present an analytic approach, derived from mechanical-geometrical assumptions, to calculate true stress from standard experimental data, without the need for finite element simulations. This chapter will validate the method through numerical simulations and discuss its practical implications for material design and experimental interpretation.

The numerical simulations discussed throughout this thesis were carried out using an in-house code written in the FreeFEM++, a powerful finite element method (FEM) software. For post-processing and visualization of the results, ParaView, a widely used tool for 3D data analysis, was employed.

By combining advanced numerical simulations with theoretical analysis, this thesis provides a detailed framework for understanding dislocation dynamics, deformation localization, and their impact on the mechanical properties of materials under extreme conditions, offering valuable tools for both fundamental research and practical engineering applications.

Chapter 2

Eulerian approach of large deformations in crystal plasticity

2.1 Introduction

Crystalline solids exhibit plastic flow when macroscopic stresses surpass specific thresholds. The plastic deformation of crystals is primarily due to the generation and motion of interacting lattice defects known as dislocations. Dislocations evolve collectively within a complex energy landscape, influenced by applied loads and long-range interactions [130]. Controlling crystal plasticity is crucial for various applications, including metal hardening [21], fatigue failure [61], nano-scale forming, and micro-pillar optimization [20, 137, 96].

Plastic deformation in crystalline materials is highly complex, involving multiple length scales. These spatial heterogeneities range from the atomistic scale (dislocation cores and grain boundary structures) to mesoscale dislocation patterns and grain microstructures, extending to the macroscopic scale of the specimen. At the macroscopic level, plasticity manifests as a smooth flow described by a continuous stress-strain response.

Several theories have been developed to describe and understand plastic deformation at the macroscopic level. Continuum Crystal Plasticity (CP) theory is the most widely used approach for modeling crystal plasticity. This theory incorporates lattice-based kinematics into the classical continuum framework. Its original mathematical formulation was introduced by Hill [50] and Hill and Rice [51], with initial applications by Asaro and Rice [8, 6] and Pierce, Asaro, and Needleman [100]. Since then, many authors have further developed CP theory (see [107] for a com-

prehensive overview). The classical Continuum crystal theory of plasticity assumes that crystalline materials undergo irreversible flow when applied stresses exceed certain thresholds. This theory models the stress-strain response with continuous curves, implying that the heterogeneities are averaged out. This approach has been successful in reproducing key plasticity phenomena such as yield, hardening, and shakedown.

CP theory spans macroscopic length scales, from micrometers (μm) to millimeters (mm), due to its coarser representation of plastic deformation compared to other methods such as molecular dynamics or discrete dislocation dynamics approaches. In recent CP formulations, deformations are considered finite, and the continuum description clearly distinguishes between reference and deformed configurations.

2.2   Multiplicative decomposition of the deformation gradient

Consider a single crystal at time $t = 0$, free of any surface tractions and body forces and let choose this configuration, say $\mathcal{K}_0 \subset \mathbb{R}^d$ (here $d = 2, 3$ is the space dimension) as reference configuration of the crystal. Let $\mathcal{K} = \mathcal{K}(t) \subset \mathbb{R}^d$ denote the current configuration. The incorporation of lattice features is achieved through a multiplicative decomposition of the total deformation gradient $\boldsymbol{F}$ into elastic and plastic components:

$$\boldsymbol{F} = \boldsymbol{F}^e \boldsymbol{P}. \tag{2.1}$$

This decomposition implies a two-stage deformation process. First, $\boldsymbol{P}$ transforms the initial reference state $\mathcal{K}_0$ to an intermediate state $\tilde{\mathcal{K}}$, characterized by plastic deformation only with no change in volume. $\boldsymbol{P}$ is called the (visco)plastic deformation with respect to the reference configuration of a material neighborhood of the material point X at time t. Then, $\boldsymbol{F}^e$ brings the body to the final configuration $\mathcal{K}$ through elastic deformation and rigid lattice rotation, i.e. $\boldsymbol{F}^e = \boldsymbol{R}\boldsymbol{U}^e$ where $\boldsymbol{R}$ denotes the rotation of the crystal axes with respect to its isoclinic orientation. In Figure 2.1 are shown the geometric decomposition and mapping of the crystal deformation and rotation of the lattice axes.

A constitutive law for the elastic part of the deformation (see [87] for example) is needed. Simplest formulations assume a linear relationship between the second Piola-Kirchhoff stress tensor and the Right Cauchy-Green strain tensor in

the intermediate configuration $\tilde{\mathcal{K}}$, though higher order elastic moduli have also been considered [123]. These incremental equations, relating total (plastic and elastic) stress to total deformation, can be equivalently mapped to the deformed configuration as done in [7, 6]. The original formulation in the undeformed configuration is summarized in [48, 88, 25].
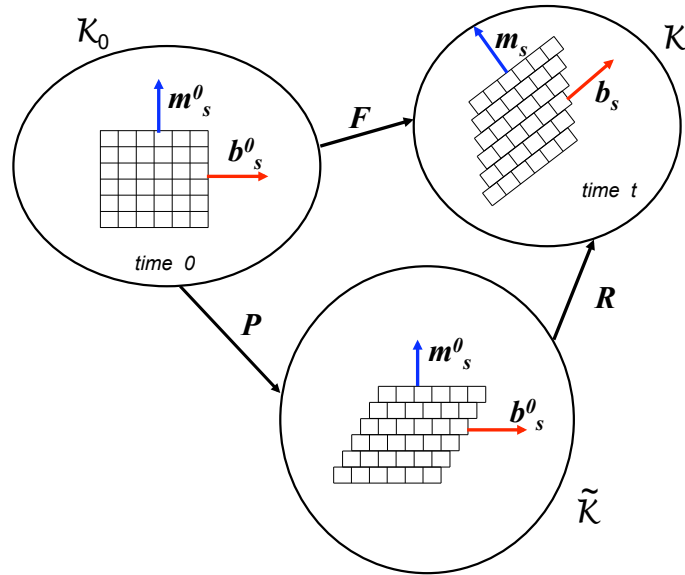

Figure 2.1: Various configurations associated with the lattice rotation of a viscoplastic crystal

Following [80, 8], $\boldsymbol{P}$ is assumed to leave the underlying lattice structure undeformed and unrotated, ensuring the uniqueness of the decomposition in (2.1). The unique feature of CP theory is its construction of the plastic component $\boldsymbol{P}$ by constraining dislocation kinematics. Plastic flow evolves along pre-selected slip directions via volume-preserving shears, leaving the crystal lattice undistorted and stress-free [87].

Since in applications involving large deformations and high strain rates, the elastic component of the deformation is small with respect to the inelastic one, it can be neglected and a rigid-viscoplastic approach will be adopted (such a hypothesis is generally used e.g. Hutchinson [56], Lebensohn and Tome [71], Kok et al.[69], etc.). That means that we neglect the elastic lattice strain $\boldsymbol{U}^e$ by supposing that $\boldsymbol{U}^e \approx \boldsymbol{I}$. This leads to the following decomposition for the deformation gradient $\boldsymbol{F}$ (see for example Kok et al. [69]):

$$\boldsymbol{F} = \boldsymbol{R}\boldsymbol{P}. \tag{2.2}$$

Such a hypothesis is valid since during forming or other industrial processes, the elastic component of deformation is negligibly small (typically 10^{-3}) in comparison to the plastic component (typically $>10^{-1}$). It also to be noted that once the elastic/plastic transition is over the stress evolution in the grains is controlled by plastic relaxation (see Tomé and Lebensohn [71]).

2.3   Eulerian description of the lattice rotations

Crystal slip systems are labeled by integers $s = 1, ..., N$, with N denoting the number of slip systems. Each slip system s is specified by the unit vectors $(\boldsymbol{b}_s^0, \boldsymbol{m}_s^0)$, where $\boldsymbol{b}_s^0$ is in the slip direction and $\boldsymbol{m}_s^0$ is normal to the slip plane in the perfect undeformed lattice. Since the viscoplastic deformation does not produce distortion or rotation of the lattice, the mean lattice orientation is the same in the reference and intermediate configurations and is specified by $(\boldsymbol{b}_s^0, \boldsymbol{m}_s^0), s = 1...N$.

Let $\boldsymbol{b}_s = \boldsymbol{b}_s(t)$ and $\boldsymbol{m}_s = \boldsymbol{m}_s(t)$, the glide direction and glide plane normal, respectively in the deformed configuration i.e. $\boldsymbol{b}_s(0) = \boldsymbol{b}_s^0$ and $\boldsymbol{m}_s(t) = \boldsymbol{m}_s^0$. Since elastic effects are neglected,

$$\boldsymbol{b}_s = \boldsymbol{R}\boldsymbol{b}_s^0, \quad \boldsymbol{m}_s = \boldsymbol{R}\boldsymbol{m}_s^0, \tag{2.3}$$

Note that according to (2.3), $\boldsymbol{b}_s$ and $\boldsymbol{m}_s$ are unit vectors. Furthermore,

$$\boldsymbol{b}_s \otimes \boldsymbol{m}_s = \boldsymbol{R} \left(\boldsymbol{b}_s^0 \otimes \boldsymbol{m}_s^0 \right) \boldsymbol{R}^T. \tag{2.4}$$

We seek to express the lattice evolution equations only in terms of vector and tensor fields associated with the current configuration. Let $\boldsymbol{v} = \boldsymbol{v}(t, x)$, the Eulerian velocity field, $\boldsymbol{L}$ the velocity gradient, $\boldsymbol{D}$ the rate of deformation, and $\boldsymbol{W}$ the spin tensor

$$\boldsymbol{L} = \boldsymbol{L}(\boldsymbol{v}) = \nabla\boldsymbol{v}, \quad \boldsymbol{D} = \boldsymbol{D}(\boldsymbol{v}) = (\nabla\boldsymbol{v})^{symm}, \quad \boldsymbol{W} = \boldsymbol{W}(\boldsymbol{v}) = (\nabla\boldsymbol{v})^{skew}. \tag{2.5}$$

The viscoplastic deformation is due to slip only; the slip contribution to the viscoplastic deformation being ([104], [125])

$$\dot{\boldsymbol{P}}\boldsymbol{P}^{-1} = \sum_{s=1}^{N} \dot{\gamma}^s \boldsymbol{b}_s^0 \otimes \boldsymbol{m}_s^0, \tag{2.6}$$

where $\dot{\gamma}^s = \dot{\gamma}^s(t)$ is the viscoplastic shear rate on the slip system s. If we denote by

$$\boldsymbol{M}_s = (\boldsymbol{b}_s \otimes \boldsymbol{m}_s)^{symm}, \quad \boldsymbol{Q}_s = (\boldsymbol{b}_s \otimes \boldsymbol{m}_s)^{skew}. \tag{2.7}$$

then, using $\boldsymbol{L} = \dot{\boldsymbol{F}}\boldsymbol{F}^{-1} = \dot{\boldsymbol{R}}\,\boldsymbol{R}^T + \boldsymbol{R}\dot{\boldsymbol{P}}\boldsymbol{P}^{-1}\,\boldsymbol{R}^T$, Eqs. (2.4) and (2.6), the rate of deformation $\boldsymbol{D}$ can be written as

$$\boldsymbol{D} = \sum_{s=1}^{N} \dot{\gamma}^s \boldsymbol{M}_s. \tag{2.8}$$

Taking the anti-symmetric part of $\boldsymbol{L}$, we obtain that the spin tensor is $\boldsymbol{W} = \dot{\boldsymbol{R}}\,\boldsymbol{R}^T + \sum_{s=1}^{N} \dot{\gamma}^s \boldsymbol{Q}_s$ and a differential equation for the rotation tensor $\boldsymbol{R}$:

$$\dot{\boldsymbol{R}} = (\boldsymbol{W} - \sum_{s=1}^{N} \dot{\gamma}^s \boldsymbol{Q}_s)\boldsymbol{R}. \tag{2.9}$$

The evolution equations (2.9) describe the evolution of the lattice in terms of vector and tensor fields associated with the current configuration.

2.4   Plastic and visco-plastic flow rules

In order to complete the model, we need to provide the constitutive equation for the slip rate $\dot{\gamma}_s$ as a function of τ_s, the stress component acting on the slip plane of normal $\boldsymbol{m}_s$ in the slip direction $\boldsymbol{b}_s$. In the current configuration, τ_s is expressed as

$$\tau^s = \boldsymbol{\sigma} : \boldsymbol{M}_s, \tag{2.10}$$

where $\boldsymbol{\sigma} = \boldsymbol{\sigma}(t)$ is the Cauchy stress tensor acting in the current configuration $\mathcal{K}$ while $\boldsymbol{M}_s$ is defined by (2.7). Note that $\{\tau^s\}_{s=\overline{1,N}}$ are not independent; they belong to a fifth dimensional space of $\mathbb{R}^N$ corresponding to the dimension of the space of deviatoric stresses.

To determine the shear strain rates $\dot{\gamma}_\alpha$ relative to the local stress, a constitutive law is needed. Various proposals exist, ranging from phenomenological to more physically based approaches. One simple phenomenological approach assumes that $\dot{\gamma}_\alpha$ depends on the stress only through the resolved shear stress τ^s.

In rigid-plastic formulations, it is assumed that the onset of plastic flow of a slip system s is governed by Schmid law: the slip system s is active if and only if

$|\tau^s| = \tau^s_c$, i.e.

$$\dot{\gamma}_s(|\tau^s| - \tau^s_c) = 0, \quad \dot{\gamma}_s\tau^s \geq 0, \quad |\tau^s| - \tau^s_c \leq 0, \tag{2.11}$$

where τ^s_c is the slip resistance (also called critical resolved shear stress or CRSS). For a given time t, the τ^s_c are material constants. Thus, the planes $|\tau^s| = \tau^s_c$ are the facets of the current yield surface of the single crystal in the stress space.

Since the resolved shear stresses τ^s are not independent, the shear rates $\dot{\gamma}^s$ given by the viscoplastic flow rule (2.11) are not independent; they have to satisfy the kinematic constraint (2.8). Given the rate of deformation $\boldsymbol{D}$, the slip rates $\dot{\gamma}^s$ can be determined by minimizing the internal plastic dissipation power

$$J_{Schmid}(\dot{\gamma}^1, \dot{\gamma}^2, ..., \dot{\gamma}^N) = \sum_{s=1}^{N} \tau^s_c|\dot{\gamma}^s|, \tag{2.12}$$

over $\mathbb{R}^N$ under the constraint (2.8). The above functional is neither strongly convex or differentiable and the solution could not be unique. Additional assumptions are needed in order to restrict the number of solutions.

One way to overcome this difficulty of determining the active slip systems problem is to adopt a rate-dependent approach for the constitutive response of the single crystal. A widely used rate-dependent (viscoplastic) model is the Norton type model, which relates the shear strain rate $\dot{\gamma}^s$ on a slip system s to the resolved shear stress τ^s through a power-law (see Asaro and Needleman [5])

$$\dot{\gamma}^s = \dot{\gamma}^s_0 \left|\frac{\tau^s}{\tau^s_c}\right|^n \text{sign}(\tau^s), \tag{2.13}$$

where $\dot{\gamma}_0$ is a reference shear strain rate, while the exponent n has a fixed value. Since the internal plastic dissipation power reads

$$J_{Norton}(\dot{\gamma}^1, \dot{\gamma}^2, ..., \dot{\gamma}^N) = \frac{n}{n+1} \sum_{s=1}^{N} \tau^s_c|\dot{\gamma}^s| \left|\frac{\dot{\gamma}^s}{\dot{\gamma}^s_0}\right|^{\frac{1}{n}}, \tag{2.14}$$

we remark that $J_{Norton} \to J_{Schmid}$ for large values of n ($n \to \infty$) which means that the Norton law is a visoplastic regularization of the Schmidt law. Note that the plastic dissipation functional is strongly convex and differentiable which means the slip rates are the unique solution of the minimization problem of the plastic dissipation power J_{Norton} over $\mathbb{R}^N$ under the constraint (2.8).

Another regularization of the Schmid law can be done by using a Perzyna-like
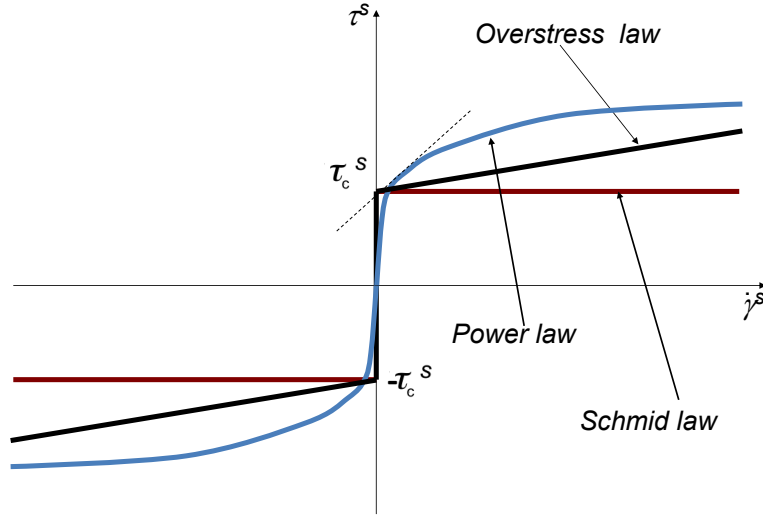
Figure 2.2: Schematic representation of two visco-plastic regularizations of the Schmid law (red line) : a power law (blue line) and overstress Perzyna-type viscoplastic law (black line).

viscoplastic law of the form (see also Figure 2.2),

$$\dot{\gamma}^s = \frac{1}{\eta_s} \left[|\tau^s| - \tau_c^s\right]_+ \mathrm{sign}(\tau^s), \tag{2.15}$$

where η_s is the viscosity, which may depend on the slip rate, and $[\,x\,]_+ = (x + |x|)/2$ denotes the positive part of any real number x. Note that the viscoplastic flow rule (2.15) is the visco-plastic extension of the rigid-plastic Schmid law using an overstress approach. The physical motivation for the dependence of the viscoplastic shear rate on the overstress $(\tau^s - \tau_c^s)$ was provided by Teodosiu and Sidoroff [125] based on an analysis of the microdynamics of crystals defects.

The internal power is given by

$$J_{Perzyna}(\dot{\gamma}^1, \dot{\gamma}^2, ..., \dot{\gamma}^N) = \sum_{s=1}^{N} \frac{\eta_s}{2}|\dot{\gamma}^s|^2 + \tau_c^s|\dot{\gamma}^s|, \tag{2.16}$$

and we remark that $J_{Perzyna} \to J_{Schmid}$ for a vanishing viscosity η_s $(\eta \to 0)$. The above functional is strongly convex, hence the slip rates are the unique solution of of the minimization problem of the plastic dissipation power $J_{Perzyna}$ over $\mathbb{R}^N$ under the constraint (2.8).

Finally we deduce that the slip rates $\dot{\gamma}^1, \dot{\gamma}^2, ..., \dot{\gamma}^N$ can be obtained by an opti-

mization problem involving the plastic dissipation power

$$(\dot{\gamma}^1, \dot{\gamma}^2, ..., \dot{\gamma}^N) = \arg\min_{\boldsymbol{D}=\sum_{s=1}^{N} g^s \boldsymbol{M}_s} J(g^1, g^2, ..., g^N)., \tag{2.17}$$

where J is one of the plastic dissipation power functionals J_{Schmid}, J_{Norton} or $J_{Perzyna}$.

2.5   Dislocation density hardening/softening models

The yield limits τ_c^s of each slipping system s can be considered as constants, but they can vary in time if hardening/softening effects are taken into consideration.

CP theory does not resolve individual plastic defects. Instead, dislocations are represented by continuously evolving incremental shear strains γ_α. This coarse representation conceals both short-range and long-range dislocation interactions. However, the simplified kinematics allows access to larger time and length scales, enabling the modeling of complex 3D systems with intricate geometries. The method can be implemented in a FEM setting, facilitating the modeling of various physical phenomena, from grain boundary evolution to pattern formation under cyclic loading [107]. On the other hand, dislocation-related effects, such as kink and shear-band formation, can also be included in the continuum CP model [31], albeit with a richer set of kinematic variables in contrast to phenomenological constitutive models using physics-based constitutive laws rely on internal variables with microstructural significance, such as lattice defect densities.

We complete here the above Eulerian crystal plasticity model with a dislocation density-based hardening/softening law. The model uses dislocation densities on slip planes, denoted by ρ^s, as internal variables to link the microstructure to macroscopic deformation. To be more precisely, the critical resolved shear stress vector $\boldsymbol{\tau}_c = (\tau_c^1, .., \tau_c^1)$ depends on the dislocation densities vector $\boldsymbol{\rho} = (\rho^1, .., \rho^N)$ as follows:

$$\boldsymbol{\tau}_c = \boldsymbol{\mathcal{T}}_c(\boldsymbol{\rho}). \tag{2.18}$$

For example, in the context of the Taylor model [121], and as proposed by Teodosiu and Raphanel [124] (see also [33]), the shear yield strength is expressed as :

$$\mathcal{T}_c^s(\boldsymbol{\rho}) = \tau_0 + \alpha\mu b \sqrt{\sum_{p=1}^{N} d^{sp}\rho^p}, \tag{2.19}$$

where τ_0 is the friction stress, α is a dimensionless parameter describing the mean strength of obstacles encountered by the mobile dislocation lines, b is the modulus of the burgers vector parameter that relates the discrete plastic deformation of crystalline materials to dislocation motion, μ is is the shear modulus and d^{sp} is a dimensionless interaction matrix expressing the average strength of the interactions and reactions between slip systems.

2.6   Dislocation density evolution models

These internal variables represent microstructural features, with dislocation density being the most crucial in the context of plasticity. Dislocations are the primary carriers of plastic deformation, making dislocation density a key microstructural state variable. By utilizing dislocation densities, numerous complex scenarios can be modeled, such as the interactions between dislocations and grain boundaries [78], prismatic slip in α-titanium alloys [2], deformation of single FCC crystals under high strains [9, 133], the size-dependent plastic flow [77] and precipitate-induced cyclic softening [1], among others, within the framework of crystal plasticity theory.

The evolution of the dislocation density can be developed from a phenomenological (statistical) model. The dislocation rate $\dot{\rho}^s$, which is proportional to the plastic slip rate $|\dot{\gamma}^s|$, is the sum of the dislocation multiplication rate $\mathcal{M}^s$ and of the dislocation annihilation rate $-\mathcal{A}^s$:

$$\dot{\rho}^s = \frac{1}{b}\left(\mathcal{M}^s(\boldsymbol{\rho}) - \mathcal{A}^s(\boldsymbol{\rho})\right)|\dot{\gamma}^s|. \tag{2.20}$$

For instance in the model of Kocks-Mecking-Teodosiu [89, 124] the multiplication and annihilation rates are given by

$$\mathcal{M}^s(\boldsymbol{\rho}) = \frac{\sqrt{\sum_{p=1}^N a^{sp}\rho^p}}{k}, \quad \mathcal{A}^s(\boldsymbol{\rho}) = 2y_c\rho^s, \tag{2.21}$$

where y_c is the mean distance controls the annihilation of dislocations and k is a proportionality factor, it represents the number of obstacle before a mobile dislocation get stopped and a^{sp} is a dimensionless interaction matrix.

The values of interaction a^{sp} coefficients are listed in the Table [2.1], which were determined from dislocation dynamic simulations [26, 70]

In the case of generalized Kocks-Mecking-Estrin model [132], which is **size de-**

a_0^{self}	$a_{cop}^{coplanar}$	a_{orth}^{Hirth}	$a_{gli}^{glissile}$	a_{lom}^{lomer}	$a_{col}^{collinear}$
0.122	0.122	0.07	0.137	0.127	0.625

Table 2.1: Values of the six independent interaction coefficients a_{ij} for FCC crystals.

pendent, the expressions for dislocation multiplication $\mathcal{M}^s$ and annihilation rates $\mathcal{A}^s(\boldsymbol{\rho})$ are provided as follows :

$$\mathcal{M}^s(\boldsymbol{\rho}) = \frac{\tilde{K}_0}{D_m} + \tilde{K}_1\sqrt{\rho^s}, \quad \mathcal{A}^s(\boldsymbol{\rho}) = bK_2\rho^s, \tag{2.22}$$

where $\tilde{K}_0$ is a production rate controlling factor (dimensionless), D_m the average grain size, $\tilde{K}_1$ governs the rate of dislocation storage by the interaction with immobile dislocations and K_2 is a controlling factor of recovery by the annihilation of dislocations.

In an alternative size-dependent model called the CLZ model [24], the multiplication and annihilation rates are :

$$\mathcal{M}^s(\boldsymbol{\rho}) = \frac{1}{2\bar{\lambda}} + k_f\sqrt{\rho^s}, \quad \mathcal{A}^s(\boldsymbol{\rho}) = y\rho^s + \frac{2\cos^2(\beta/2)}{D},$$

where the model parameters are : $\bar{\lambda}$ is the length of the statistically average effective Single Arm Source, k_f is a dimensionless constant and set at 10^{-2}, y is the effective mutual annihilation distance and set to be equal to $6b$, β the slip-plane orientation angle is the angle between the primary slip plane and the top surface of the single-crystal micropillars and D is the diameter sample.

In the dislocation density-based constitutive model of [63] it is assumed that the total dislocation-density ρ^s can be decomposed, into a mobile dislocation-density, ρ_m^s, and an immobile dislocation-density ρ_{im}^s as

$$\rho_{tot}^s = \rho_m^s + \rho_{im}^s.$$

For both of them we deal with two evolution equations

$$\frac{d\rho_m^s}{dt} = \left(\frac{g_{sour}}{b^2}\frac{\rho_{im}^s}{\rho_m^s} - \frac{g_{minter}}{b^2}\exp(-\frac{H}{kT}) - \frac{g_{immob}}{b}\sqrt{\rho_{im}}^s \right)|\dot{\gamma}^s|,$$

$$\frac{d\rho_{im}^s}{dt} = \left(\frac{g_{minter}}{b^2} \exp(-\frac{H}{kT}) + \frac{g_{immob}}{b} \sqrt{\rho_{im}^s} - g_{recov} \exp(-\frac{H}{kT})\rho_{im}^s \right) |\dot{\gamma}^s|$$

where g_{sour} represents the coefficient associated with the rise in mobile dislocation density attributed to dislocation sources, g_{minter} denotes the coefficient linked to the trapping of mobile dislocations resulting from interactions with forest intersections, cross-slip mechanisms around obstacles, or dislocation interactions, g_{recov} signifies the coefficient related to the rearrangement and annihilation of immobile dislocations, g_{immob} denotes the immobilization of mobile dislocations, H is the activation enthalpy, and k is Boltzmann's constant. Since only the immobile dislocation densities are responsible of the hardening/softening effect and their evolution is independent of the mobile ones we can conclude that immobile dislocation-density ρ_{im}^s plays the same role as ρ^s in the previous models. Moreover, the equation of immobile dislocation density evolution has the same structure as the generalized Kocks-Mecking-Estrin model. For that we have to take $\frac{\tilde{K}_0}{D_m} = \frac{g_{minter}}{b} \exp(-\frac{H}{kT})$, $\tilde{K}_1 = g_{immob}$ and $K_2 = g_{recov} \exp(-\frac{H}{kT})$.

Finally, the hardening or softening effects, described by (2.18) and (2.20), depend on the evolution of the dislocation density ρ^s on all systems s, that derives from the balance between accumulation and annihilation rates.

2.7   2-D model with 3 slip systems

The 3D system ($d = 3$) with a large number of slip systems N is too difficult to be analyzed from theoretical or physical point of view. That is why, in many situations, a simplification could be useful for a better understanding the complex phenomena which occur in the crystal deformation. We will introduce here a two dimensional model ($d = 2$) with $N = 3$ slip systems. In this case let us denote with ϕ and $-\phi$ the angles formed by slip system $r = 1$ with the other two systems $r = 2, 3$ and let θ be the angle formed by the slip system 1 with the Ox_1 axis (see Figure 2.3). The three composite in-plane slip systems $\boldsymbol{b}_1, \boldsymbol{b}_2, \boldsymbol{b}_3$ are specified by the angles $\theta, \theta + \phi, \theta - \phi$.

The main simplification for the 2-D problem comes from the latice rotation $\boldsymbol{R}$ which is now a rotation $\boldsymbol{R}(\theta, \boldsymbol{e}_3)$ with angle θ along $0x_3$ axis and we have

$$\boldsymbol{Q}_r = \frac{1}{2} \left((1,0) \otimes (0,1) - (0,1) \otimes (1,0) \right). \tag{2.23}$$
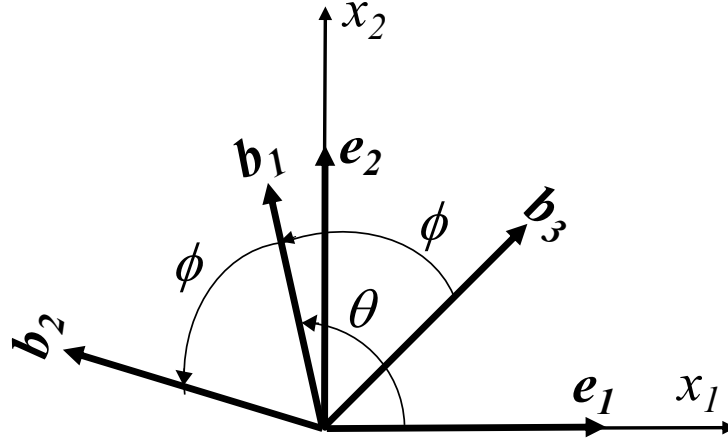
Figure 2.3: Two dimensional model with three slip systems.

for all $r = 1, 2, 3$ and (2.9) has a much more simpler form

$$\dot{\theta} = \frac{\partial \theta}{\partial t} + \boldsymbol{v} \cdot \nabla \theta = \frac{1}{2} \left(\sum_{r=1}^{3} \dot{\gamma}^r - (\frac{\partial v_1}{\partial x_2} - \frac{\partial v_2}{\partial x_1}) \right). \tag{2.24}$$

We have in mind two situations where this model is physically sound : i) the in-plane deformation of a FCC crystal, ii) the slip in the basal plane of a hexagonal crystal.

2.7.1   In-plane deformation of a FCC crystals

Rice [104] showed that certain pairs of the three-dimensional systems that are potentially active need to combine in order to achieve plane-strain deformation. For a F.C.C. crystal, with 12 potentially active slip systems, we consider Ox_3 axis to be parallel to [110] in the crystal basis, which means that the plane-strain plane (Ox_1x_2) is the plane $[\bar{1}10] - [001]$. Some geometrical constraints (see [15]) have to are satisfied such that $N = 3$ pairs of composite systems will give deformation in the plane (Ox_1x_2). As shown in Figure 2.4 the in-plane system $r = 1$ is formed by $(k, l) = (3, 12)$, $r = 2$ is formed by $(k, l) = (4, 5)$, and $r = 3$ is formed by $(k, l) = (7, 8)$ (here k, l are number of slipping directions for the 3-D FCC crystal). We also suppose in what follows that the systems $1, 2, 6, 9, 10$ and 11 are not active. For all $r = 1, 2, 3$ we have denoted by $\boldsymbol{b}_r, \boldsymbol{m}_r$ the normalized projections of the corresponding three-dimensional slip directions and normal directions (k, l) onto the

$x_1 x_2$-plane. The angle ϕ between the slipping sytem 1 and 2 is

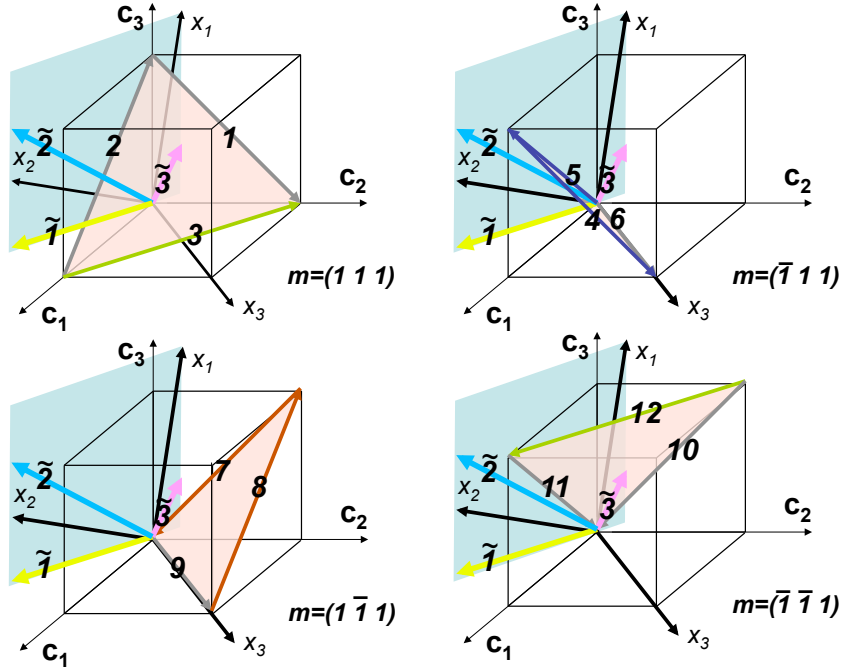$$\phi = \arctan(\sqrt{2}), \tag{2.25}$$

Figure 2.4: Three ($N = 3$) composite in-plane systems are: $\tilde{1} = (3, 12)$, $\tilde{2} = (4, 5)$ and $\tilde{3} = (7, 8)$, from [15].

Since there are some scalar factors between the first two components of the in-plane systems and the 3-dimensional ones given by

$$q_1 = \frac{1}{\sqrt{3}}, \quad q_2 = q_3 = \frac{\sqrt{3}}{2}, \tag{2.26}$$

the 2-D composite slipping rate $\dot{\gamma}^r$ corresponds to the 3-D slipping rate $\dot{\gamma}^k$ multiplied by $2q_r$. As it follows from [15] the 2-D yield limit τ_0^r corresponds to the 3-D yield limit τ_0^k divided by q_r while the 2-D viscosity η^r corresponds to the 3-D yield limit η^k divided by q_r^2.

2.7.2   Slip in the basal plane of a hexagonal crystal

Alternatively, this situation corresponds to hexagonal close-packed (hcp) crystals (such as Ti, Mg, Zr, etc) under plane strain, with the plane of deformation aligned with the basal plane (0001) of the hexagonal lattice. This situation has been ex-
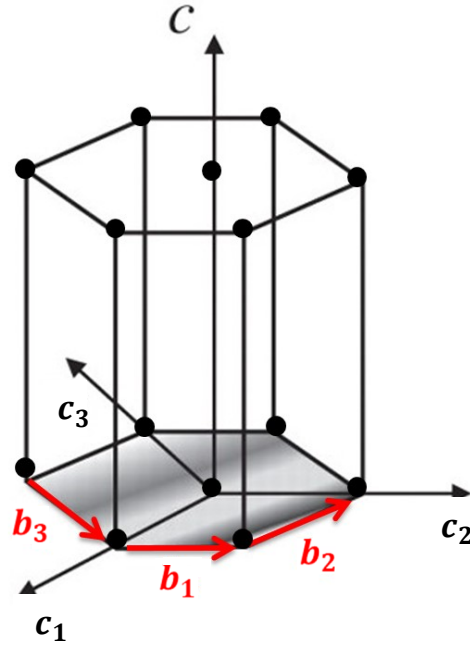
Figure 2.5: Hexagonal Bravais lattice, prismatic slip systems presented with red color and basal plane grayed out.

perimentally considered in [22]. In this situation, the plastic strain is mainly accommodated by the three prismatic slip systems, i.e. the $(10\bar{1}0)\langle 1\bar{2}10\rangle$ slip family, as illustrated in Figure 2.5. Each of those slip systems can act independently from the two others, as its strain is a plane strain. One might remark that combinations of other slip systems of hcp crystals from the basal and the pyramidal slip families could also lead to plane strain, but it would require significantly more energy, and therefore never occur. Thus, those slip families are not considered in this work. The prismatic slip systems are symmetrical, leading to

$$\phi = \pi/3 = 60°. \tag{2.27}$$

for a given rate of deformation $\boldsymbol{D}$ given in the Eulerian basis $\boldsymbol{e}_1, \boldsymbol{e}_2$ by

$$\boldsymbol{D} = D_{11}(\boldsymbol{e}_1 \otimes \boldsymbol{e}_1 - \boldsymbol{e}_2 \otimes \boldsymbol{e}_2) + D_{12}(\boldsymbol{e}_1 \otimes \boldsymbol{e}_2 + \boldsymbol{e}_2 \otimes \boldsymbol{e}_1) \tag{2.28}$$

and a given lattice orientation θ.

2.7.3   Rate of deformation slip rate decomposition

Another important simplification obtained in [15] for this model is the analytic expressions for the slip rates on individual composite systems $\dot{\gamma}_r$ for a given rate of

deformation $\boldsymbol{D}$, which in the Eulerian basis $\boldsymbol{e}_1, \boldsymbol{e}_2$ is written as

$$\boldsymbol{D} = D_{11}(\boldsymbol{e}_1 \otimes \boldsymbol{e}_1 - \boldsymbol{e}_2 \otimes \boldsymbol{e}_2) + D_{12}(\boldsymbol{e}_1 \otimes \boldsymbol{e}_2 + \boldsymbol{e}_2 \otimes \boldsymbol{e}_1), \qquad (2.29)$$

and a given lattice orientation θ. The slip rates $\dot{\gamma}_r$ ($r = 1, 2, 3$) can be determined by minimizing the internal power J under the constraints (2.8). Let us first remark that $\boldsymbol{M}_r = \boldsymbol{R}(\theta, \boldsymbol{e}_3)\tilde{\boldsymbol{M}}_r \boldsymbol{R}(-\theta, \boldsymbol{e}_3)$, where $\tilde{\boldsymbol{M}}_r = \left(\tilde{\boldsymbol{b}}_r \otimes \tilde{\boldsymbol{m}}_r\right)^{symm}$ and $\tilde{\boldsymbol{b}}_r$ corresponds to the orientation $\theta = 0$, i.e. $\tilde{\boldsymbol{b}}_1 = (1, 0), \tilde{\boldsymbol{b}}_3 = (\cos(\phi), \sin(\phi))$ and $\tilde{\boldsymbol{b}}_2 = (\cos(\phi), -\sin(\phi))$. If the initial orientation of the lattice is given by θ_0 then $\boldsymbol{M}_r^0 = \boldsymbol{R}(\theta_0, \boldsymbol{e}_3)\tilde{\boldsymbol{M}}_r \boldsymbol{R}(-\theta_0, \boldsymbol{e}_3)$. The strain rate decomposition (2.8) could be written as

$$\boldsymbol{D}^\theta = \boldsymbol{R}(-\theta, \boldsymbol{e}_3)\boldsymbol{D}\boldsymbol{R}(\theta, \boldsymbol{e}_3) = \sum_{r=1}^{3} \dot{\gamma}^r \tilde{\boldsymbol{M}}_r^0. \qquad (2.30)$$

Let us first decompose the three dimensional vector

$$\dot{\Gamma} = (\dot{\gamma}_1, \dot{\gamma}_2, \dot{\gamma}_3) = s\boldsymbol{S}^\phi + c\boldsymbol{C}^\phi + z\boldsymbol{Z}^\phi \qquad (2.31)$$

in the basis $\{\boldsymbol{S}^\phi, \boldsymbol{C}^\phi, \boldsymbol{Z}^\phi\}$, given by $\boldsymbol{S}^\phi = (0, \sin(2\phi), -\sin(2\phi))$, $\boldsymbol{C}^\phi = (1, \cos(2\phi), \cos(2\phi))$ and $\boldsymbol{Z}^\phi = \boldsymbol{S}^\phi \wedge \boldsymbol{C}^\phi = (-\sin(4\phi), \sin(2\phi), \sin(2\phi))$. Substitution of (2.31) into (2.30) leads to:

$$s(\theta) = -2\frac{\cos(2\theta)D_{11} + \sin(2\theta)D_{12}}{|\boldsymbol{S}^\phi|^2}, \qquad c(\theta) = 2\frac{\cos(2\theta)D_{12} - \sin(2\theta)D_{11}}{|\boldsymbol{C}^\phi|^2}, \quad (2.32)$$

where $|\boldsymbol{S}^\phi|^2 = 2\sin^2(2\phi)$ and $|\boldsymbol{C}^\phi|^2 = 1 + 2\cos^2(2\phi)$.

Since s and c are obtained from the kinematic condition (2.30) the slip rates $\dot{\Gamma}$ from (2.31) is a function of z hence the internal power J is a function of z only, i.e. $J(\dot{\gamma}^1, \dot{\gamma}^2, \dot{\gamma}^3) =: J(z)$. For instance for the Schmid model we have

$$J_{Schmid}(z) = \sum_{r=1}^{3} \tau_c^r |s(\theta)S_r^\phi + c(\theta)C_r^\phi + zZ_r^\phi|. \qquad (2.33)$$

Note that $z \to J^{Schmid}(z)$ is differentiable everywhere with the exception of three points, z_1^θ, z_2^θ and z_3^θ where $s(\theta)S_r^\phi + c(\theta)C_r^\phi + zZ_r^\phi = 0$, given by

$$z_1^\theta = -\frac{c(\theta)}{\sin(4\phi)}, \quad z_2^\theta = \frac{s(\theta)\sin(2\phi) + c(\theta)\cos(2\phi)}{\sin(2\phi)}, \quad z_3^\theta = \frac{-s(\theta)\sin(2\phi) + c(\theta)\cos(2\phi)}{\sin(2\phi)}.$$

However, the left and right derivatives $J'_{Schmid}(z_r^\theta-), J'_{Schmid}(z_r^\theta+)$ exist and can be

computed from

$$J'_{Schmid}(z) = \sum_{r=1}^{3} \tau_c^r |Z_r^\phi| \frac{z - z_r^\theta}{|z - z_r^\theta|}.$$

Since $z \to J_{Schmid}(z)$ is piece-wise linear the minimum of this convex function is $z(\theta) = z_m^\theta$ where z_m^θ is such that $J^{Schmid}(z_m^\theta) = \min_{r=1,2,3} J^{Schmid}(z_r^\theta)$ and we get

$$z(\theta) = z_r^\theta \quad \text{if} \quad J'_{Schmid}(z_r^\theta-)J'_{Schmid}(z_r^\theta+) \leq 0. \tag{2.34}$$

For the Perzyna viscoplastic regularization the power dissipation reads

$$J_{Perzyna}(z) = \sum_{r=1}^{3} \frac{\eta_r}{2} |s(\theta)S_r^\phi + c(\theta)C_r^\phi + zZ_r^\phi|^2 + \tau_c^r |s(\theta)S_r^\phi + c(\theta)C_r^\phi + zZ_r^\phi|. \tag{2.35}$$

and the general expression of $J'(z)$ as:

$$J'_{Perzyna}(z) = A^\theta + B^\phi z + \sum_{r=1}^{3} \tau_c^r |Z_r^\phi| \frac{z - z_r^\theta}{|z - z_r^\theta|},$$

with $A^\theta = \sum_{r=1}^{3} \eta_r (s(\theta)S_r^\phi + c(\theta)C_r^\phi)Z_r^\phi$, $B^\phi = \sum_{r=1}^{3} \eta_r (Z_r^\phi)^2$. We can now solve the equation $(J^{Perzyna})'(z) = 0$ to get the analytical expression of $z(\theta)$

$$z(\theta) = \begin{cases} z_r^\theta & \text{if} \quad J'_{Perzyna}(z_r^\theta-)J'_{Perzyna}(z_r^\theta+) \leq 0, \\ \dfrac{1}{B^\phi}\left[-A^\theta + \sum_{r=1}^{3} \tau_0^r |Z_r^\phi| \dfrac{J'_{Perzyna}(z_r^\theta+)}{|J'_{Perzyna}(z_r^\theta+)|} \right] & \text{otherwise} \end{cases} \tag{2.36}$$

Further substitution of (2.32) and (2.34) (or (2.36)) into (2.31) gives the analytical decomposition of the strain rate $\boldsymbol{D}(\boldsymbol{v})$ into the three slip rates $\dot{\gamma}_1, \dot{\gamma}_2, \dot{\gamma}_3$

$$(\dot{\gamma}_1(\theta), \dot{\gamma}_2(\theta), \dot{\gamma}_3(\theta)) = s(\theta)\boldsymbol{S}^\phi + c(\theta)\boldsymbol{C}^\phi + z(\theta)\boldsymbol{Z}^\phi \tag{2.37}$$

according to the constitutive equation (2.11) (or (2.15)).

The above formula, which gives the slip rate decomposition of the strain rate given by 2.29 in the Eulerian basis, is useful for the FE computations and plays a key role in the numerical algorithm. For the stability analysis is more convenient to
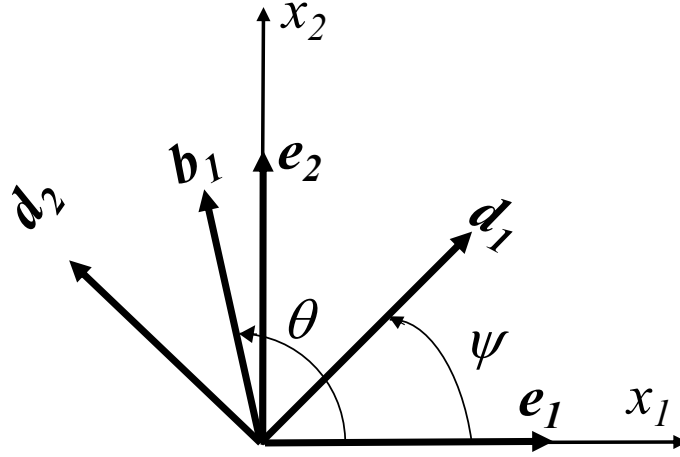
Figure 2.6: Angles of the principal strain rate directions ψ and the lattice orientations θ.

represent the strain rate $\boldsymbol{D}$ in its principal directions, denoted by $\boldsymbol{d}_1, \boldsymbol{d}_2$, as

$$\boldsymbol{D} = d(\boldsymbol{d}_1 \otimes \boldsymbol{d}_1 - \boldsymbol{d}_2 \otimes \boldsymbol{d}_2), \tag{2.38}$$

where $d > 0$ is the principal rate of deformation. We denote by ψ the angle between $\boldsymbol{d}_1$ and $\boldsymbol{e}_1$ (see Figure 2.6). To compute the slip rate decomposition in this configuration les us consider first the non-dimensional case $D_{12} = 0, D_{11} = 1$, called in the following "reference case", corresponding to $d = 1$ and $\psi = 0$. Let denote by

$$(\dot{\gamma}_1^{ref}(\theta), \dot{\gamma}_2^{ref}(\theta), \dot{\gamma}_3^{ref}(\theta)) = s^{ref}(\theta)\boldsymbol{S}^\phi + c^{ref}(\theta)\boldsymbol{C}^\phi + z^{ref}(\theta)\boldsymbol{Z}^\phi, \tag{2.39}$$

where s^{ref}, c^{ref} and z^{ref} are given by the above formulas for $D_{12} = 0, D_{11} = 1$. In Figure 2.7 we have plotted the reference slip rates $\dot{\gamma}_1^{ref}(\theta), \dot{\gamma}_2^{ref}(\theta), \dot{\gamma}_3^{ref}(\theta)$ for the Schmid model in the case of a FCC crystal. We remark that for 12 orientations $(\theta = \phi/4, \pi/4, \pi/2 - \phi/4, \pi/2 + \phi/4, 3\pi/4, \pi - \phi/4, ...)$ only one slip system is active while for any other orientation two slip systems are active and the maximum of the slip rate is 2. Moreover the dependence of the slip rates with the lattice orientation is not everywhere smooth: the angles where only one active slip system is active the derivative is discontinuous. This discontinuity, which is due to the Schmid rigid-plastic law, is not more present in the case of Perzyna regularization.

We can write now the (dimensional) slip rate decomposition for the strain rate

representation (2.38) to be

$$(\dot{\gamma}_1(\theta), \dot{\gamma}_2(\theta), \dot{\gamma}_3(\theta)) = d\left(\dot{\gamma}_1^{ref}(\theta - \psi), \dot{\gamma}_2^{ref}(\theta - \psi), \dot{\gamma}_3^{ref}(\theta - \psi)\right). \qquad (2.40)$$
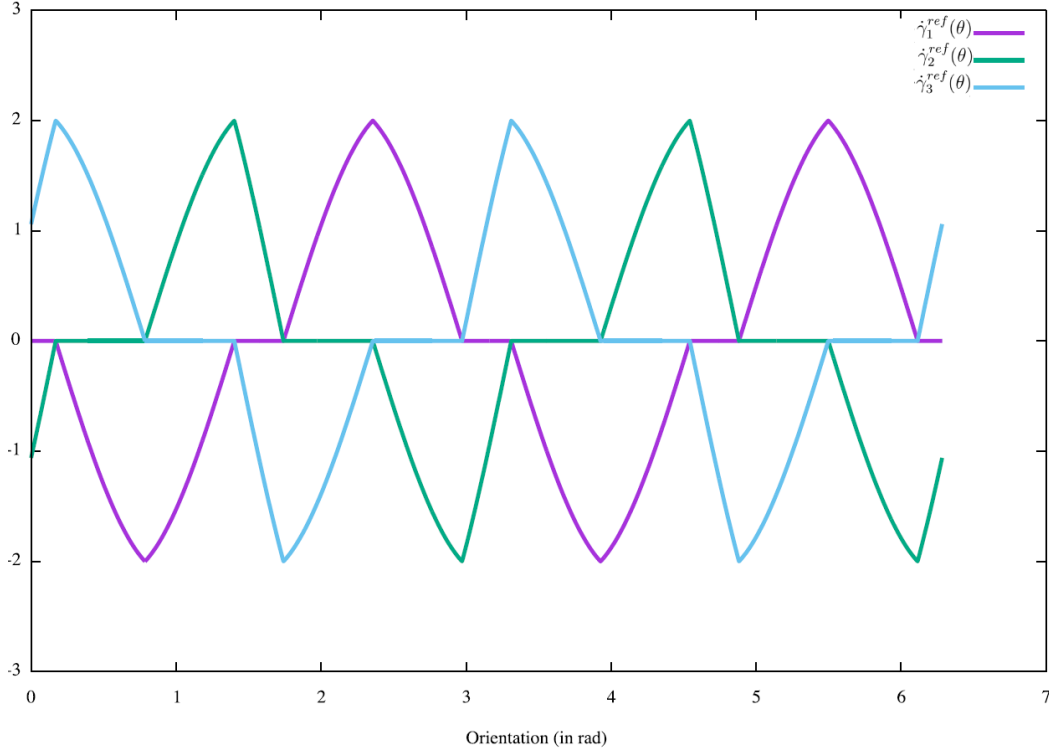

Figure 2.7: The reference slip rates $\theta \to (\dot{\gamma}_1^{ref}(\theta), \dot{\gamma}_2^{ref}(\theta), \dot{\gamma}_3^{ref}(\theta)))$ (i.e. for $D_{12} = 0, D_{11} = 1$) as functions of the lattice orientation θ in the case of in-plane deformation of a FCC crystal.

2.8   Initial and boundary value problem formulation

We begin by presenting the equations governing the motion in a domain $\mathcal{D} = \mathcal{D}(t)$ of an incompressible rigid-viscoplastic crystal. In an Eulerian description of a crystal visco-plasticity theory, the unknowns are: the velocity $\boldsymbol{v} : [0, T] \times \mathcal{D} \to \mathbb{R}^d$, the crystal lattice orientation, i.e. the rotation $\boldsymbol{R} : [0, T] \times \mathcal{D} \to O^{rt}$ where O^{rt} denotes rotations set and the Cauchy stress $\boldsymbol{\sigma} : [0, T] \times \mathcal{D} \to \mathbb{R}_S^{3\times 3}$. Let $\boldsymbol{\sigma} = \boldsymbol{\sigma}' + p\boldsymbol{I}$, where $\boldsymbol{\sigma}'$ is the stress deviator while $p : [0, T] \times \mathcal{D} \to \mathbb{R}$ is the pressure.

The momentum balance in the Eulerian coordinates reads

$$\rho^{mass}(\partial_t \boldsymbol{v} + \boldsymbol{v} \cdot \boldsymbol{\nabla} \boldsymbol{v}) - \mathbf{div}\,\boldsymbol{\sigma}' + \nabla p = \rho^{mass} \boldsymbol{f} \quad \text{in } \mathcal{D}, \tag{2.41}$$

where the mass density $\rho^{mass} > 0$ and the body forces $\boldsymbol{f}$ are supposed to be known. The incompressibility condition is

$$\mathrm{div}\boldsymbol{v} = 0 \quad \text{in } \mathcal{D}. \tag{2.42}$$

The momentum balance equations are completed by the constitutive equation, which relates the stress tensor $\boldsymbol{\sigma}$ and the rate of deformation tensor $\boldsymbol{D}(\boldsymbol{v})$ (see (2.8)) through the evolution equations for each slip system s given by (2.11) or some viscous regularization (2.13) or (2.15).

The boundary $\partial\mathcal{D}$ of the domain $\mathcal{D}$ is decomposed into two disjoint parts, Γ_v and Γ_s, such that the velocity is prescribed on Γ_v and traction is prescribed on Γ_s, at any time t :

$$\boldsymbol{v}(t) = \mathbf{V}(t) \quad \text{on} \quad \Gamma_v, \quad \boldsymbol{\sigma}(t)\boldsymbol{n} = \boldsymbol{S}(t) \quad \text{on} \quad \Gamma_s, \tag{2.43}$$

where $\boldsymbol{n}$ stands for the outward unit normal on $\partial\mathcal{D}$, $\boldsymbol{V}$ is the imposed velocity and $\boldsymbol{S}$ is the prescribed stress vector.

In some situations, as the compression of micro-pillars, we can deal with the bilateral frictional contact on a part of the boundary denoted Γ_c with a rigid body which has the velocity $\boldsymbol{V}^g$. In this case the boundary conditions read:

$$\boldsymbol{v}^r \cdot \boldsymbol{n} = 0,\ |\boldsymbol{\sigma}_T| + \mu_f \sigma_n \leq 0,\ |\boldsymbol{v}_T^r|(|\boldsymbol{\sigma}_T| + \mu_f \sigma_n) = 0,\ \frac{\boldsymbol{v}_T^r}{|\boldsymbol{v}_T^r|} = -\frac{\boldsymbol{\sigma}_T}{|\boldsymbol{\sigma}_T|}, \quad \text{on } \Gamma_c, \tag{2.44}$$

where we have denoted by $\boldsymbol{v}^r(t) = \boldsymbol{v}(t) - \boldsymbol{V}^g(t)$ the relative velocity, by $\sigma_n = \boldsymbol{\sigma}\boldsymbol{n} \cdot \boldsymbol{n}$ the normal stress, by $\boldsymbol{v}_T^r = \boldsymbol{v}^r - (\boldsymbol{v}^r \cdot \boldsymbol{n})\boldsymbol{n}$ the tangential relative velocity and by $\boldsymbol{\sigma}_T = \boldsymbol{\sigma}\boldsymbol{n} - \sigma_n \boldsymbol{n}$ the tangential stress.

We also consider another partition of $\partial\mathcal{D}$ into $\partial_{in}\mathcal{D}(t)$ and $\partial_{out}\mathcal{D}(t)$ corresponding to incoming ($\boldsymbol{v} \cdot \boldsymbol{n} < 0$) and outcoming ($\boldsymbol{v} \cdot \boldsymbol{n} \geq 0$) flux. The boundary conditions associated to the lattice evolution equations (2.9) and of the dislocation evolution equation (2.20) are:

$$\boldsymbol{R}(t) = \boldsymbol{R}^{in}(t), \quad \rho^s(t) = \rho_s^{in}(t), \quad s = 1, .., N, \quad \text{on} \quad \partial_{in}\mathcal{D}(t). \tag{2.45}$$

i.e. a given lattice orientation and a given dislocation densities of the crystal are prescribed on $\partial_{in}\mathcal{D}(t)$. For the simplified model (see Section 2.7) the boundary condition associated to (2.24) reads

$$\theta(t) = \theta^{in}(t), \qquad \text{on} \quad \partial_{in}\mathcal{D}(t), \tag{2.46}$$

To the field equations, we add the initial conditions

$$\boldsymbol{v}(0) = \boldsymbol{v}^0, \quad \boldsymbol{R}(0) = \boldsymbol{R}^0, \quad \rho^s(0) = \rho_0^s, \quad s = 1,..,N \quad \text{in} \quad \mathcal{D}. \tag{2.47}$$

where $\boldsymbol{v}^0$ is the initial velocity and $\boldsymbol{R}^0$ gives the initial orientation of the crystal lattice and $\rho_0^s, s = 1,..,N$ are the initial dislocation density fields. Note that in this model, there is no need to prescribe initial conditions for the stress. This is very convenient since the initial stress field is generally not known or it cannot be easily measured.

2.9   Numerical strategy

To integrate the governing equations, a mixed finite-element and Galerkin discontinuous strategy, developed in [14], will be used. We will give here only the principles of the method used for simulation results in the next sections while a detailed description is given in Annex. Time implicit (backward) Euler scheme is used for the field equations, which gives a set of nonlinear equations for the velocities $\boldsymbol{v}$ and lattice orientation $\boldsymbol{R}$. At each iteration in time, an iterative algorithm is used in order to solve these nonlinear equations. Specifically, the variational formulation (inequality) for the velocity field is discretized using the finite element method, while a finite volume method with an upwind choice of the flux is adopted for solving the hyperbolic equations that describe the evolution of the lattice orientation. One of the advantages of the proposed numerical strategy is that it does not require the consideration of elastic deformation since it is not based on an elastic predictor/plastic corrector scheme (e.g.[116]).

It is to be noted that in the case of the proposed rigid-viscoplastic model (2.15), numerical difficulties arise from the non-differentiability of the viscoplastic terms. That means that one cannot use finite element techniques developed for Navier-Stokes fluids (see for instance [39, 122]). To overcome these difficulties the iterative

decomposition-coordination formulation coupled with the augmented Lagrangian method of [40, 32] was modified. The reason for this modification is that the in the crystal model (2.11) there is the no co-axiality between the stress deviator and the rate of deformation as it is the case in the Bingham model used by [40, 32]. Note that this iterative decomposition-coordination algorithm permits to solve at each iteration the equations for the unit vectors that define the lattice orientation.

Furthermore, if the domain $\mathcal{D}$ occupied by the single crystal (or poly-crystals) varies in time, then an arbitrary Eulerian-Lagrangean (ALE) description was adopted. In the numerical simulations presented in the next sections we use the followings spatial discretization: P2 for the velocity field, P1 for the pressure, P1 discontinuous for the stress field, slip rates, dislocation densities and lattice orientations.

Chapter 3

Orientation attractors in velocity gradient driven processes

3.1   Introduction

The stability of crystallographic orientations plays a pivotal role in the evolution of material textures, particularly during plastic deformation processes. Understanding this stability is essential for characterizing how materials respond to deformation, especially in the context of both mono-and polycrystalline structures. During deformation, lattice orientations tend to stabilize around specific configurations, often referred to as lattice orientation attractors, which are crucial for predicting material behavior under stress.

Deformation-induced texture evolution arises primarily through mechanisms like grain rotation, driven by the activity of slip systems or twinning. This dynamic process leads to the formation of intragranular substructures, where new orientations deviate from the parent grain's initial orientation. Over deformation, these substructures tend to evolve toward preferred orientations shaped by the imposed deformation, which subsequently influences the material's mechanical properties and overall texture [115, 4, 68].

Crystallographic orientation is a key determinant of whether a grain will undergo uniform (homogeneous) or localized (heterogeneous) deformation. Stable orientations typically lead to more uniform deformation, whereas unstable orientations are often linked to strain localization and deformation inhomogeneity. Thus, the stability of crystallographic orientations becomes central to understanding texture development during plastic deformation. This stability analysis for both hexago-

nal close-packed (HCP) and face-centered cubic (FCC) crystal provides insight into how initial crystallographic orientations affect the stability of lattice configurations during deformation [45, 64, 44, 75]. The simulations, employing an Eulerian framework, simulate channel compression under uniform loading with a null rotation rate to isolate the effects of external forces on orientation evolution. An important effort was also done for modeling texture evolution due to dynamic recrystallization of ice to deduce the existence of orientation attractors that maximizes the resolved shear stress on the easiest slip system in the crystal (see [17, 91, 18, 16].

In this chapter we want to investigate the stability of the lattice orientation in a particular case: the velocity gradient driven processes. To simplify our analysis only perfectly plastic models, without hardening/softening effects will be considered. Even if the problem is stated in its general framework, the stability analysis will be done for the simplified 2D model with three slip systems. We will characterize the stable stationary orientations and will deduce their attaction basins, essential in the prediction of the final texture of the poly/mono-crystal.

In the numerical simulations, which illustrate the theory, two specific cases are examined. In the first case, we deal with an homogeneous velocity gradient field with a nonhomegeous initial orientations, modeling the grains of a poly-cristal. Firstly all grains are initialized with orientations belonging to one of two attractors, expected to evolve toward them. We analyze also the situation when the initial orientations are kept the same except for one grain, whose orientation corresponds to a unstable configuration. This comparison illustrates how subtle variations in initial crystallographic orientations can significantly influence both the stability of the material and the distribution of strain within individual grains. The second case deals with a mono-crystal (homogeneous initial orientation) but with a driven non-homogeneous velocity gradient field. A void growth under a radial loading in a mono-crystal is chosen to illustrate this case.

By combining theoretical stability analysis with these numerical simulations, this chapter offers a comprehensive examination of how initial crystallographic orientations, deformation mechanisms, and applied loading conditions affect the stability and evolution of lattice orientations.

3.2 Stability analysis and attractors of crystal orientation

We will suppose in this section that we deal with a velocity gradient driven processes, i.e. $\boldsymbol{L} = \boldsymbol{L}^*$ is given and let us denote by $\boldsymbol{D}^* = (\boldsymbol{L}^* + \boldsymbol{L}^{*T})/2$ the driven rate of deformation and by $\boldsymbol{W}^* = (\boldsymbol{L}^* - \boldsymbol{L}^{*T})/2$ the driven rotation tensor. To simplify our analysis we shall not consider here any hardening or softening effects. Bearing in mind that $\boldsymbol{M}_s = \boldsymbol{R}\boldsymbol{M}_s^0\boldsymbol{R}^T$ then the slip rate decomposition of $\boldsymbol{D}^*$ (2.8) can be rewritten as $\boldsymbol{R}^T\boldsymbol{D}^*\boldsymbol{R} = \sum_{s=1}^N \dot{\gamma}^s \boldsymbol{M}_s^0$. Hence the plastic (or viscoplastic) constitutive law (2.17) will give the slip rates $\dot{\gamma}^s$ as function of $\boldsymbol{R}$ only, ie.

$$(\dot{\gamma}^1(\boldsymbol{R}), \dot{\gamma}^2(\boldsymbol{R}), ..., \dot{\gamma}^N(\boldsymbol{R})) = \arg \min_{\boldsymbol{R}^T\boldsymbol{D}^*\boldsymbol{R} = \sum_{s=1}^N g^s \boldsymbol{M}_s^0} J(g^1, g^2, ..., g^N). \qquad (3.1)$$

We deduce that the differential equation(2.9) is now a Cauchy problem for the rotation tensor $\boldsymbol{R}$

$$\begin{cases} \dot{\boldsymbol{R}}(t) = \boldsymbol{W}^*\boldsymbol{R}(t) - \boldsymbol{R}(t) \left(\sum_{s=1}^N \dot{\gamma}^s(\boldsymbol{R}(t))\boldsymbol{Q}_s^0 \right). \\[4mm] \boldsymbol{R}(0) = \boldsymbol{I} \end{cases} \qquad (3.2)$$

Tha main objective of this section is to obtain a stability analysis of the above differential equation to get some insights of possible attractors of the lattice rotation. We have mention here that, due to the complexity of the problem, we are not able to do an explicit stability analysis in the general case. However we would like to introduce here a generic methodology useful in approaching different particular problems (see next section).

Let us first introduce the stationary lattice rotations $\boldsymbol{R}^{st}$ as the solution of the right hand side of the above evolution equation:

$$\boldsymbol{W}^*\boldsymbol{R}^{st} = \boldsymbol{R}^{st} \left(\sum_{s=1}^N \dot{\gamma}^s(\boldsymbol{R}^{st})\boldsymbol{Q}_s^0 \right). \qquad (3.3)$$

The above equation for the stationary rotations is nonlinear and very diffcult to solve in the set of orthogonal tensors $\mathcal{O} = \{\boldsymbol{Q} \; ; \; \boldsymbol{Q}^T = \boldsymbol{Q}^{-1}\}$. The fact that $\mathcal{O}$ is not a vectorial space is another difficulty which occurs when we would like to use the linear stability theory to distinguish between the stable and unstable stationary

rotations. That is why it could be more convenient to describe the lattice rotation by the three Euler angles $\boldsymbol{\theta} = (\theta_1, \theta_2, \theta_3)$ with respect to $Ox_1x_2x_3$ Eulerian coordinates. That means that $\boldsymbol{R}$ is a composition of three rotations $\boldsymbol{R} = \boldsymbol{R}(\theta_1 - \theta_1^0, \boldsymbol{e}_1)\boldsymbol{R}(\theta_2 - \theta_2^0, \boldsymbol{e}_2)\boldsymbol{R}(\theta_3 - \theta_3^0, \boldsymbol{e}_3)$, where we have denoted by $\boldsymbol{R}(\theta_i, \boldsymbol{e}_i)$ the rotation with angle θ_i around the axis Ox_i and by $\boldsymbol{\theta}^0 = (\theta_1^0, \theta_2^0, \theta_3^0)$ the initial orientation of the crystal. Then the Cauchy problem (3.2) could be written in terms of Euler angles as

$$\begin{cases} \dot{\boldsymbol{\theta}}(t) = \boldsymbol{\mathcal{F}}(\boldsymbol{\theta}(t), \boldsymbol{D}^*, \boldsymbol{W}^*). \\ \boldsymbol{\theta}(0) = \boldsymbol{\theta}^0. \end{cases} \tag{3.4}$$

Let us mention here that the above differential equation is generic, that means that we are not able to get a specific expression of the function $\boldsymbol{\mathcal{F}}$ in the general case. Only in some simple cases we are able to do it, as for instance (3.9) obtained in the next section.

To describe the lattice orientation attractors we have firstly to compute the stationary (or invariant) lattice orientation, denoted by $\boldsymbol{\theta}^{st}$, as the solution of the folowing system:

$$\boldsymbol{\mathcal{F}}(\boldsymbol{\theta}^{st}, \boldsymbol{D}^*, \boldsymbol{W}^*) = 0. \tag{3.5}$$

The attractors are linearly stable stationary lattice orientations. One can characterize the stability of $\boldsymbol{\theta}^{st}$ through the eigenvalues $\lambda_q(\boldsymbol{\theta}^{st}), q = 1, .., N$ of the matrix

$$T_{sp} = \frac{\partial \mathcal{F}_s}{\partial \theta_p}(\boldsymbol{\theta}^{st}).$$

If

$$Re(\lambda_q(\boldsymbol{\theta}^{st})) < 0 \quad \text{for all } q = 1, 2, 3 \tag{3.6}$$

then $\boldsymbol{\theta}^{st}$ is linearly stable and it is an attractor $\boldsymbol{\theta}^{att}$. That means that there exists a neighborhood $\mathcal{N}$ of $\boldsymbol{\theta}^{att}$ such that if the initial orientation $\boldsymbol{\theta}^0 \in \mathcal{N}$ then $\boldsymbol{\theta}(t) \to \boldsymbol{\theta}^{att}$ for $t \to \infty$.

3.3   Stability analysis of the 2-D model

To apply above stability analysis to get the lattice orientation attractors is a difficult task. Indeed, deriving the expression for $\boldsymbol{\mathcal{F}}$ and solving the non-linear system (3.5) becomes very complex in the general case with numerous slip systems. However, for the 2D model with 3 slip systems, a lot of simplifications occurs. Firstly we

deal with a single angle θ for the lattice orientation description, and we have an analytical decomposition (2.37) instead of a minimization problem (3.1).

Let denote by $d^* > 0$ and $-d^*$ the principal rates of deformation, by $\boldsymbol{d}_1^*, \boldsymbol{d}_2^*$ the principal directions (eigenvectors) of $\boldsymbol{D}^*$, by ω^* the Eulerian rotation rate and let $\psi^*(t)$ be the angle between $\boldsymbol{d}_1^*$ and Ox_1 axis, i.e. we have

$$\boldsymbol{D}^* = d^*(\boldsymbol{d}_1^* \otimes \boldsymbol{d}_1^* - \boldsymbol{d}_2^* \otimes \boldsymbol{d}_2^*), \quad \boldsymbol{W}^* = \omega^*(\boldsymbol{e}_1 \otimes \boldsymbol{e}_2 - \boldsymbol{e}_2 \otimes \boldsymbol{e}_1), \quad \boldsymbol{L}^* = \boldsymbol{D}^* + \boldsymbol{W}^*.$$

Let us deduce here the expressions of $\boldsymbol{\mathcal{F}}$ for the 2D model. For that let us remark that from (2.40) we get

$$\sum_{s=1}^{3} \dot{\gamma}_s = d^* \mathcal{G}(\theta - \psi^*) \tag{3.7}$$

where $\mathcal{G}$ is given by

$$\mathcal{G}(\theta) = \sum_{s=1}^{3} \dot{\gamma}_s^{ref}(\theta), \tag{3.8}$$

while $\dot{\gamma}_s^{ref}(\theta)$ are given in (2.39). In Figure 3.1 we have plotted the non-dimensional function $\mathcal{G}$ for the in-plane deformation of a FCC crystal (green, $\phi = 54.7°$) and of the hexagonal crystal (blue, $\phi = 60°$).

Finally, from (2.24) we deduce the 2D expression of (3.4) :

$$\begin{cases} \dot{\theta}(t) = \dfrac{1}{2}(d^* \mathcal{G}(\theta(t) - \psi^*(t)) - 2\omega^*) \\ \theta(0) = \theta^0. \end{cases} \tag{3.9}$$

In what follows we consider two types of Eulerian strain-driven processes. The first one deals with a constant (in time, i.e. stationary) Eulerian velocity gradient (i.e. $\psi^*(t) = const$) and the second one with a constant (in time, i.e. stationary) Lagrangian velocity gradient (i.e. $\psi^*(t) = const - \omega^* t$).

3.3.1   Stationary Eulerian velocity gradient

We will suppose here that the angle $\psi^*(t)$ of the principal directions of $\boldsymbol{D}^*$ is constant in time, i.e.
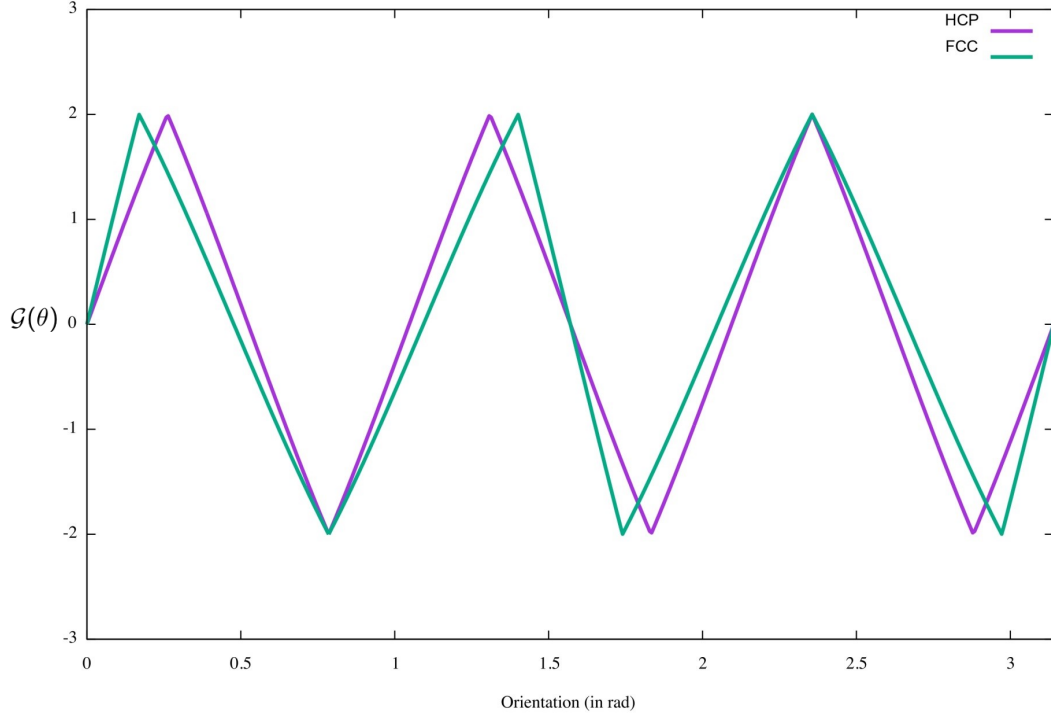
$$\psi^*(t) = \psi_0^*,$$

Figure 3.1: The function $\theta \to \mathcal{G}(\theta)$ in the case of in-plane deformation of a FCC crystal (green, $\phi = 54.7°$) and of the hexagonal crystal (blue, $\phi = 60°$).

and we define a new crystal orientation $\tilde{\theta}(t)$ with respect to $\boldsymbol{d}_1^*$ axis:

$$\tilde{\theta}(t) = \theta(t) - \psi_0^*.$$

Bearing in mind this notation (3.9) reads

$$\begin{cases} \dot{\tilde{\theta}}(t) = \dfrac{1}{2}(d^*\mathcal{G}(\tilde{\theta}(t)) - 2\omega^*), \\ \tilde{\theta}(0) = \tilde{\theta}^0 = \theta^0 - \psi_0^*. \end{cases} \tag{3.10}$$

We can compute now the stationary orientations $\tilde{\theta}^{st}$ as the solution of the non-linear algebraic equation

$$\mathcal{G}(\tilde{\theta}^{st}) = 2\frac{\omega^*}{d^*}. \tag{3.11}$$

Let $\tilde{\theta}^{st}$ be a stationary orientation and suppose that $\mathcal{G}$ is differentiable in $\tilde{\theta}^{st}$. Then

$$\text{if} \quad \mathcal{G}'(\tilde{\theta}^{st}) < 0 \quad \text{then} \quad \tilde{\theta}^{st} \text{ is an attractor.} \tag{3.12}$$

In Figure 3.2 we have plotted the function $\theta \to \mathcal{G}(\theta)$ in the case of in-plane

deformation of a FCC crystal. We remark that this function is piece-wise linear and as it follows from (3.11) the stationary lattice orientation $\tilde{\theta}^{st}$ have to be founded at the intersection of this graph with the horizontal line $y = 2\omega/d$.
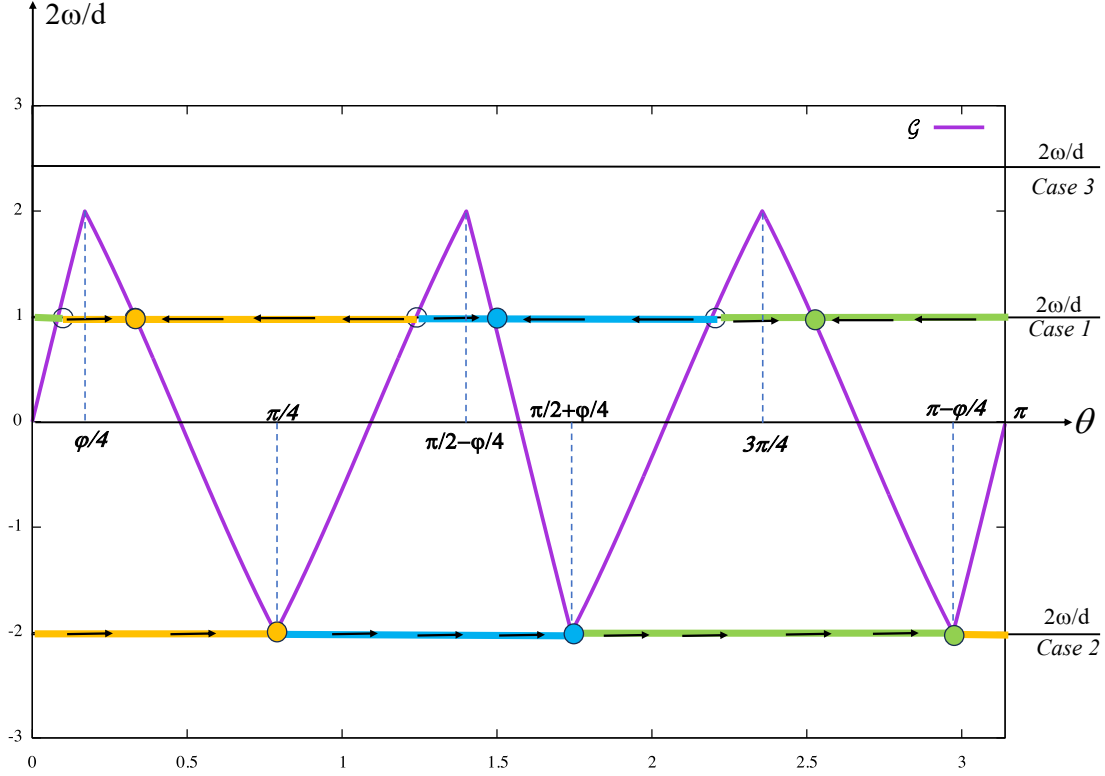

Figure 3.2: The function $\theta \to \mathcal{G}(\theta)$ in the case of in-plane deformation of a FCC crystal. Intersection with the line $y = 2\omega/d$ gives the stationary lattice orientations $\tilde{\theta}^{st}$. The attractors $\tilde{\theta}^{att}$ are the solid colored (orange, blue and green) discs and the colored segments (corresponding to the color of the attractor) represent their attraction basins.

We can distinguish 3 cases :

i) $|\omega^*| < d^*$. In this case, plotted in Figure 3.2, there are 6 stationary orientations $\tilde{\theta}^{st}$) given by

$$\tilde{\theta}_1^{st} = \frac{\omega}{d}\frac{\phi}{4}, \quad \tilde{\theta}_2^{st} = \frac{\phi}{4} + (1 - \frac{\omega}{d})\frac{\pi - \phi}{8}, \quad \tilde{\theta}_3^{st} = \frac{\pi}{4} + (1 + \frac{\omega}{d})\frac{\pi - \phi}{8},$$

$$\tilde{\theta}_4^{st} = \frac{\pi}{2} - \frac{\phi}{4} + (1 - \frac{\omega}{d})\frac{\phi}{4}, \quad \tilde{\theta}_5^{st} = \frac{\pi}{2} + \frac{\phi}{4} + (1 + \frac{\omega}{d})\frac{\pi - \phi}{8}, \quad \tilde{\theta}_6^{st} = \frac{3\pi}{4} + (1 - \frac{\omega}{d})\frac{\pi - \phi}{8}$$

but following (3.12) only three ($\tilde{\theta}_2^{st}, \tilde{\theta}_4^{st}$ and $\tilde{\theta}_6^{st}$) are attractors (stable):

$$\tilde{\theta}_1^{att} = \frac{\phi}{4} + (1 - \frac{\omega}{d})\frac{\pi - \phi}{8}, \quad \tilde{\theta}_2^{att} = \frac{\pi}{2} - \frac{\phi}{4} + (1 - \frac{\omega}{d})\frac{\phi}{4}, \quad \tilde{\theta}_3^{att} = \frac{3\pi}{4} + (1 - \frac{\omega}{d})\frac{\pi - \phi}{8}, \quad (3.13)$$

which are plotted in Figure 3.2 by solid colored (orange, blue and green) discs. Their attraction basins are the intervals plotted in Figure 3.2 by colored segments (corresponding to the color of the attractor) given by

$$B_1^{att} = (\tilde{\theta}_1^{st}, \tilde{\theta}_3^{st}), \quad B_2^{att} = (\tilde{\theta}_3^{st}, \tilde{\theta}_5^{st}), \quad B_3^{att} = (\tilde{\theta}_5^{st}, \pi + \tilde{\theta}_1^{st}).$$

That means that

$$\text{if} \quad \tilde{\theta}_0 \in B_i^{att} \quad \text{then} \quad \tilde{\theta}(t) \to \tilde{\theta}_i^{att} \quad \text{for} \quad t \to \infty, \quad \text{for all } i = 1, 2, 3. \qquad (3.14)$$

In Figure 3.3 we have plotted the numerical simulation of the time evolution of the lattice orientations $t \to (\cos(\theta(t)), \sin(\theta(t)))$ for 200 choices of the initial orientation $\theta_0 \in [0, 2\pi]$ and $\psi_0^* = 0$. We have chosen $d^* = 2\omega^*$ (corresponding to case 1 of Figure 3.2) and the reference strain rate such that the associate reference strain $\gamma = d^* t$ has the same scale as the time t. We remark the presence of 3 different attractors (6 on Figure 3.3 with an π symmetry), as is described by the above theoretical results. Notice that the attrractors work only for large strains, i.e. the distance $|\theta(t) - \theta_i^{att}|$ is small enough only for strains larger than 50%. These large strains occur frequently in the shear bands.

ii) $|\omega^*| = d^*$. In this case, plotted in Figure 3.2, there are 3 stationary orientations $\tilde{\theta}$ given by

$$\tilde{\theta}_1^{st} = \text{sign}(\frac{\omega}{d})\frac{\phi}{4}, \quad \tilde{\theta}_2^{st} = \frac{\pi}{2} + \text{sign}(\frac{\omega}{d})\frac{\pi}{4}, \quad \tilde{\theta}_3^{st} = \frac{\pi}{2} - \text{sign}(\frac{\omega}{d})\frac{\phi}{4}.$$

For all these angles the function $\theta \to \mathcal{G}(\theta)$ is not differentiable but the left and right derivative exists and have opposite signs. Following (3.12) neither are stable (in the classical sense) but they have left or right attractors. Indeed, for $\omega = d$ we have

$$\tilde{\theta}_1^{att} = \frac{\phi}{4}, \quad \tilde{\theta}_2^{att} = \frac{\pi}{2} - \frac{\phi}{4}, \quad \tilde{\theta}_3^{att} = \frac{3\pi}{4}, \quad \text{for } \omega = d, \qquad (3.15)$$

$$B_1^{att} = (\frac{\phi}{4}, \frac{\pi}{2} - \frac{\phi}{4}], \quad B_2^{att} = (\frac{\pi}{2} - \frac{\phi}{4}, \frac{3\pi}{4}], \quad B_3^{att} = (\frac{3\pi}{4}, \pi + \frac{\phi}{4}], \quad \text{for } \omega = d.$$

For $d = -\omega$ the attractors

$$\tilde{\theta}_1^{att} = \frac{\pi}{4}, \quad \tilde{\theta}_2^{att} = \frac{\pi}{2} + \frac{\phi}{4}, \tilde{\theta}_3^{att} = \pi - \frac{\phi}{4}, \quad \text{for } \omega = -d, \qquad (3.16)$$
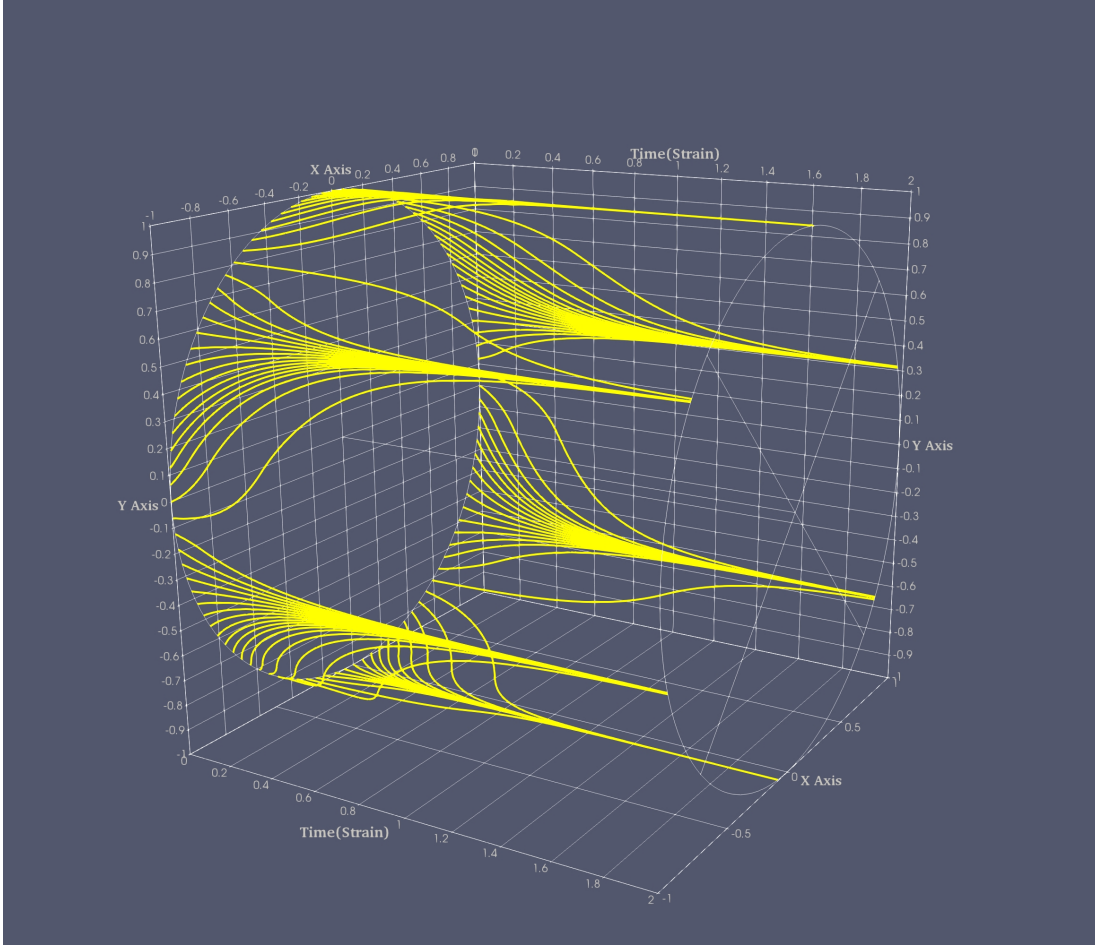
Figure 3.3: Numerical simulation of 200 time/strain trajectories $t \rightarrow (\cos(\theta(t)), \sin(\theta(t)))$ of the crystal orientation in case 1 ($|\omega^*| < d^*$ and $\Psi_0^* = 0$) for different choices of the initial orientation θ_0. For crystal symmetry reasons only 3 attractors of 6 plotted here are different.

are plotted in Figure 3.4 by solid colored (orange, blue and green) discs while their attraction basins

$$B_1^{att} = (-\frac{\phi}{4}, \frac{\pi}{4}], \quad B_2^{att} = (\frac{\pi}{4}, \frac{\pi}{2} + \frac{\phi}{4}], \quad B_3^{att} = (\frac{\pi}{2} + \frac{\phi}{4}, \pi - \frac{\phi}{4}], \quad \text{for } \omega - = d,$$

are the intervals plotted in Figure 3.2 by colored segments (corresponding to the color of the attractor).

For $d^* = -\omega^*$ (corresponding to case 2 of Figure 3.2) we have computed the time evolution of the lattice orientations $t \rightarrow (\cos(\theta(t)), \sin(\theta(t)))$ for 200 choices of the initial orientation $\theta_0 \in [0, 2\pi]$ (see Figure 3.4). We remark the presence of 3 attractors and the lattice orientations trajectories obey (3.14). As before the attractors work only for large strains.

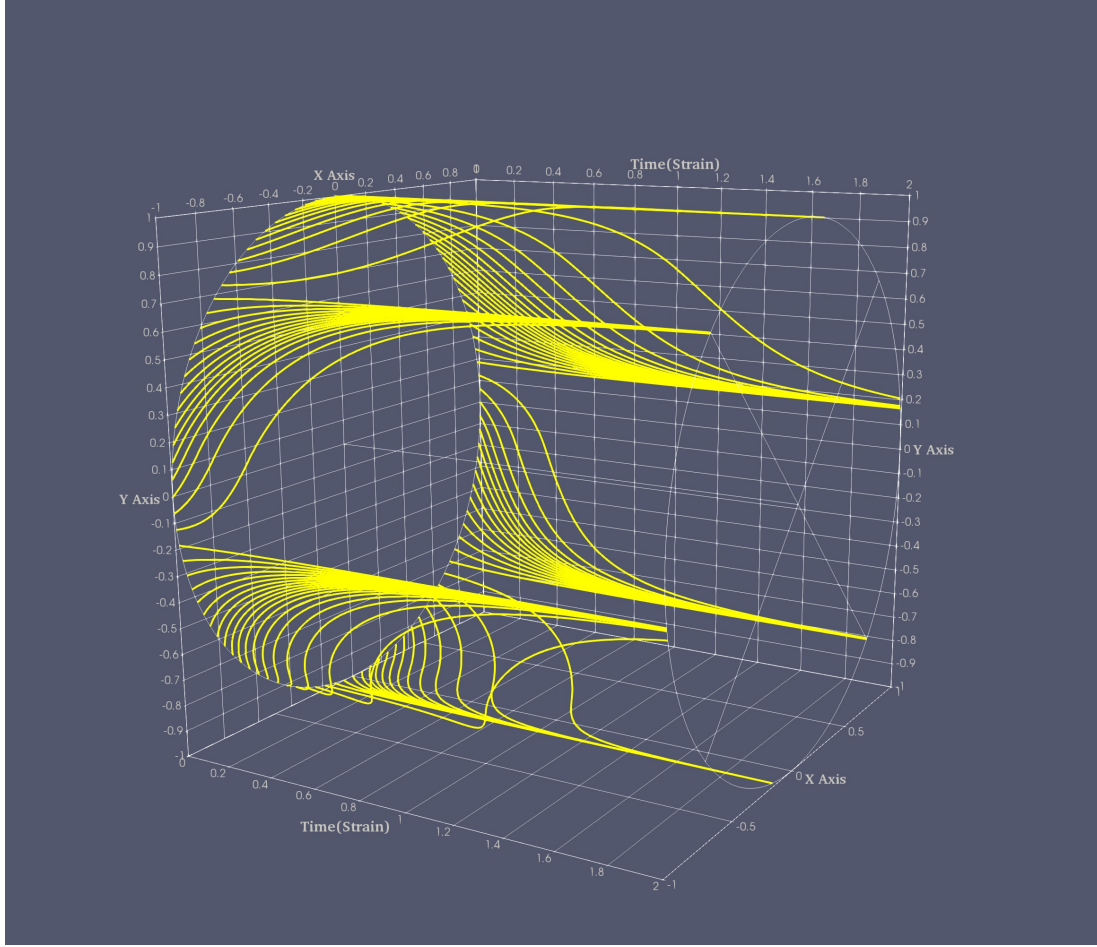iii) $|\omega| > d$. In this case, plotted in Figure 3.2, there are no stationary orien-
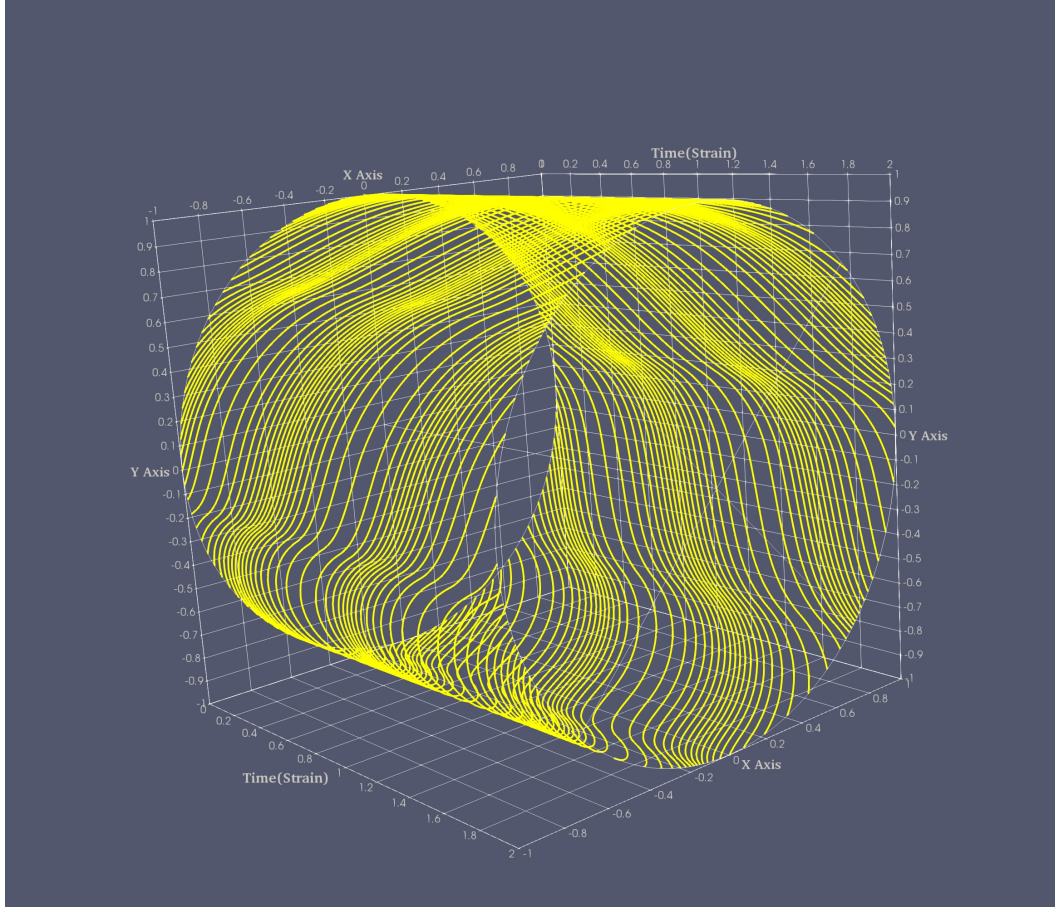
Figure 3.4: Numerical simulation of 200 time/strain trajectories $t \rightarrow (\cos(\theta(t)), \sin(\theta(t)))$ of the crystal orientation in case 2 $(-\omega^* = d^*$ and $\psi_0^* = 0)$ for different choices of the initial orientation θ_0. For crystal symmetry reasons only 3 (left) attractors of 6 plotted here are different.

tations. To see that we have chosen $\omega^* = \dfrac{3}{2}d^* = 1.5$ (corresponding to case 3 of Figure 3.2) and we have plotted in Figure 3.5 the numerical simulation of the time evolution of the lattice orientations $t \rightarrow (\cos(\theta(t)), \sin(\theta(t)))$ for 200 choices of the initial orientation $\theta_0 \in [0, 2\pi]$ and $\psi_0^* = 0$. We remark the absence of any attractor.

3.3.2 Stationary Lagrangian velocity gradient

Let us suppose here that the principal directions of the Eulerain strain rate $\boldsymbol{D}^*$ are rotated with the angle $-\omega^* t$, such that it has the same orientation after the rigid rotation imposed by the spin tensor $\boldsymbol{W}^*$. That is why we will suppose that the angle $\psi^*(t)$ is given by

$$\psi^*(t) = \psi_0^* - \omega^* t,$$

Figure 3.5:   Numerical   simulation   of   200   time/strain   trajectories $t \rightarrow$ $(\cos(\theta(t)), \sin(\theta(t)))$ of the crystal orientation in case 3 ($|\omega| > d$ and $\psi_0^* = 0$) for different choices of the initial orientation θ_0. Note that no attractors are present.

and we define the "rotated" crystal orientation to be

$$\tilde{\theta}(t) = \theta(t) - \psi_0^* + \omega^* t.$$

This situation arrives for the rotation and a radial expansion deformation of the type $\boldsymbol{v}^* = \dfrac{V^* R^*}{r} \boldsymbol{e}_r - \omega^* r \boldsymbol{e}_\varphi$ where r, φ are the Eulerian cylindrical coordinates. In this case $\boldsymbol{d}_1 = \boldsymbol{e}_\varphi, \boldsymbol{d}_2 = \boldsymbol{e}_r$ and $\psi^*(t) = \pi/2 + \varphi - \omega^* t$.

Bearing in mind this notation (3.9) reads

$$\begin{cases} \dot{\tilde{\theta}}(t) = \dfrac{d^*}{2} \mathcal{G}(\tilde{\theta}(t)) \\ \tilde{\theta}(0) = \tilde{\theta}^0 = \theta^0 - \psi_0^*, \end{cases} \tag{3.17}$$

which is exactly (3.10) with $\omega^* = 0$. We can deduce that there are 6 stationary

orientations $\tilde{\theta}^{st}$ given by

$$\tilde{\theta}_1^{st} = 0, \quad \tilde{\theta}_2^{st} = \frac{\pi + \phi}{8}, \quad \tilde{\theta}_3^{st} = \frac{3\pi - \phi}{8}, \quad \tilde{\theta}_4^{st} = \frac{\pi}{2}, \quad \tilde{\theta}_5^{st} = \frac{3\pi + \phi}{8}, \quad \tilde{\theta}_6^{st} = \frac{7\pi - \phi}{8}$$

but following (3.12) only three $(\tilde{\theta}_2^{st}, \tilde{\theta}_4^{st}$ and $\tilde{\theta}_6^{st})$ are attractors (stable):

$$\tilde{\theta}_1^{att} = \frac{\pi + \phi}{8}, \; \tilde{\theta}_2^{att} = \frac{\pi}{2}, \; \tilde{\theta}_3^{att} = \frac{7\pi - \phi}{8}, \tag{3.18}$$

Their attraction basins are the intervals given by

$$B_1^{att} = (\tilde{\theta}_1^{st}, \tilde{\theta}_3^{st}), \quad B_2^{att} = (\tilde{\theta}_3^{st}, \tilde{\theta}_5^{st}), \quad B_3^{att} = (\tilde{\theta}_5^{st}, \pi + \tilde{\theta}_1^{st}).$$

That means that

$$\text{if} \quad \tilde{\theta}_0 \in B_i^{att} \quad \text{then} \quad \tilde{\theta}(t) \to \tilde{\theta}_i^{att} \quad \text{for} \quad t \to \infty, \quad \text{for all } i = 1, 2, 3. \tag{3.19}$$

3.4   Numerical simulations

In this section we present some numerical simulations of the crystal lattice orientation evolution for two different classical problems in crystal plasticity. The first one deals with a poly-crystal (i.e. a non-homogeneous initial orientation) which is loaded with an homogeneous gradient velocity loading. The second one concerns a mono-crystal which is subjected to an isotropic loading, as a void growth under radial expansion. In this case the associated rate of deformation $\boldsymbol{D}^*$ is radial, hence non-homogeneous in space while the initial orientation is homogeneous.

We have to mention here that the in both cases only the boundary conditions are given in relation to a driven velocity field $\boldsymbol{v}^*$ but the computed velocity field $\boldsymbol{v}$ is different from the expected one. Indeed the response of the (poly-)crystal on the boundary loading, could presents slip and/or kink bands, which are too complicated to be well described by the driven velocity field $\boldsymbol{v}^*$. However, in the examples shown here, the overall final orientation of the lattice can be deduced from the apriori attractors distribution predicted by the stability analysis of the previous section.

The material parameter used in this quasi-static computation is not directly specific to a particular material but reflects the order of magnitude typically associated with hexagonal close-packed (HCP) crystals. The material parameters are: density $\rho^{mass} = 3200\text{kg/m}^3$, yield limit $\tau_c^s = 20\text{MPa}$ for all systems with no hardening, and
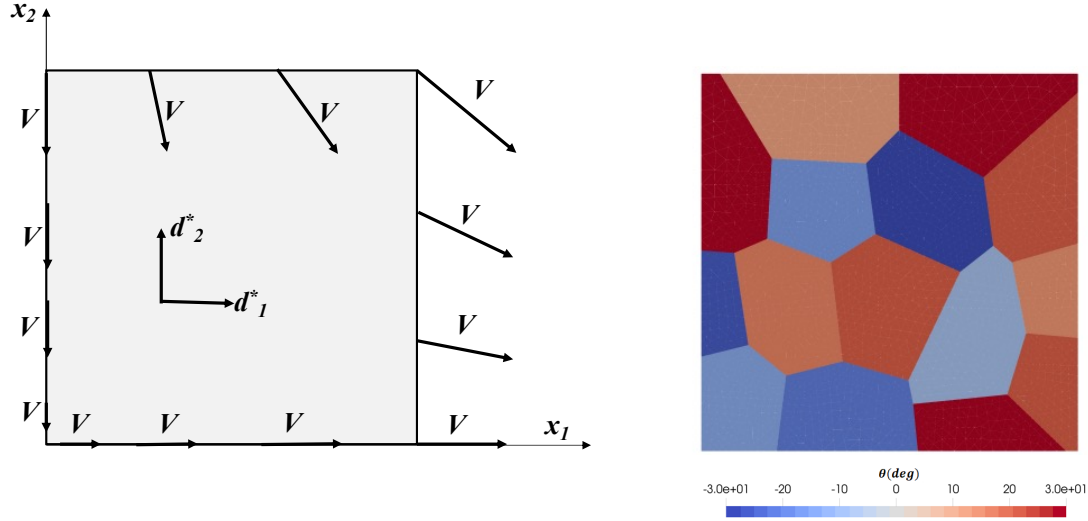
Figure 3.6: Left: schematic representation of a poly-crystal under a homogeneous gradient velocity loading. Right: the distribution $(x, y) \to \theta^0(x, y)$ of the initial on the initial lattice orientation in the color scale $(-30°, 30°)$.

a small viscosity (less than 1% of $\tau_c^s/\dot{\Gamma}_c$, where $\dot{\Gamma}_c$ is the characteristic strain rate) chosen for numerical reasons only.

3.4.1 Homogeneous loading of a poly-crystal

The poly-crystal domain is a rectangle $(0, L(t)) \times ((0, H(t))$, which is a square $(L_0 = H_0)$ at the initial configuration $t = 0$, containing 15 grains of different orientations (see Figure 3.6 right).

On the boundary, denoted by $\Gamma_v(t) = \Gamma(t)$, we impose a velocity $\boldsymbol{V}$ (see Figure 3.6 left), corresponding to the in-compressible Eulerian velocity field $\boldsymbol{v}^* = d^*(x_1 \boldsymbol{e}_1 - x_2 \boldsymbol{e}_2)$, i.e.

$$\boldsymbol{V}(t)(x, y) = d^*(x\boldsymbol{e}_1 - y\boldsymbol{e}_2). \tag{3.20}$$

. The associated gradient of the velocity field $\boldsymbol{v}^*$ is

$$\boldsymbol{L}^* = \boldsymbol{D}^* = d^*(\boldsymbol{e}_1 \otimes \boldsymbol{e}_1 - \boldsymbol{e}_2 \otimes \boldsymbol{e}_2),$$

which is homogeneous and corresponds to the choice

$$\boldsymbol{d}_1^* = \boldsymbol{e}_1, \quad \boldsymbol{d}_2^* = \boldsymbol{e}_2, \quad \omega^* = 0, \quad \psi^* = \psi_0^* = 0.$$

Following the stability analysis of the rotated orientation angle $\tilde{\theta} = \theta$ we deduce that the orientation attractor (plotted in Figure 3.7 middle) is given on each grain

depending on the initial orientation (see Figure 3.6 right) by

$$\theta^{att}(x, y) = \begin{cases} \dfrac{\pi}{6} & \text{if} \quad \theta^0(x, y) \in (0, \dfrac{\pi}{3}) \\[2ex] -\dfrac{\pi}{6} & \text{if} \quad \theta^0(x, y) \in (-\dfrac{\pi}{3}, 0). \end{cases}$$

The initial velocity and the initial crystal orientation where chosen to be

$$\boldsymbol{v}^0(x, y) = \boldsymbol{v}^*(x, y), \quad \theta^0 = \theta^0(x, y). \tag{3.21}$$

Choosing the engineering deformation to be

$$\epsilon^{eng}(t) = \frac{H_0 - H(t)}{H_0}$$

the time period $[0, T]$, the square width H_0 and the strain rate d^* were fixed to correspond to a final engineering deformation $\epsilon^{eng}_{final} = (H_0 - H_{final})/L_0 = 0.5 = 50\%$ (here $H(t)$ is the actual height of the poly-crystal).

In figure Figure 3.7 top we have plotted the evolution of lattice orientation $(x, y) \rightarrow \theta(t, x, y)$ during the deformation process. We remark that globally the lattice orientation is approaching to the estimated attractor $(x, y) \rightarrow \theta(t, x, y)$ (plotted in Figure 3.7 middle) for large strains. The final orientation does not match perfectly with the predicted one but it is very close (less than 5° almost everywhere). That can be seen from the gap between lattice orientation and the estimated attractor

$$(x, y) \rightarrow g(t, x, y) = |\theta(t, x, y) - \theta^{att}(t, x, y)|,$$

plotted in Figure 3.7 bottom. To have a global quantitative measure we have computed the L^2 norm of the gap $g(t)$ given by

$$||g(t)||_2 = \sqrt{\frac{\int_{\Omega(t)} g^2(t, x, y) \, dxdy}{mes(\Omega(t))}},$$

and plotted Figure 3.8. We remark that the L^2 norm has in important decrease till $\epsilon^{eng} = 0.3$, and then it exhibits a plateau around 0.06rad$\approx 3.5°$. Only some grains are not very well estimated. This can be explained by the loss of the strain rate homogeneity, as can be see in Figure 3.9. We remark the presence of some shear bands which at the beginning follows grain boundaries but at the end it seems to
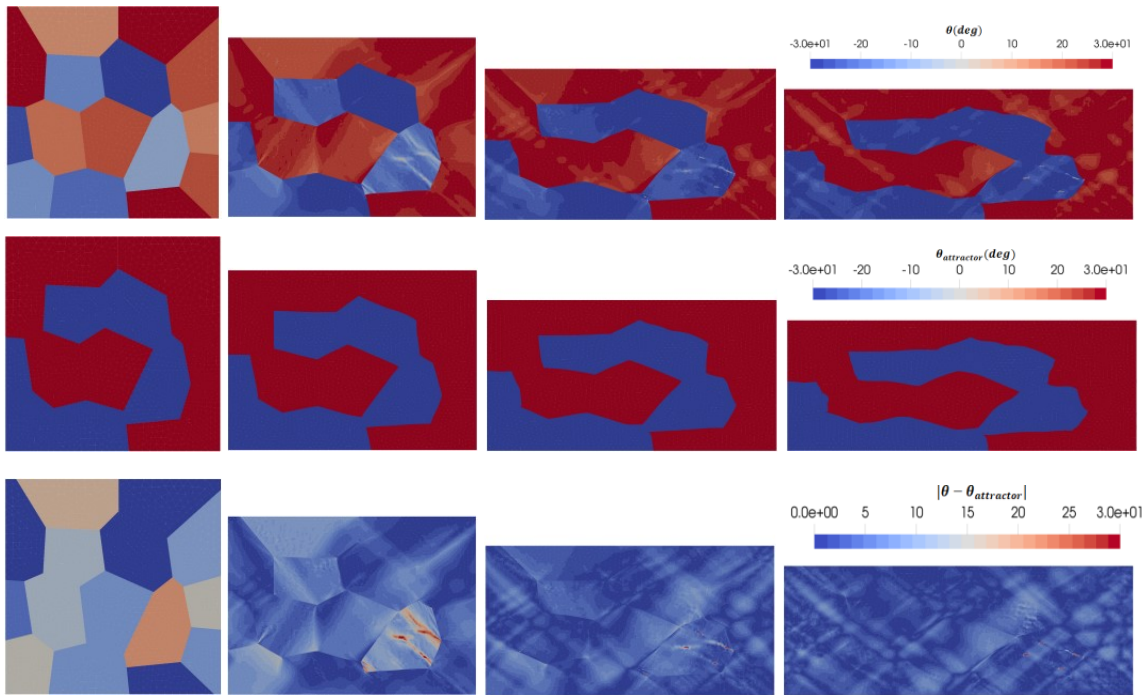
Figure 3.7: Top: the computed Eulerian distribution $(x, y) \to \theta(t, x, y)$ of the lattice orientation in color scale $(-30°, 30°)$. Middle: the expected Eulerian distribution $(x, y) \to \theta^{att}(t, x, y)$ of the orientation attractor in color scale $(-30°, 30°)$ Bottom: the Eulerian distribution $(x, y) \to |\theta(t, x, y) - \theta^{att}(t, x, y)|$ of the difference between lattice orientation and the estimated attractor in color scale $(0, 30°)$. The distributions correspond to $t = 0$ $(\epsilon^{eng} = 0)$, $t = T/3$ $(\epsilon^{eng} = 0.166)$, $t = 2T/3$ $(\epsilon^{eng} = 0.33)$ and $t = T$ $(\epsilon^{eng} = 0.5)$.
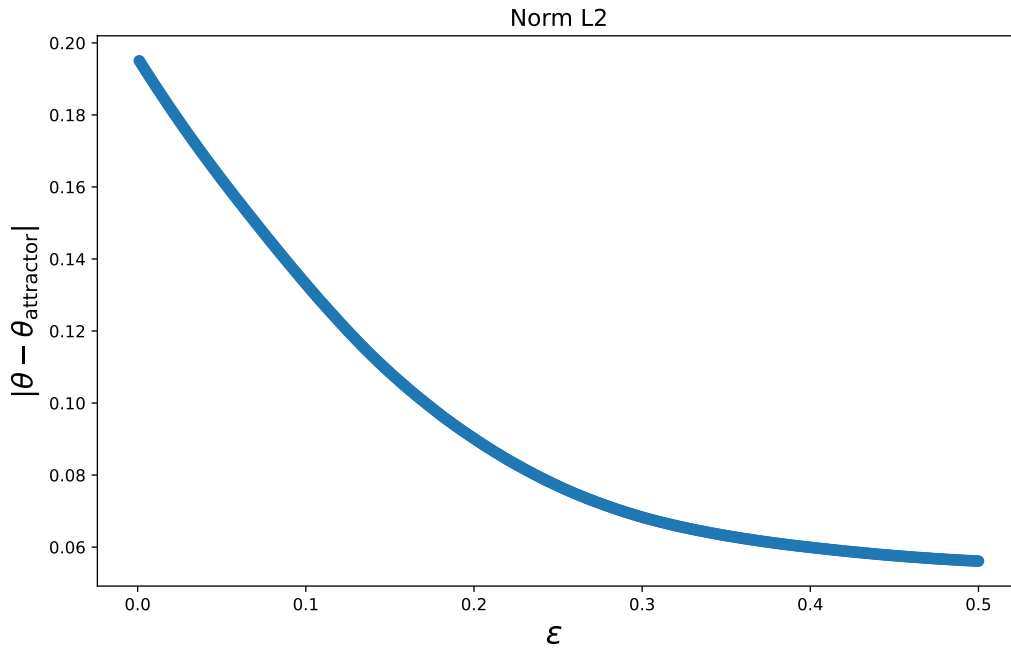
Figure 3.8: Evolution of the gap L^2 norm $||g(t)||_2$ versus the engineering deformation ϵ^{eng}.
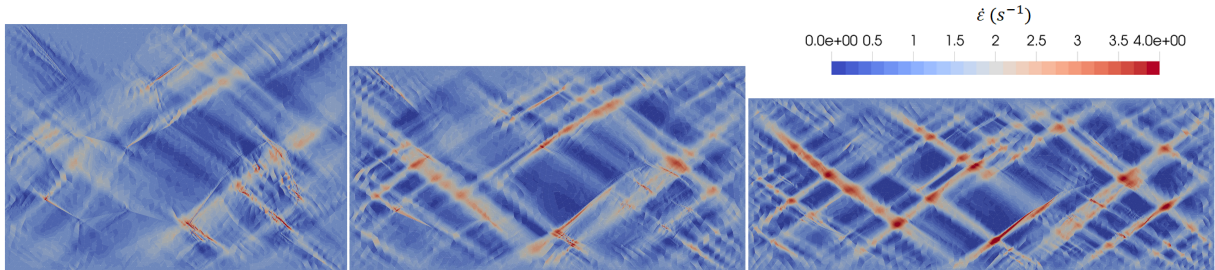

Figure 3.9: The computed equivalent strain rate for $t = T/3$ ($\epsilon^{eng} = 0.166$), $t = 2T/3$ ($\epsilon^{eng} = 0.33$) and $t = T$ ($\epsilon^{eng} = 0.5$).

be associated on the overall geometry of the sample.

The initial choice of grains orientations, presented in Figure 3.6 right, include only grain orientations belonging to an attraction basin. To see what happens if a grain has an unstable stationary orientation we have changed the orientation of upper right grain (see Figure 3.10) to be $\theta = 0$, which is an unstable stationary orientation located between two attraction basins $(-\pi/3, 0)$ and $(0, \pi/3)$. We remark that a part of the grain joints $\theta^{att} = \pi/6$ attractor, another part joins $\theta^{att} = -\pi/6$ attractor, while a third part of the grain presents orientations bands associated to kink or shear bands. We have to mention here that the computations in this regime could be mesh or time-step dependent, hence it is very difficult to predict the final
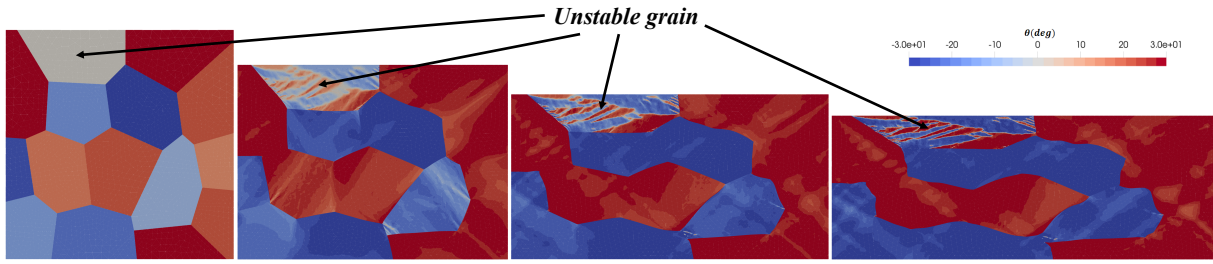
Figure 3.10: The computed Eulerian distribution $(x, y) \rightarrow \theta(t, x, y)$ of the lattice orientation in color scale $(-30°, 30°)$ for $t = 0$ ($\epsilon^{eng} = 0$), $t = T/3$ ($\epsilon^{eng} = 0.166$), $t = 2T/3$ ($\epsilon^{eng} = 0.33$) and $t = T$ ($\epsilon^{eng} = 0.5$). Notice that one grain has an initial unstable orientation.

configuration.

3.4.2 Non-homogeneous loading of a mono-crystal

At initial state the crystal domain is represented by a disc of radius R_0, containing an initially circular void at the center of radius $r_0 = R_0/10$ see Figure 3.11 left. On the external boundary, denoted by $\Gamma_e(t)$, we impose a radial velocity $\boldsymbol{V}$, corresponding to an in-compressible Eulerian velocity field $\boldsymbol{v}^* = \dfrac{V_0 R_0}{r} \boldsymbol{e}_r$ (here r, φ are the cylindrical coordinates), i.e.

$$\boldsymbol{V}(t)(x, y) = \frac{V_0 R_0}{x^2 + y^2}(x\boldsymbol{e}_1 + y\boldsymbol{e}_2), \tag{3.22}$$

while the internal boundary, denoted by $\Gamma_i(t)$, is traction free (i.e. $\mathbf{S}(t) = 0$).

The associated gradient of the velocity field $\boldsymbol{v}^*$ is

$$\boldsymbol{L}^* = \boldsymbol{D}^* = d^*(r)(\boldsymbol{e}_\varphi \otimes \boldsymbol{e}_\varphi - \boldsymbol{e}_r \otimes \boldsymbol{e}_r), \quad d^*(r) = \frac{V_0 R_0}{r^2},$$

which is non-homogeneous and corresponds to the choice

$$\boldsymbol{d}_1^* = \boldsymbol{e}_\varphi(\varphi), \quad \boldsymbol{d}_2^* = \boldsymbol{e}_r(\varphi), \quad \omega^* = 0, \quad \psi^* = \psi_0^* = \varphi + \frac{\pi}{2}.$$

Following the stability analysis of the rotated orientation angle $\tilde{\theta} = \theta - \psi_0^*$ we deduce that the orientation attractor $\theta^{att} = \tilde{\theta}^{att} + \psi_0^*$ is given on each of 6 circular sectors of the plane (see Figure 3.11 right) by

$$\theta^{att}(\varphi) = \varphi - \frac{(k+1)\pi}{3}, \quad \text{for } \varphi \in \left(\frac{(1+2k)\pi}{6}, \frac{(3+2k)\pi}{6}\right), \, k \geq 0.$$
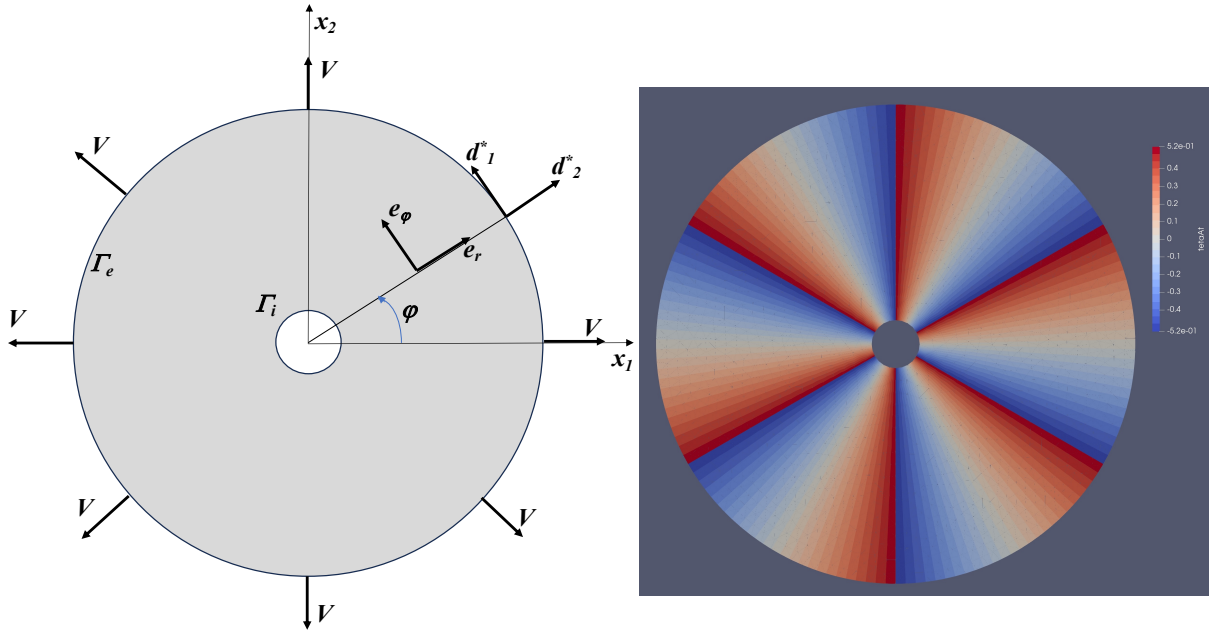
Figure 3.11: Left: schematic representation of a single-crystal with a circular void at its center under a radial velocity loading. Right: the distribution $(x, y) \rightarrow \theta^{att}(x, y)$ of the predicted attractor on the initial configuration in the radian color scale $(-\pi/6, \pi/6)$.

The initial conditions in velocity and in the crystal orientation where chosen to be

$$\boldsymbol{v}^0(x, y) = \boldsymbol{v}^*(x, y), \quad \theta^0 = 0. \tag{3.23}$$

The time period $[0, T]$, the initial external radius R_0 and the velocity V_0 were chosen to correspond to a final engineering volume deformation $\epsilon^{eng}_{final} = 2V_0 T/R_0 = 0.1875 = 18.75\%$. Note that the expected deformation at the void level is $R_0/r_0 = 10$ times higher (around 180%) than on the external boundary.

In figure 3.12 (top) we have plotted the evolution of lattice orientation $(x, y) \rightarrow \theta(t, x, y)$ during the deformation process. We remark that the orientation exhibits a discontinuity on the angles $\varphi = \pi/6 + k\pi/3$ as the attractor does. However the discontinuity is more present near the void, where the deformations are much larger, than near the external boundary. This is in concordance with our stability analysis of the previous section: the distance between the lattice orientation and its attractor decreases significantly for large strains (more than 50%) which are present near the void but are too small on the external boundary. In Figure 3.12 bottom we have plotted distribution $(x, y) \rightarrow |\theta(t, x, y) - \theta^{att}(t, x, y)|$ of the difference
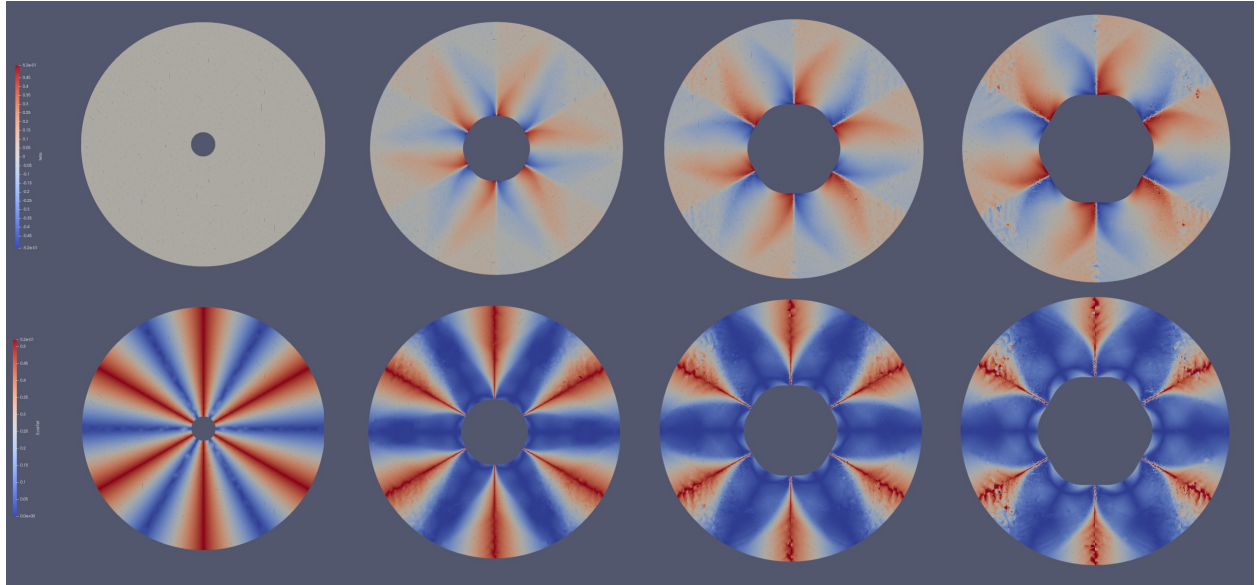
Figure 3.12: Top: the computed Eulerian distribution $(x, y) \rightarrow \theta(t, x, y)$ of the lattice orientation in the radian color scale $(-\pi/6, \pi/6)$. Bottom: the Eulerian distribution $(x, y) \rightarrow |\theta(t, x, y) - \theta^{att}(t, x, y)|$ of the gap between lattice orientation and the estimated attractor in the radian color scale $(0, \pi/6)$. The distributions correspond to $t = 0$ ($\epsilon^{eng} = 0$), $t = T/3$ ($\epsilon^{eng} = 0.0625$), $t = 2T/3$ ($\epsilon^{eng} = 0.125$) and $t = T$ ($\epsilon^{eng} = 0.1875$).

between lattice orientation and the estimated attractor. We remark that globally the blue zones (where the orientation is close to the attractor) are growing during the deformation. However, as explained above, there are some regions (the discontinuity lines $\varphi = \pi/6 + k\pi/3$ and far from the void, plotted in red) where the attractor is not describing the lattice orientation.

We have also to mention that very close the void, at large strains, the deformation process is much more complex: slip and kink bands appears (see Chapter 4). Moreover, during the deformation process, the computed equivalent strain rate is not more radial (see Figure 3.13) as expected from $\boldsymbol{D}^*$. That is why the above analysis based on a simple assumption on the velocity field $\boldsymbol{v}^*$ is less pertinent. This can be seen in Figure 3.12 bottom where at $t = 2T/3$ ($\epsilon^{eng} = 0.125$) and at $t = T$ ($\epsilon^{eng} = 0.1875$) the difference between the lattice orientation and the estimated attractor is a little big larger very near the void.

3.5   Conclusions

This chapter focuses to the stability of the lattice orientation for velocity gradient driven processes. To simplify the problem only perfectly plastic models, without
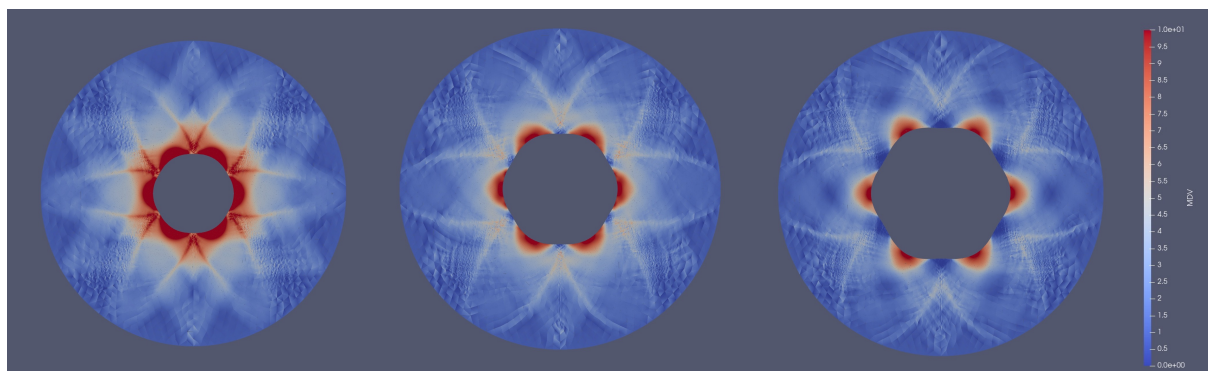
Figure 3.13: The computed equivalent strain rate for $t = T/3$ ($\epsilon^{eng} = 0.0625$), $t = 2T/3$ ($\epsilon^{eng} = 0.125$) and $t = T$ ($\epsilon^{eng} = 0.1875$).
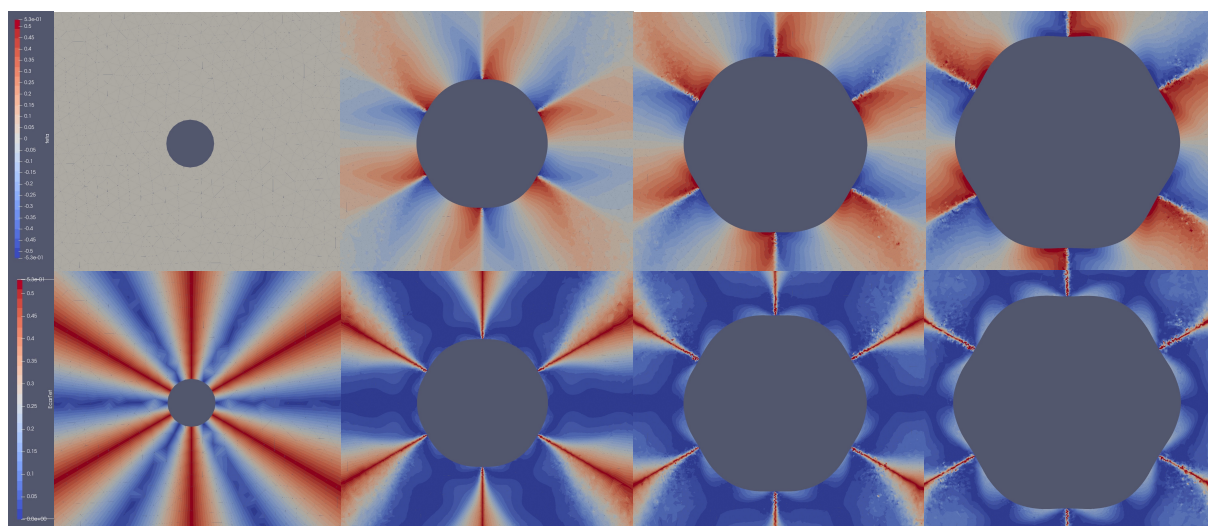

Figure 3.14: Zoom on the void of Figure 3.12. Top: the computed Eulerian distribution $(x, y) \rightarrow \theta(t, x, y)$ of the lattice orientation in the radian color scale $(-\pi/6, \pi/6)$. Bottom: the Eulerian distribution $(x, y) \rightarrow |\theta(t, x, y) - \theta^{att}(t, x, y)|$ of the gap between lattice orientation and the estimated attractor in the radian color scale $(0, \pi/6)$. The distributions correspond to $t = 0$ ($\epsilon^{eng} = 0$), $t = T/3$ ($\epsilon^{eng} = 0.0625$), $t = 2T/3$ ($\epsilon^{eng} = 0.125$) and $t = T$ ($\epsilon^{eng} = 0.1875$).

hardening/softening effects were considered. The general problem of lattice orientation stability analysis is very difficult to explicitly formulate in a mathematical framework for which tools as linear stability could be used. That is why we have restricted ourselves to the simplified 2D model with three slip systems. We have theoretically characterized the stable stationary orientations and have computed their attraction basins, essential in the prediction of the final texture of the poly/monocrystal. Since the attractors are effective for slip strains larger than 50% this stability analysis, which concerns large deformations, is not so useful for small strains.

To illustrate the theory, we have done numerical simulations for two specific problems. In both cases only the boundary conditions are given in relation to the driven velocity field but the computed velocity field is different from the expected one. However, the overall final orientation of the lattice can be deduced from the a priori attractors distribution predicted by the stability analysis.

The first case, a homogeneous driven velocity gradient field with a nonhomegeous initial orientations, modeling the grains of a poly-crystal, is considered. Since all grains are initialized with orientations belonging to one of two attractors, the stability analysis gives the expected final texture of the poly-crystal. The computed orientation is in a very good accord with the predicted one with a gap average (in L^2 norm) less than 4°. The situation when only one grain has an initial unstable orientation is also analyzed. We found that this grain develops a lot of shear bands but globally it has a limited effect on the global orientation of the poly-crystal. This comparison illustrates how subtle variations in initial crystallographic orientations can significantly influence the distribution of strain within individual grains.

In the second case we have considered a mono-crystal (homogeneous initial orientation) but with a driven non-homogeneous velocity gradient: void growth under radial loading. The numerical simulations point out that, accordingly with stability analysis, the orientation exhibits a discontinuity on the angles $\varphi = \pi/6 + k\pi/3$, as the attractor does. These discontinuities are present near the void, where the deformations are large enough, and vanish near the external boundary where the deformation is small and the attractor is not effective. Very close the void, at large strains, the deformation process is much more complex: slip and kink bands appears and the strain rate is far from the driven one. That is why the difference between the lattice orientation and the estimated attractor is a little big larger very near the void.

Chapter 4

Dislocation density attractors in slip driven processes

4.1 Introduction

The objective of this study is to perform a stability analysis on some established dislocation density-based models: the Kocks and Mecking (KM) model, Kocks-Mecking model, Kocks-Mecking-Estrin model, and CLZ model. This analysis aims to identify the conditions leading to the attainment of stationary (saturation) states in the active slip systems. Additionally, we seek to evaluate the linear stability of these states to determine whether they demonstrate attractor characteristics.

Although the dislocation-density based CP models we consider are inherently size-independent, our analytical investigations uncover unexpected and 'indirect' size-dependent outcomes. Specifically, we demonstrate that size effects can manifest through variations in the initial dislocation density, particularly noticeable in FIB-prepared samples where the initial dislocation density decreases as the sample diameter increases [62]. This phenomenon significantly influences whether the material experiences softening or hardening processes.

Building on our analytical treatment, we conduct numerical simulations to simulate the compression of micro pillars of varying sizes in an Eulerian crystal plasticity approach adept at describing very large deformations. Our motivation stems from the burgeoning field of nanotechnology, where the production of nano-scale structures has underscored the importance of understanding material behavior at submicron levels [41, 27, 35]. Given the widespread utilization of micrometric sensors in industries like transportation and energy, comprehending how size impacts

a material's mechanical response has become paramount.

Our key discovery is that certain aspects of microstructural evolution observed in small-scale materials can be effectively captured using dislocation-density based CP models. This finding holds promising implications for the design of miniaturized mechanical devices and innovative materials.

4.2   Stability analysis and attractors

In this section we will consider a slip driven process, which in our context means that the slip function $t \to \gamma^s(t)$ are given for a significant time period $[0,T]$. The N slip systems can be classified between N_a active slip systems and N_i inactive slip systems ($N = N_a + N_i$). To be more precisely let $A_c \cup A_i$ be a partition of $\{1,..,N\}$ and let denote by $\boldsymbol{\rho}_a$ the vector containing all active slip systems $\rho^s, s \in A_c$, for which $|\dot{\gamma}^s| > 0$, and by $\boldsymbol{\rho}_i$ the vector with all inactive slip systems $\rho^s, s \in A_i$, for which $\dot{\gamma}^s = 0$. Following (2.20) the dislocation densities of inactive slip systems will rest constant, i.e. $\boldsymbol{\rho}_i(t) = \boldsymbol{\rho}_i(0) = \boldsymbol{\rho}_i^0$, while the active ones will satisfy the following Cauchy problem

$$
\begin{cases}
\dot{\rho}^s(t) = & \dfrac{1}{b}\left(\mathcal{M}^s(\boldsymbol{\rho}_a(t), \boldsymbol{\rho}_i^0) - \mathcal{A}^s(\boldsymbol{\rho}_a(t), \boldsymbol{\rho}_i^0)\right)|\dot{\gamma}^s(t)|, \\
\rho^s(0) = & \rho_0^s, \quad s \in A_c.
\end{cases}
\tag{4.1}
$$

Let $\dot{\gamma}^{ref}$ be a reference slip rate and let denote by $\gamma = \dot{\gamma}^{ref}t$ the reference slip. For simplicity we consider only constant slip rates, i.e. $\dot{\gamma}^s(t) = \dot{\gamma}^{ref}g_s$. Since the model considered here are time independent the differential system (4.1) can be recasted in terms of γ as

$$
\begin{cases}
\dfrac{d\rho^s}{d\gamma} = & \dfrac{1}{b}\left(\mathcal{M}^s(\boldsymbol{\rho}_a(\gamma), \boldsymbol{\rho}_i^0) - \mathcal{A}^s(\boldsymbol{\rho}_a(\gamma), \boldsymbol{\rho}_i^0)\right)|g^s|, \\
\rho^s(0) = & \rho_0^s, \quad s \in A_c.
\end{cases}
\tag{4.2}
$$

To describe the dislocation density's attractors (which can be called also "saturation dislocation density") we have firstly to compute the stationary (or invariant) dislocation densities, denoted by the vector $\tilde{\boldsymbol{\rho}}_a$, as the solution of the folowing system:

$$
\mathcal{M}^s(\tilde{\boldsymbol{\rho}}_a, \boldsymbol{\rho}_i^0) = \mathcal{A}^s(\tilde{\boldsymbol{\rho}}_a, \boldsymbol{\rho}_i^0), \quad s \in A_c.
\tag{4.3}
$$

We remark that if $\boldsymbol{\rho}_a^0 = \tilde{\boldsymbol{\rho}}_a$ then $\boldsymbol{\rho}_a(t) = \tilde{\boldsymbol{\rho}}_a$ for all $t \in [0,T]$. The attractors are

linearly stable stationary dislocation densities. One can characterize the stability of $\tilde{\boldsymbol{\rho}}_a$ through the eigenvalues $\lambda^q(\tilde{\boldsymbol{\rho}}_a, \boldsymbol{\rho}_i^0), q = 1, ..N_a$ of the matrix

$$S_{sp} = (\frac{\partial \mathcal{M}^s}{\partial \rho^p}(\tilde{\boldsymbol{\rho}}_a, \boldsymbol{\rho}_i^0) - \frac{\partial \mathcal{A}^s}{\partial \rho^p}(\tilde{\boldsymbol{\rho}}_a, \boldsymbol{\rho}_i^0))|g^s|, \quad s, p \in A_c.$$

If

$$Re(\lambda^q(\tilde{\boldsymbol{\rho}}_a, \boldsymbol{\rho}_i^0)) < 0 \quad \text{for all } q = 1, ..N_a \tag{4.4}$$

then $\tilde{\boldsymbol{\rho}}_a$ is linearly stable and it is an attractor, called in the next *saturation dislocation density* and denoted by $\tilde{\boldsymbol{\rho}}_a^{sat}$. That means that there exists a neighborhood $\mathcal{N}$ of $\tilde{\boldsymbol{\rho}}_a^{sat}$ such that if $\boldsymbol{\rho}_a^0 \in \mathcal{N}$ then $\boldsymbol{\rho}_a(t) \to \tilde{\boldsymbol{\rho}}_a^{sat}$ and $\boldsymbol{\tau}_0(t) \to \boldsymbol{\tau}_c^{sat} = \boldsymbol{\mathcal{T}}_c(\tilde{\boldsymbol{\rho}}_a^{sat}, \boldsymbol{\rho}_i^0)$.

4.2.1   Initial dislocation density and size effects

The impact of initial dislocation density on the mechanical response in monocrystals is significant, as shown in several studies [95, 13, 97, 11, 105]. These studies emphasize that variations in microstructure, particularly initial dislocation density, can arise due to differences in sample size and/or fabrication methods.

For instance, the situation when the fabrication method change or alters the microstructure, micropillars milled from bulk single crystals using a focused ion beam (FIB), this process shapes the pillars by bombarding the target's surface with gallium-accelerated heavy ions, modifying the microstructure of specimens with a large surface-to-volume ratio. This modification includes introducing an additional dislocation network, decorating dislocations with gallium, or forming gallium precipitates [29, 67]. The FIB preparation effect on mechanical response is strong for ordered bulk material (low dislocation density) and becomes more pronounced with deceasing sample size. As a result, the initial dislocation density increases with decreasing sample dimensions [24]. This inverse relationship between sample size and initial dislocation density is referred to in the literature as a 'size effect,' which is notably absent in conventional bulk plasticity. Furthermore, it has been reported that regardless of sample preparation, two (Cu) nano-specimens with the same initial microstructure exhibit identical mechanical responses, even if their sizes differ [62]. This observation suggests that the initial microstructure may have a more significant impact than size, leading to a preference for discussing the "initial microstructure effect" rather than the "size effect".

4.2.2   Self interaction dislocations

We consider here the dislocation interraction limited to self interaction, which means that the dislocation multiplication and annihilation rates for the slip system s depends only on ρ^s, i.e. $\mathcal{T}^s(\boldsymbol{\rho}) = \mathcal{T}^s(\rho^s), \mathcal{M}^s(\boldsymbol{\rho}) = \mathcal{M}^s(\rho^s), \mathcal{A}^s(\boldsymbol{\rho}) = \mathcal{A}^s(\rho^s)$ for all systems s. For Kocks and Mecking's model (2.21) "self interaction" means $d^{sp} = a^{sp} = 0$ for $s \neq p$.

For self interaction dislocations is not more necesesary to distinguish between the active and inactive systems as in the previous section. To find the stationary dislocation densities $\tilde{\rho}^s$ the nonlinear sytem (4.3) reduces to a nonlinear equation

$$\mathcal{M}^s(\tilde{\rho}^s) = \mathcal{A}^s(\tilde{\rho}^s) \tag{4.5}$$

while the condition (4.4), which assure that a stationary density is an attractor (or a saturation density), reads

$$\frac{d}{d\rho}\mathcal{M}^s(\tilde{\rho}^s) < \frac{d}{d\rho}\mathcal{A}^s(\tilde{\rho}^s). \tag{4.6}$$

For Kocks and Mecking's model (2.21) we found from (4.5) two stationary densities for each slip system

$$\tilde{\rho}^s = 0, \quad \text{and} \quad \tilde{\rho}^s = \frac{a^{ss}}{(2y_c k)^2},$$

but according to (4.6) only the second one is stable that means that we deal with a single attractor or saturation dislocation density $\tilde{\rho}^s_{sat}$ which corresponds to a saturation CRSS $\tau^s_{c,sat}$.

$$\tilde{\rho}^s_{sat} = \frac{a^{ss}}{(2y_c k)^2}, \quad \tau^s_{c,sat} = \tau_0 + \frac{\alpha \mu b \sqrt{d^{ss}a^{ss}}}{2y_c k}, \tag{4.7}$$

For generalized Kocks-Mecking-Estrin (KME) model [30] the formula of the saturation dislocation density is

$$\tilde{\rho}^s_{sat} = \left(\frac{\tilde{K}_1 + \sqrt{\tilde{K}_1^2 + 4\,b\,k_2 k_0}}{2\,b\,k_2} \right)^2 \text{ with } k_0 = \frac{\tilde{K}_0}{D_m} \tag{4.8}$$

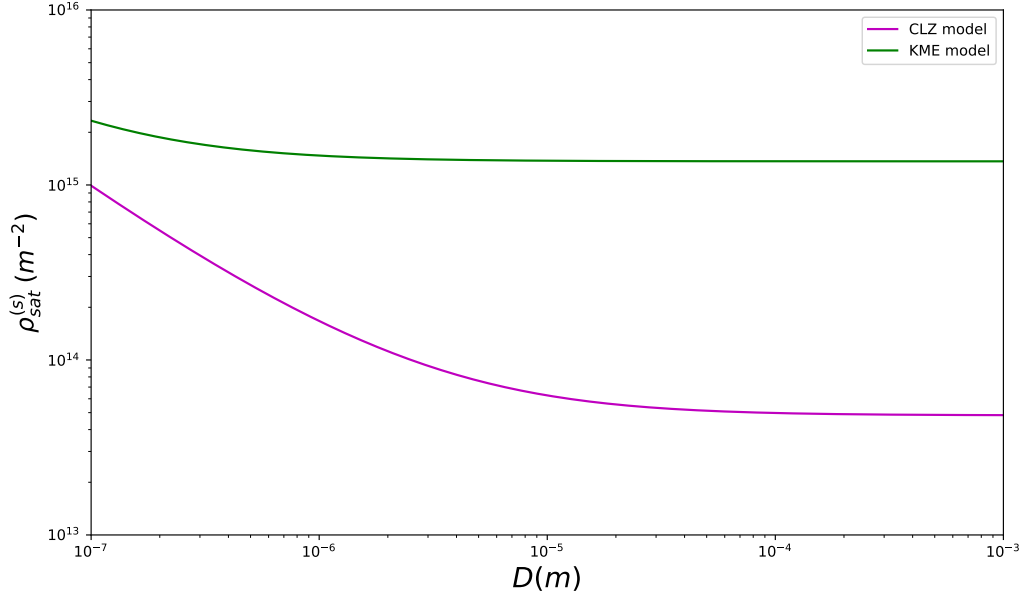For CLZ model [24] the saturation dislocation density and the saturation CRSS are

Figure 4.1: The saturation dislocation densities $\tilde{\rho}_{sat}^s$ of KME and CLZ model versus diameter sample

$$\tilde{\rho}_{sat}^s = \left(\frac{k_f + \sqrt{k_f^2 + 4\,b\,\frac{y}{D}[\frac{1}{2\xi} - 2\cos^2(\beta/2)]}}{2\,y} \right)^2, \tag{4.9}$$

$$\tau_{c,sat}^s = \tau_0 + \alpha\mu b\sqrt{\tilde{\rho}_{sat}^s} + \frac{k\mu b}{\bar{\lambda}} \quad \text{with } \xi = \frac{\bar{\lambda}}{D} \approx 0.3.$$

The influence of variations in average grain size on the saturation dislocation density, as outlined in Fig. 4.1, is minimal when computed using the KME model. Consequently, there is only a minor size-effect observed on the saturation dislocation density. In contrast, the saturation dislocation density of the CLZ model exhibits a sensitivity to diameter, especially between 200 nm and 10 μm when the dislocation saturation value decreases by approximately a factor of 6.

In conclusion for self interaction dislocations we can expect three different scenarios, depending of the initial condition $\rho_0{}^s$ of the density dislocation:

- (i) If $\rho_0^s < \tilde{\rho}_{sat}^s$ then $\rho^s(t) \nearrow \tilde{\rho}_{sat}^s$ and we deal a with a hardening process $\tau_c^s(t) \nearrow \tau_{c,sat}^s$ up to a maximal critical resolved shear stress;

- (ii) if $\rho_0^s > \tilde{\rho}_{sat}^s$ then $\rho^s(t) \searrow \tilde{\rho}_{sat}^s$ and we deal a with a softening process $\tau_c^s(t) \searrow \tau_{c,sat}^s$ down to a minimal critical resolved shear stress;

- (iii) if $\rho_0^s \approx \tilde{\rho}_{sat}^s$ then $\rho^s(t) \approx \tilde{\rho}_{sat}^s$ and we deal a with a plateau $\tau_c^s(t) \approx \tau_{c,sat}^s$.

The recognition that initial dislocation density determines whether a material undergoes a softening or hardening deformation process underscores the size-dependence of initial dislocation density. This understanding corroborates the discussion of FIB-prepared samples in Section 4.2.1. Based on this revelation, it can be asserted that although the Kocks-Mecking (KM) model is inherently size-independent, incorporating initial dislocation densities for samples of different sizes reveals distinct differences in deformation processes. Consequently, the KM model's results exhibit size-dependence.

Among the models examined, the KM model uniquely accounts for the interactions between slip systems—both self and cross interactions—while also producing results that are dependent on sample size. Therefore, the KM model is selected to simulate the evolution of dislocation density.

As an example, we have computed in Figure 4.2 (left) the evolution of the dislocation density $t \to \rho^s(t)$ for Ni, physical value are taken from [97, 3] ($\tau_0 = 11$ MPa, $b = 0.24$nm, $y_c = 3.36b$ and k=38), for 8 choices of the initial dislocation densities $\rho_0^s \in [7.5 \times 10^{12}, 5 \times 10^{15}]$, where we have putted the $a^{s,p} = 0$ for $s \neq p$ to get $\tilde{\rho}_{sat}^s$ and $\tau_{c,sat}^s$ as mentioned in equation (4.7). Given the similarity between interaction matrix $a^{s,p}$ and $d^{s,p}$, we have assumed that $a^{s,p} = d^{s,p}$.

We remark that the dislocation densities and the critical resolved shear stress are converging to saturation values as is predicted by the theory. Moreover, this convergence is effective for large values of slips (more than 50%), which are expected only the shear bands.

4.2.3   Cross interaction dislocations

Let analyse here the Kocks and Mecking model for cross interaction dislocations. The nonlinear system (4.3) for stationary dislocation densities $\tilde{\boldsymbol{\rho}}_a$ reads:

$$\sum_{p \in A_c} a^{sp} \tilde{\rho}^p + \rho_{0,i}^s = (2y_c k)^2 (\tilde{\rho}^s)^2, \quad s \in A_c, \tag{4.10}$$

where

$$\rho_{0,i}^s = \sum_{p \in A_i} a^{sp} \rho_0^p, \quad s \in A_c.$$

Generally, the above system cannot be solved analytically and a numerical approach is needed. For instance one can use a Newton-Raphson method or to try to compute
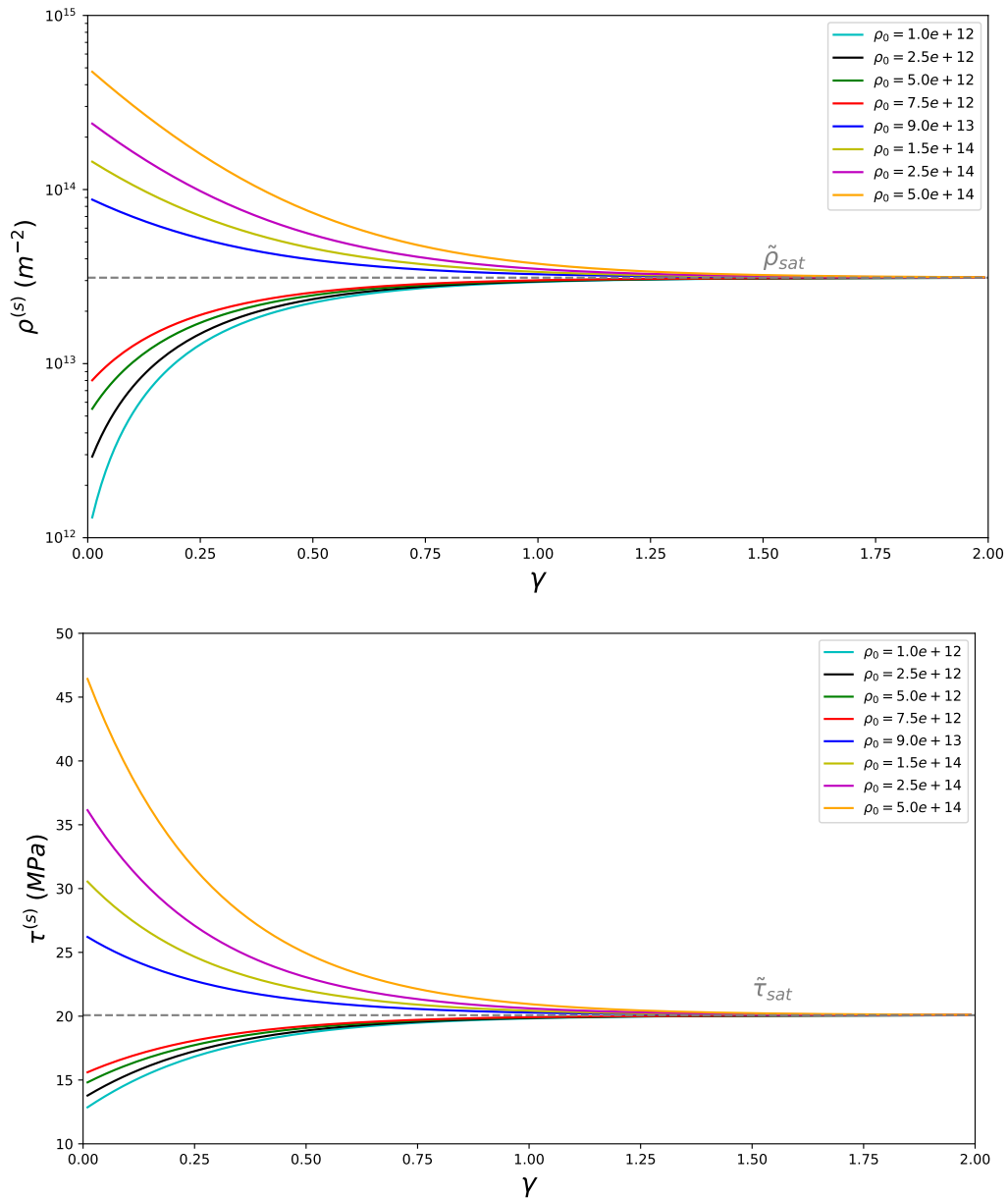
Figure 4.2: Evolution of non-interacting systems of Ni over slip for different initial values. Top : dislocation density over slip, Bottom : shear yield strength over slip.

the local minimizers of the potential function

$$W(\boldsymbol{\rho}_a) = \frac{(2y_ck)^2}{3} \sum_{p \in A_c} (\rho^p)^3 - \frac{1}{2} \sum_{s,p \in A_c} a^{sp} \rho^p \rho^s - \sum_{s \in A_c, p \in A_i} a^{sp} \rho_0^p \rho^s.$$

For the simplicity of the analysis we will suppose in the next that the slip rates $\dot{\gamma}^s = \dot{\gamma}^{ref}$ are the same in all active systems $s \in A_c$, i.e. $g^s = 1$. To see if a solution $\tilde{\boldsymbol{\rho}}_a$ is an attractor we have to compute the eigenvalues of $\tilde{\alpha}_s$ of the matrix

$$\tilde{A}_{sp} = \frac{a^{sp}}{\tilde{\rho}^s}.$$

Then the linear stability condition (4.4) reads

$$Re(\tilde{\alpha}_q) < 2(2y_ck)^2, \quad \text{for all } q = 1, .., N_a. \tag{4.11}$$

Let us mention here a sufficient condition which allow us to compute an analytic solution of (4.10). Let us suppose that the sum of all cross interaction coefficients corresponding to the active slip systems a^{sp} on a line s is the same for all lines, i.e.

$$\sum_{p \in A_c} a^{sp} = a_c, \quad \rho_{0,i}^s = \rho_{0,i}, \quad \text{for all } s \in A_c. \tag{4.12}$$

This is the case in many situations which are detailed in the Appendix I.

If the above property is verified then there exists a uniform solution of (4.10), given by $\tilde{\rho}^s = \tilde{\rho}$ for all $s \in A_c$, where $\tilde{\rho}$ is

$$\tilde{\rho} = \frac{a_c \pm \sqrt{a_c^2 + 4(2y_ck)^2 \rho_{0,i}}}{2(2y_ck)^2}. \tag{4.13}$$

If $\rho_{0,i}$ is not vanishing then only one solution (corresponding to the sign $+$) is non-negative. If $\rho_{0,i} = 0$ (this is always the case if all slip systems are active $A_i = \emptyset$ or if the active and inactive systems are not interacting, i.e. $a^{sp} = 0$ for all $s \in A_c, p \in A_i$) then we deal with two uniform stationary dislocation densities:

$$\tilde{\rho} = 0 \quad \text{and} \quad \tilde{\rho} = \frac{a_c}{(2y_ck)^2}, \quad \text{if } \rho_{0,i} = 0. \tag{4.14}$$

To see if the stationary uniform density is an attractor we have to check the stability condition (4.11). We remark that if (4.12) holds then the largest eigenvalue of matrix $\tilde{A}_{sp}$, corresponding to the uniform eigenvector $(1, .., 1)$, is $\tilde{\alpha}^{max} = a_c/\tilde{\rho}$ and (4.11)

holds always for $\tilde{\rho} > 0$. We deduce that for Kocks-Mecking model we deal with a saturation uniform dislocation density

$$\tilde{\rho}_{sat} = \frac{a_c + \sqrt{a_c^2 + 4(2y_ck)^2\rho_{0,i}}}{2(2y_ck)^2,} \tag{4.15}$$

which corresponds to a saturation critical resolved shear stress

$$\tau_{c,sat}^s = \tau_0 + \alpha\mu b\sqrt{\tilde{\rho}_{sat}\sum_{p\in A_c} d^{sp} + \sum_{p\in A_i} d^{sp}\rho_0^p} \tag{4.16}$$

In order to see the role played by the level of inactive dislocation densities, denoted here by $\rho_{0,i}$, we have computed in Figure 4.3 (Top) the evolution of the dislocation density $\gamma^s \to \rho^s(\gamma^s)$ for Ni in the case of 4 active slip systems for two choices of inactive dislocation densities.

- (i) $\rho_0^p = 10^{11}m^{-2}$ for all $p \in A_i$

- (ii) $\rho_0^p = 10^{14}m^{-2}$, for all $p \in A_i$.

The initial values of the four active dislocation densities were chosen to belong to $[1 \times 10^{13}, 5 \times 10^{15}]m^{-2}$. We remark that the dislocation densities and the critical resolved shear stress are converging to saturation values $\tilde{\rho}_{sat} = 1.117 \times 10^{14}$ for (i) and $\tilde{\rho}_{sat} = 2.584 \times 10^{14}$ for (ii), as is predicted by the theory. The value of the saturation is strongly dependent on the values of inactive dislocation densities. The level of inactive dislocation densities is essential in the evolution of yield limit. Indeed, as it is shown in Figure 4.3 right, in the first case we deal with a hardening process while in the second one we remark a softening behavior.

4.2.4 Simplified model stability analysis

Let us analyse here more in details the simplified model, designated as a 2-D toy model and described in Section 2.7. For simplicity the inactive slip systems are excluded, but the methodology previously described is applied to examine the stability of dislocation density evolution given by the KM model on the three active slip systems. The material parameters where chosen to correspond to Nickel.

We have chosen two initial dislocation densities for all systems

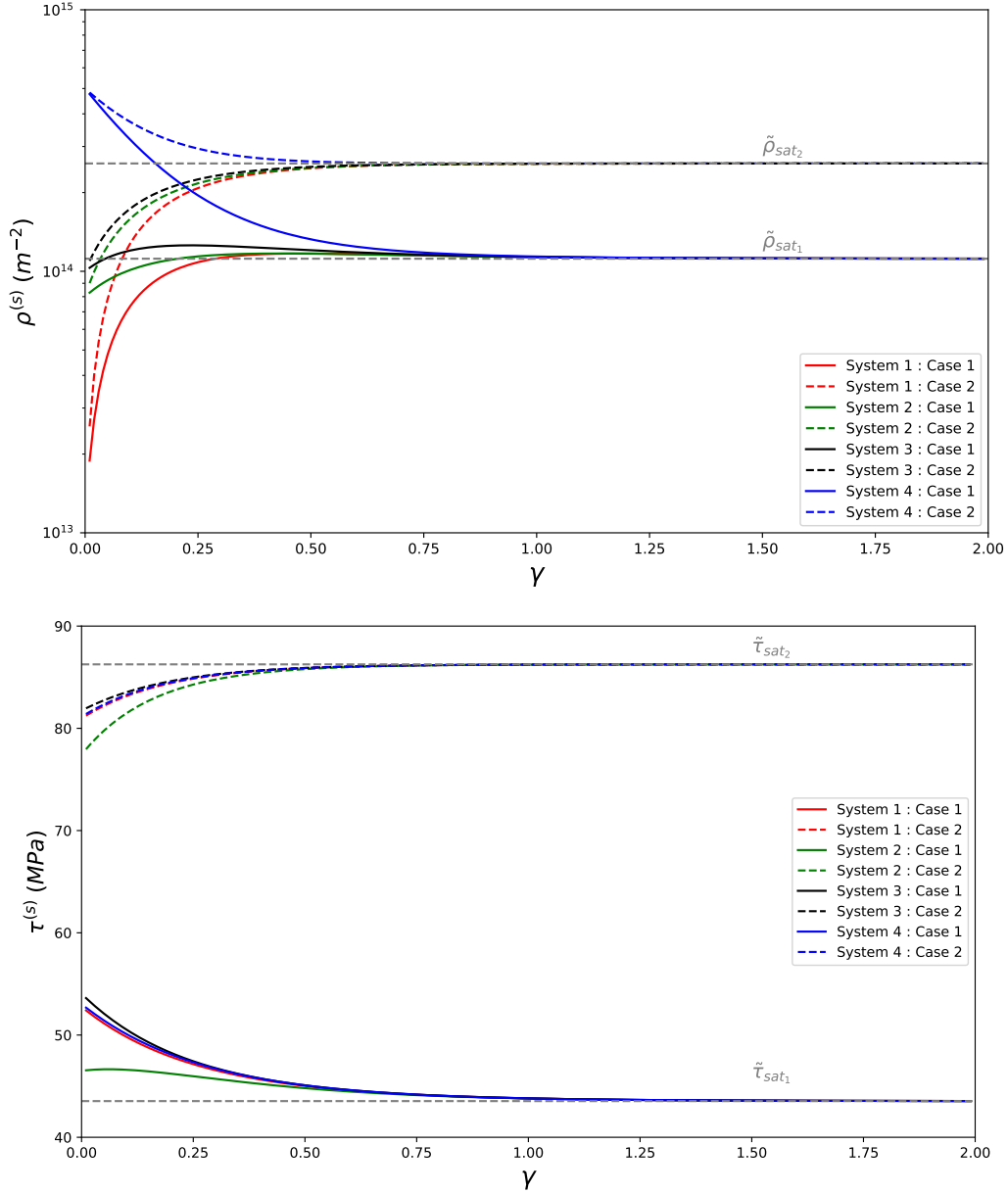- (i) $\rho_0^s = 9 \times 10^{13} \ m^{-2}$ for all $s = 1, 2, 3,$

Figure 4.3: Evolution of four active dislocation densities and shear yield strengths for Ni with a cross-interacting model for two choices (i) and (ii) of the inactive dislocation densities. Top : dislocation densities over slip, Bottom : shear yield strength over slip.

- (ii) $\rho_0{}^s = 7.5 \times 10^{12} \ m^{-2}$ for all $s = 1, 2, 3$.

This choice was done such that we can emphasize a size effect even for size independent models (see Section 4.2.1), corresponding to $D = 1\mu$m for the first one for $D = 20\mu$m in the second one.

Attractors of self interaction dislocations

In the context of self interaction of the simplified model, the expression of saturation dislocation density and the saturation shear yield limit are identical to those expressed in equation (4.7).

In fact, the saturation dislocation density is uniform across the three active systems and size-indepedent. Nevertheless, contrasting behaviors are evident in the two specimens, as depicted in Figure 4.4. The red line represents case i) (smaller specimen), characterized by an initial dislocation density on active system(s) greater than the uniform saturation dislocation density, $\tilde{\rho}_{sat}^s$. Notably, as the dislocation densities converge toward the saturation value, a discernible softening process follows, i.e., $\tau^s(t) \searrow \tilde{\tau}_{c,sat}^s$. In contrast in case ii) (larger specimen) represented by the blue line experiences a hardening phenomenon, characterized by an increase in both dislocation densities and the shear yield limit. This divergent behavior manifests the size-dependency introduced through initial dislocation density.

Attractors of cross interaction dislocations

In the analysis of cross interactions, we utilize equation (4.10) to compute the stationary points. This is a nonlinear system which does not have, generally, analytical solutions. We explore two distinct use cases, one in which an analytical solution exists and another one where a numerical solution is founded.

- UC1 : Active slip systems are subject to (4.12),

- UC2 : Active slip systems do not satisfy (4.12).

<u>**UC1**</u> case. The dislocation interaction matrix associated with the three active slip systems is as follows:

$$A_1 = \begin{pmatrix} a_0 & \zeta & \zeta \\ & a_0 & \zeta \\ symm. & & a_0 \end{pmatrix}$$

with $a_c = \sum_{p=1}^{3} a^{sp} = a_0 + 2\zeta$, for all $s = 1, 2, 3$ and $\zeta = 0.122$. We refer to equation(4.15) and (4.16) to calculate the uniform saturation dislocation density and
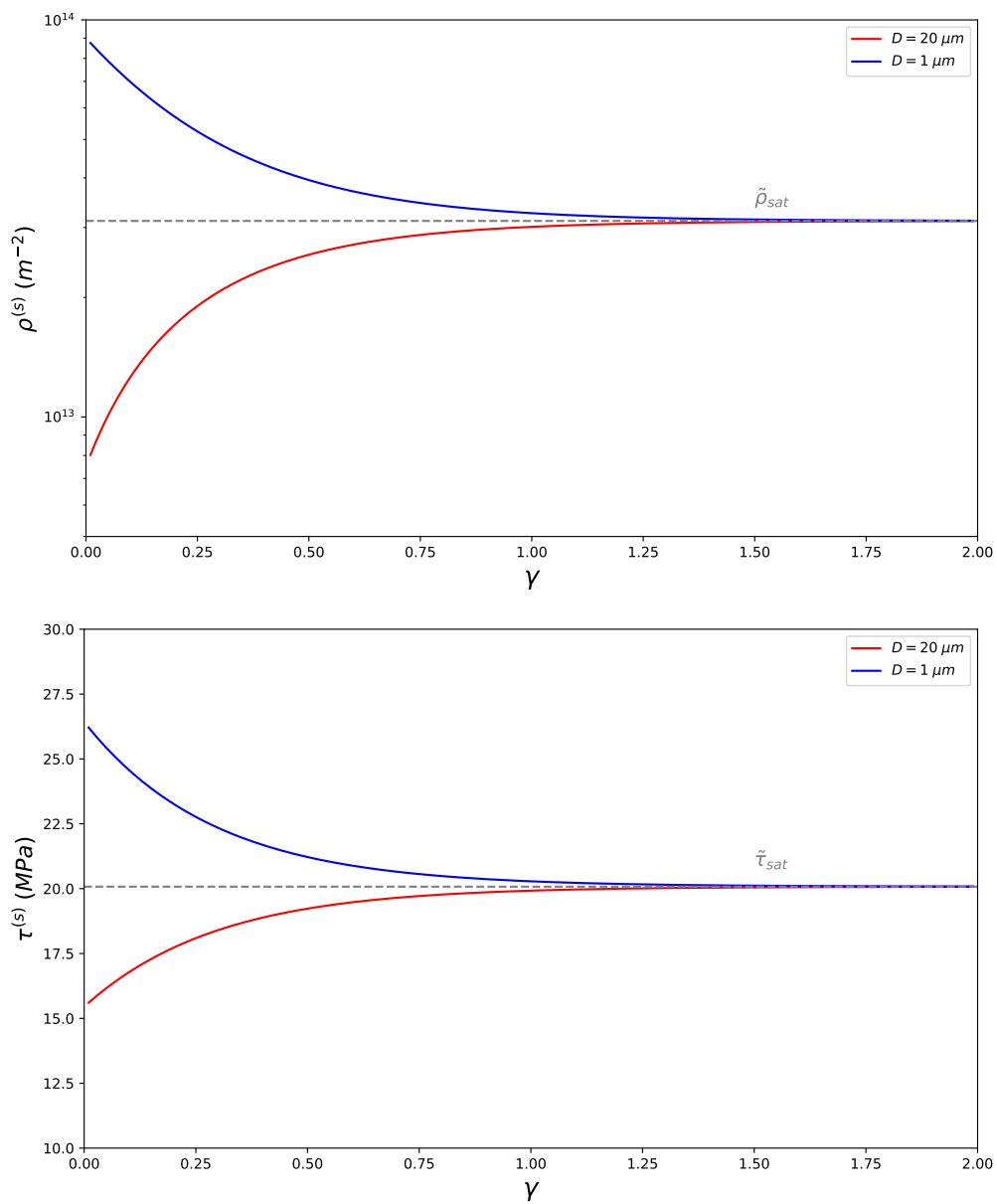
Figure 4.4: Evolution of the self-interaction simplified model for two different initial choices of initial dislocation densities ρ_0^s, corresponding to $D = 1\mu$m (in red) and $D = 20\mu$m in (blue). Left: dislocation densities over slip, Right: shear yield strengths over slip.

uniform saturation shear yield strength. This is achieved by substituting $\rho_{0,i} = 0$ into equation (4.15) and $\rho_0^p = 0$ into equation (4.16).

$$\tilde{\rho}_{sat}^s = \frac{a_c}{(2y_c k)^2}, \quad \tau_{c,sat}^s = \tau_0 + \alpha\mu b \sqrt{\tilde{\rho}_{sat}^s \sum_{p=1}^{3} d^{sp}}$$

In Figure 4.5 we have plotted the system evolution for two different the reference initial choices of initial dislocation densities ρ_0^s and we remark the good agreement with the stability analysis deduced before. It is noteworthy that the uniform saturation dislocation density established in this case is larger than the one determined in self-interaction analysis. The deduced value is three time higher than its self-interaction counterpart, approximately equal to the initial dislocation density of the smaller sample, resulting in a steady state of dislocation density for the smaller specimen.

(UC2)case. The dislocation interaction matrix associated with the three active slip systems is as follows:

$$A_2 = \begin{pmatrix} a_0 & \zeta & \zeta \\ & a_0 & \chi \\ symm. & & a_0 \end{pmatrix}$$

with $\zeta \neq \chi = 0.137$, i.e. $\sum_{p=1}^{3} a^{1p} = a_0 + 2\zeta \neq \sum_{p=1}^{3} a^{2p} = \sum_{p=1}^{3} a^{3p} = a_0 + \zeta + \chi$. The above interaction matrix implies a symmetry between the systems 2 and 3, which means in our context that $\rho^2 = \rho^3$. Since we cannot compute the saturation values we have solved the nonlinear system (4.2). In Figure 4.6 we have plotted the system evolution $\gamma \to \rho^1(\gamma)$ and $\gamma \to \rho^2(\gamma) = \rho^3(\gamma)$ for two different the reference initial choices of initial dislocation densities ρ_0^s. We remark that each dislocation densities have an asymptotic behavior to a saturation value. Rather than displaying a uniform saturation dislocation density and uniform saturation critical resolved shear stress, as found in the self and UC1 cases, UC2 case features two saturation dislocation densities $\tilde{\rho}_{sat}^1$ and $\tilde{\rho}_{sat}^2 = \tilde{\rho}_{sat}^3$ and two saturation critical resolved shear stresses $\tilde{\tau}_{c,sat}^1$ and $\tilde{\tau}_{c,sat}^2 = \tilde{\tau}_{c,sat}^3$. The gap between the two saturation critical resolved shear stresses is insignificant, because the difference between $\sum_{p=1}^{3} a^{1p}$ and $\sum_{p=1}^{3} a^{2p}$ is too small.
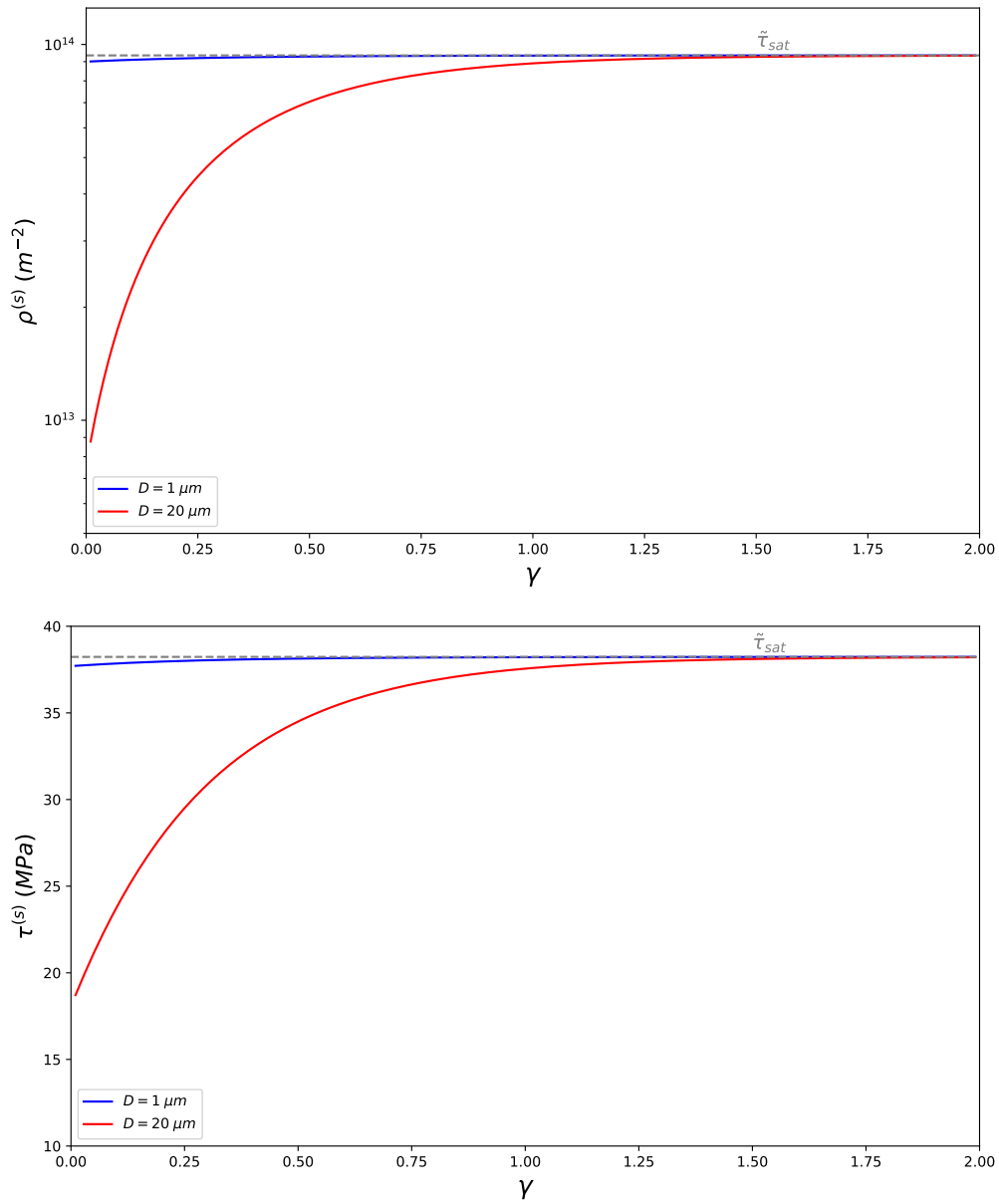
Figure 4.5: Evolution of the cross-interaction simplified model (UC1) for two different initial choices of initial dislocation densities ρ_0^s, corresponding to $D =1\mu$m (in red) and $D =20\mu$m in (blue). Top: dislocation densities over slip, Bottom: shear yield strengths over slip.

4.3 Compression micro-pillars simulations

In this section, we will illustrate the stability analysis described in Section 4.2.4 by performing simulations with the 2D toy model introduced in Section 2.7. It is acknowledged that the reduction from a 3D model to a 2D model, which incorporates only three slip systems, may result in the loss of some detailed information. Despite this simplification, the derived conclusions can still offer significant insights into the underlying physical phenomena. These simulations aim to demonstrate that the behavior of pillars under compression tests is strongly dependent on the initial dislocation density which depend on the pillar size, particularly noticeable in FIB-prepared samples where the initial dislocation density decreases as the sample diameter increases [62].

4.3.1 Numerical simulations setup

All numerical experiments were conducted using Nickel pillars with a consistent geometric aspect ratio of $L_0/D = 2.5$. To streamline the presentation, we present calculations for only two diameters: 1 micrometer and 20 micrometers.

The compression testing methodology is shown schematically in Figure 4.7. The setting mimics the compression experiment commonly conducted on nano and micro scale samples. The (top) surface of the sample is in unilateral frictional contact (friction coefficient $\mu_f = 0.2$)with a rigid plate which moves with a constant (and small) velocity $-V$ on y-axis, the plate movement continues until the sample's final height is reduced by 25% from the initial heigh, deformation takes place in the $x - y$ plane. The other parts of the pillar which is not in contact with the upper plate are traction free whereas on the bottom the sample is fixed.

In all the simulations, the global rate of deformation in all the computations is low $(0.5s^{-1})$, such that the loading could be considered as quasi-static.

For the material coefficients of Nickel, we considered a density of $\rho^{mass} = 8900$ Kg/m^3, a shear modulus equal to $G = 76000$ MPa and the burger vector $b = 0.24$ nm. The KM dislocation density evolution model parameters were set to $K = 38$ and $y_c = 3.36\ b$ while the interaction matrix data can be found in Table 2.1. The case of a in-plane deformation of a FCC crystal, described in Section 2.7.1, was
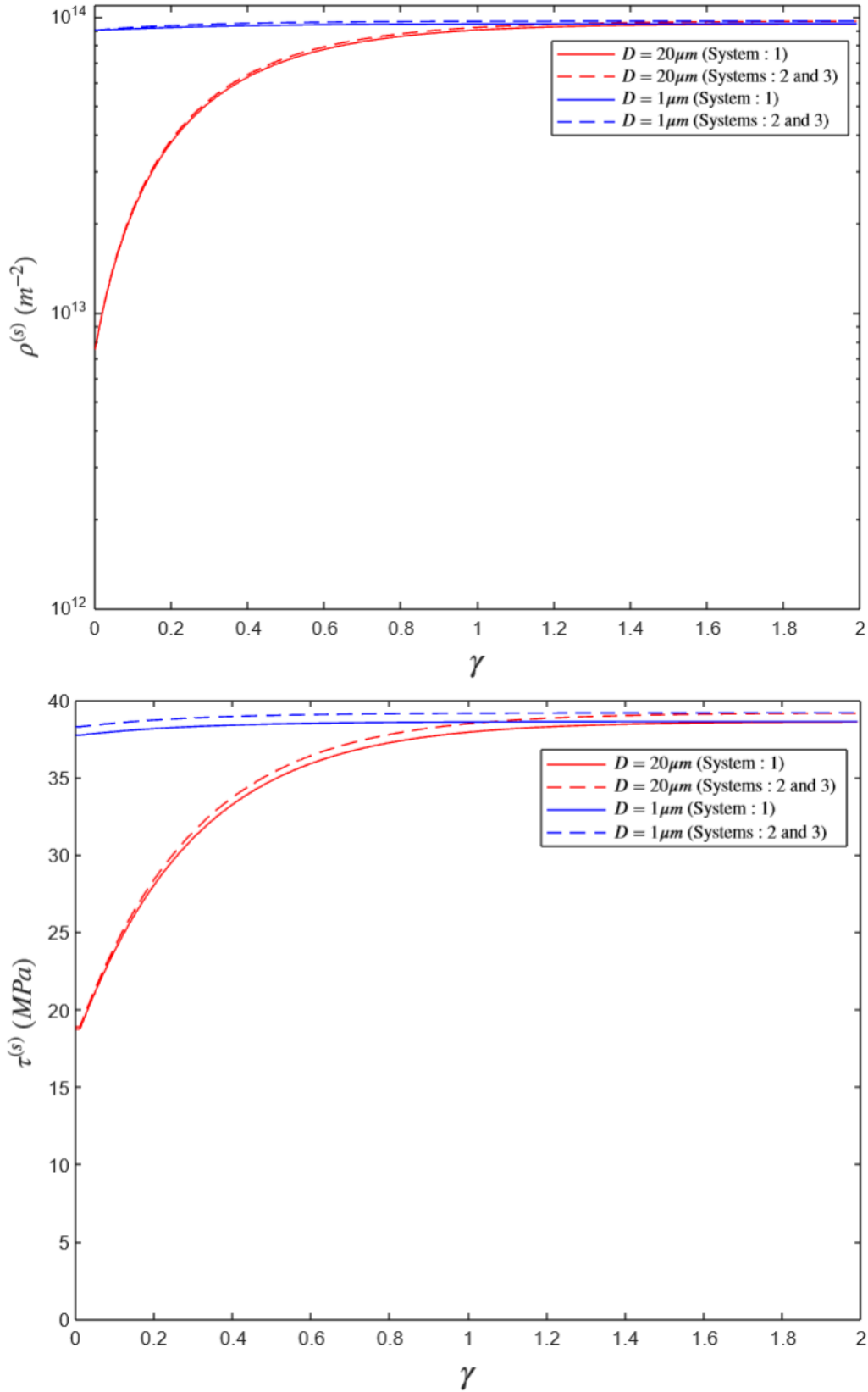
Figure 4.6: Evolution of the cross-interaction simplified model (UC2) for two different initial choices corresponding to $D = 1\mu$m (in red) and $D = 20\mu$m in (blue). Top: $\gamma \rightarrow \rho^1(\gamma)$ and $\gamma \rightarrow \rho^2(\gamma) = \rho^3(\gamma)$ dislocation densities over slip, Bottom: $\gamma \rightarrow \tau_c^1(\gamma)$ and $\gamma \rightarrow \tau_c^2(\gamma) = \tau_c^3(\gamma)$ shear yield strengths over slip.
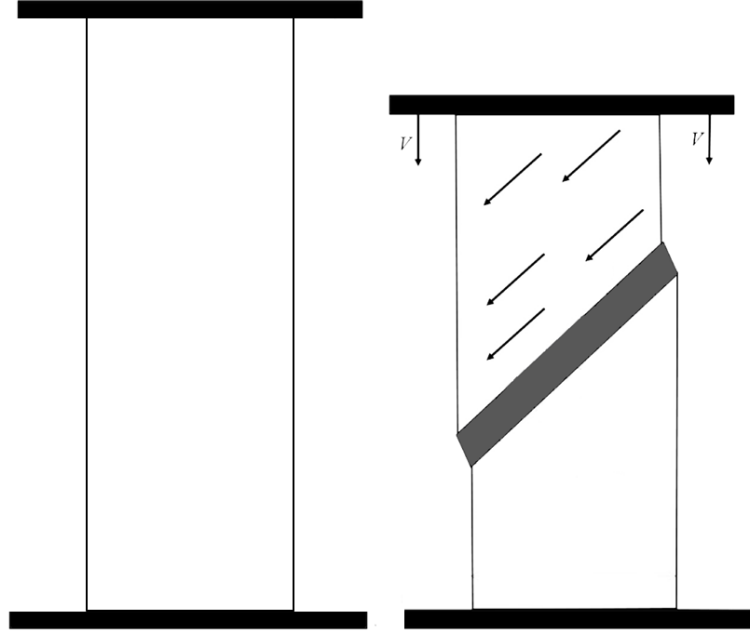
Figure 4.7: A schematic representation of micropillar compression and the formation of a shear band (in grey).

considered in what follows

Initial dislocation densities: The setup follows Section 4.2.4, where two different initial dislocation densities, denoted as (i) and (ii), were considered to capture the size effect, i.e., a change in behavior for two different sample dimensions: $D = 1\mu$m for (i) and $D = 20\mu$m for (ii). All other material coefficients have been considered nearly the same. $\tau_c^k = 26.11$ MPa for (i) and $\tau_c^k = 15.36$ MPa for (ii).

Mesh. To capture the shear bands, we used an adaptive mesh technique based on the strain rate norm $\dot{\epsilon}_p = |\mathbb{D}(\boldsymbol{v})|$, where ϵ_p is the cumulative plastic strain. This means that regions with a higher slip rate have a finer mesh, while regions outside have a coarser mesh. The ratio between the fine and coarse mesh sizes was 1/8. In Fig. 4.8, we have plotted the distribution of cumulative plastic strain ϵ_p at 15% of total deformation for different ratios between the fine and coarse mesh sizes. We found that for the ratio 1/8, the numerical results are not mesh-dependent.

Time step. Since we are using an implicit numerical scheme, the chosen time step is relatively large and corresponds to a deformation of 0.1% between two time steps. As a result, the computational cost is low, allowing the simulations to be performed on a personal computer.

Viscosity. The viscosity was chosen to be as small as possible to ensure the

convergence of the numerical scheme while maintaining the rate-independence of the mechanical model.
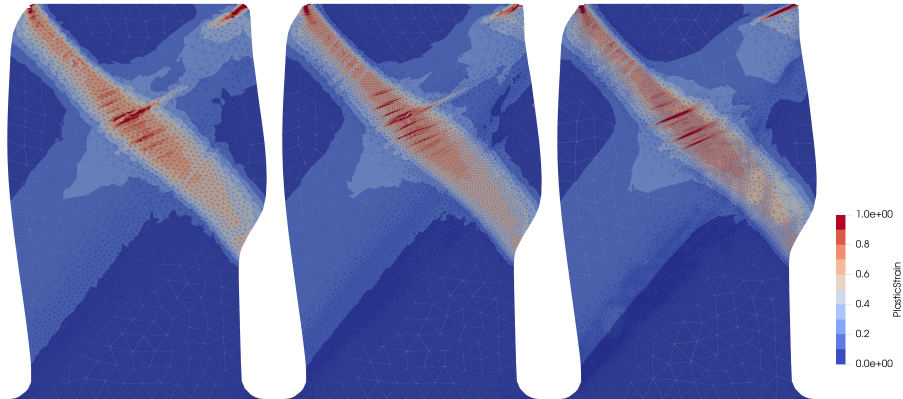

Figure 4.8: The distribution of cumulative plastic strain ϵ_p at 15% of total deformation for different ratio between the sizes of the fine and coarse meshes: 1/4 (left); 1/8 (middle); 1/16(right).

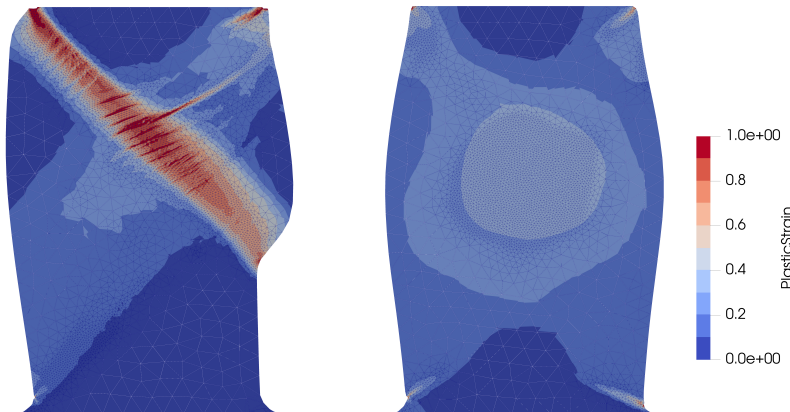### 4.3.2   Self interaction computation

Figure 4.9: Pillar deformation for the self interaction model. Accumulated plastic strain at 18% of total deformation for two choices of initial dislocation densities: case (i) ($D = 1\mu$m) (left) and case (ii) ($D = 20\mu$m) (right).

Firstly, we investigate the compression of pillars under the assumption of self-interaction to analyze the disparities in the mechanical response. As shown in Fig. 4.9, the micro-pillars exhibit qualitatively different deformation processes. In case (i) (smaller pillar), plastic deformation is localized, taking the form of a thin shear band that accumulates almost all the deformation (exceeding 100% of accumulated plastic strain), effectively separating two rigid regions. Conversely, in case (ii) (larger pillar), the response is typical of conventional bulk materials, where the deformation
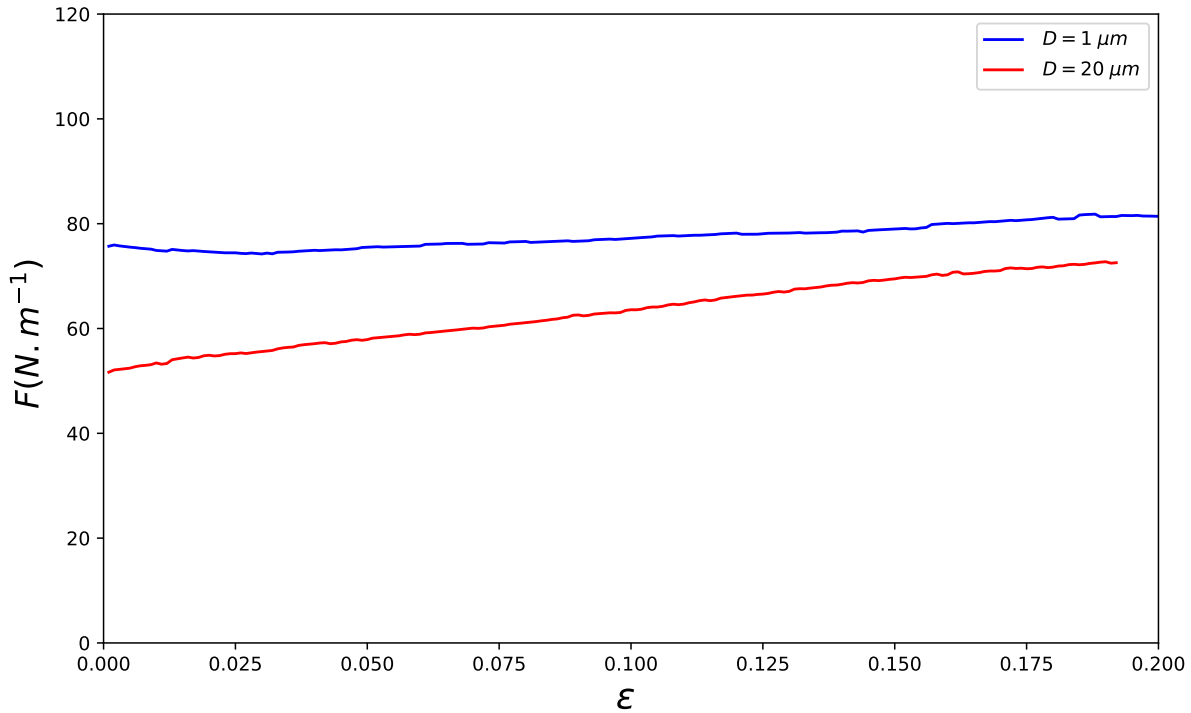
Figure 4.10: Pillar deformation for the self interaction model. Linear Force vs plastic Strain : case (i) ($D = 1\mu$m) (Blue) and case (ii) ($D = 20\mu$m) (Red).

propagates homogeneously, leading to a barrel-shaped pillar. This is illustrated by the spatial distribution of accumulated plastic strain in Fig. 4.9.

Line Load-strain Curve. In Fig. 4.10 the line load or linear force- versus strain curve features size dependency where the linear force for case (i) (smaller sample) remains consistently higher than for case (ii) (larger sample) throughout the deformation process, illustrating the concept that "smaller is stronger". In case (i), the linear force is relatively constant during deformation, while in case (ii), the larger sample shows a progressive increase in linear force. This trend can be attributed to the stability of the sample and how the load is distributed within it. For the localized deformation observed in case (i), plastic deformation occurs mainly through dislocation glide, which limits the increase in load. In instances of highly localized deformation with a thinner band, this can even lead to a sharp drop in load see [112]. In homogeneous deformation, as in case (ii), the load is better distributed resulting in a gradual increase, which suggests that the specimen can undergo further deformation while maintaining stability.

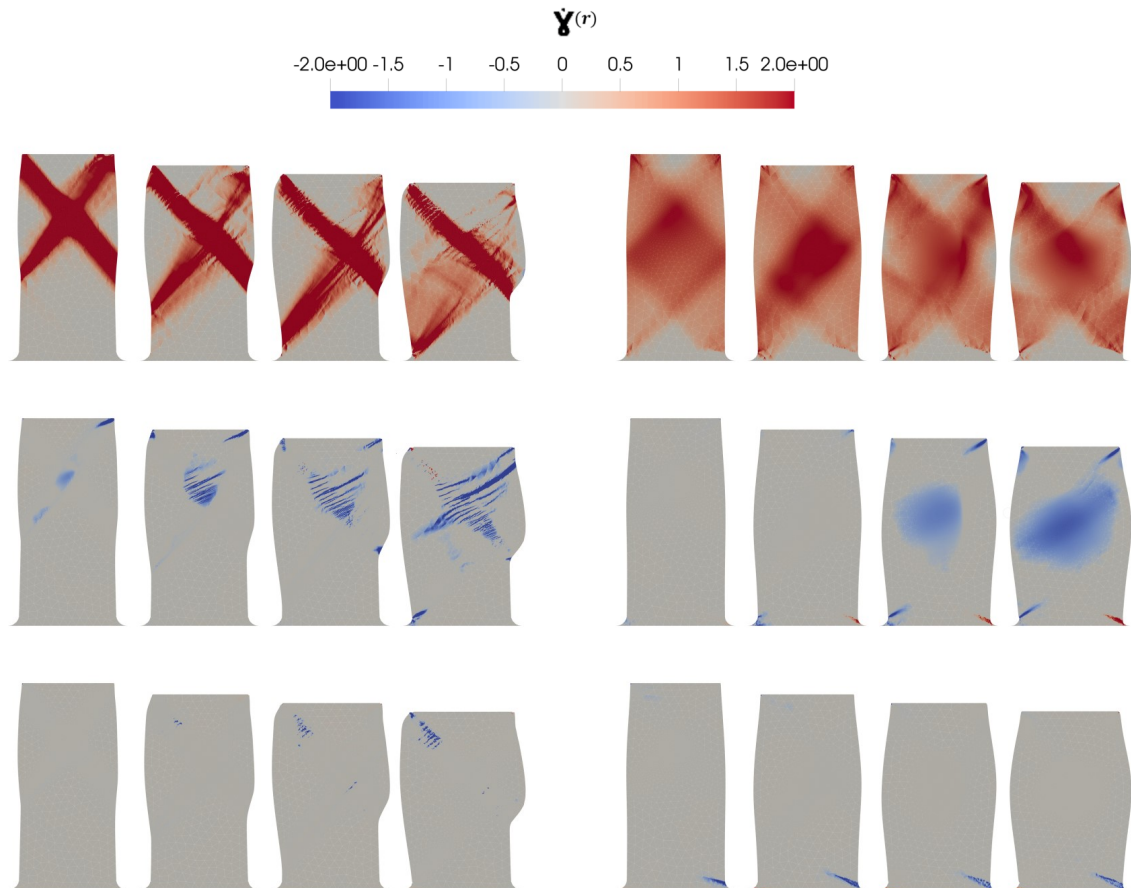**Slip rates.** Fig. 4.11 shows the spatial distribution of the slip rates correspond-

Figure 4.11: Pillar deformation for the self interaction model. The slip rates $\dot{\gamma}_1$ (up),$\dot{\gamma}_2$ (middle) and $\dot{\gamma}_3$ (bottom) distribution at different levels of deformations(5%, 10%, 14% and 18%) for two choices of initial dislocation densities: case (i) ($D = 1\mu$m) (left) and case (ii) ($D = 20\mu$m) (right).

Figure 4.12: Pillar deformation for the self interaction model. Dislocation densities ρ^1 (up), ρ^2 (middle) and ρ^3 (bottom) distributions at different levels of deformations (5%, 10%, 14% and 18%) for t two choices of initial dislocation densities: case (i) ($D = 1\mu$m) (left) and case (ii) ($D = 20\mu$m) (right).

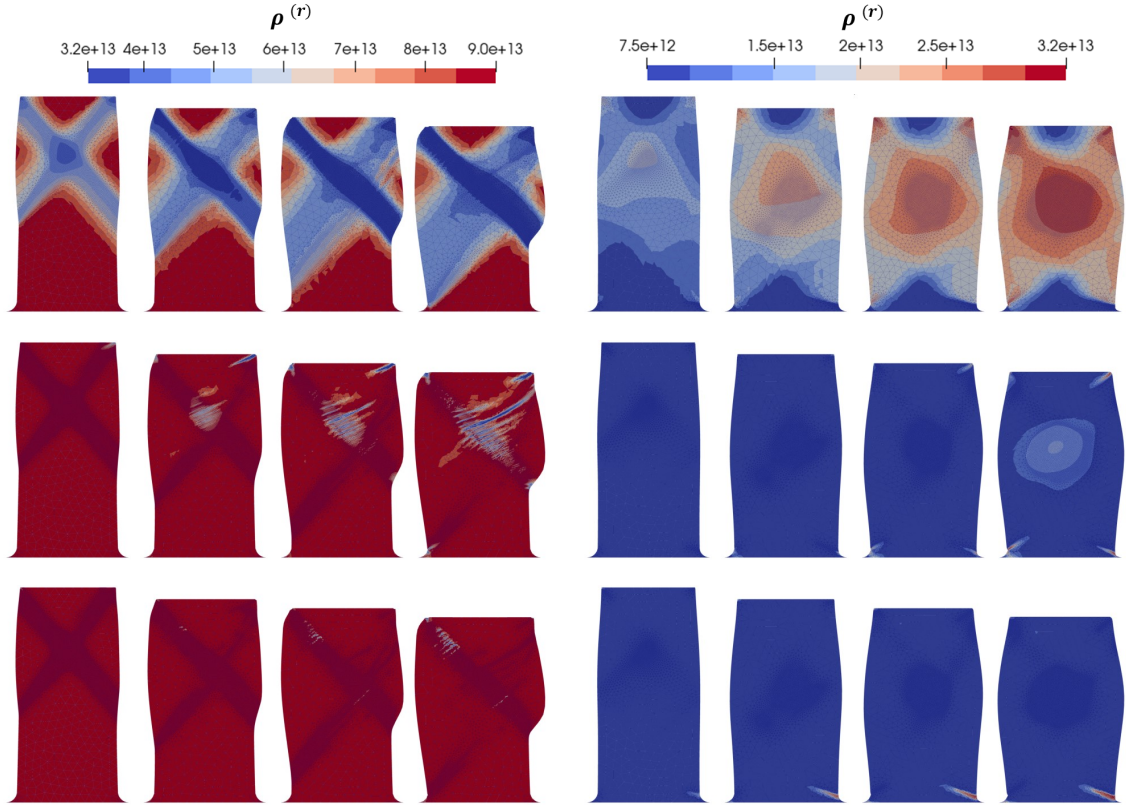ing to the 3 active slip systems at different levels of deformation in the micropillars. Slip system 1 remains active throughout the entire deformation process, irrespective the case considered. The activity of system 1 concentrates in the middle of case (ii) (larger specimen), while in case (i) (smaller sample), it localizes within the shear band. On the other hand, system 2 is active only for case (ii) (larger sample) and at higher deformation levels (beyond 10%). In the case (i) the activity of system 2 is somewhat limited and confined to a narrow bands, justifying its neglect. Notably, system 3 remained inactive across all cases.

Dislocation densities. Regarding the evolution of dislocation densities, illustrated in Fig. 4.12, for slip systems 2 and 3, which have small slip rates, we observe no significant variation. The dislocation density associated with slip system 1 decreases as deformation progresses in case (i) (small sample), while it increases in case (ii) (larger sample), as expected from the stability analysis.

Thus, in case (i) (smaller pillar), we observe a softening deformation process,

whereas in case (ii) (larger pillar), a hardening deformation process occurs.

The saturation of the computed dislocation densities starts at a high level of deformation and affects only system 1. This is evident for case (i) (small sample) at 12.5% of total deformation and for case (ii) (larger sample) at 18%. The delayed saturation of dislocation densities in case (ii) (larger sample) is attributed to the substantial difference in slip values, γ^1, between the two cases at an equivalent total deformation.

At 12.5% of total deformation, the mean slip value γ^1 was around 90% in the shear band for case (i), while for case (ii), it did not even reach 40%. These results confirm that saturation occurs for larger values of slip (more than 50%), as pointed out by the previous stability analysis.

Shear band. Altogether, this means that when dealing with softening processes (as in the case of small pillar size), plastic deformation tends to favor the propagation along a specific slip system, leading to one or two shear bands. When hardening is present (as in the case of larger pillars), shear bands cannot develop significantly, as the plastic yield limit increases with the slip accumulated in the shear band. This is why we observe a multitude of small shear bands, and "isotropization" is induced by the presence of multi-slips in different regions of the pillar, resulting in an overall homogeneous deformation.

Initial lattice orientation. The simulation results presented earlier are based on an initial crystal lattice orientation of $\theta^0 = 65°$, which serves as the reference configuration. Our goal is to investigate how the activity of slip systems evolves with different initial orientations. To explore the impact of the initial lattice orientation on localized plastic deformation (case (i)), we conducted additional simulations under the same conditions but with three distinct initial orientations: $\theta^0 = 35°$, $\theta^0 = 145°$, and $\theta^0 = 115°$.

For $\theta^0 = 35°$, as shown in Fig. 4.13 (a), the simulation reveals a multislip scenario, characterized by two localized shear bands instead of just one. Interestingly, these shear bands exhibit divergent orientations, appearing to point in opposite directions. Unlike the reference configuration, system 1 is no longer active, allowing systems 2 and 3 to accommodate the deformation.

Assuming that we initially rotate the crystal by $\frac{\pi}{2}$ from the reference configuration, no change in the deformation pattern is observed; deformation localizes exactly as it does in the reference configuration. This consistency persists even when the
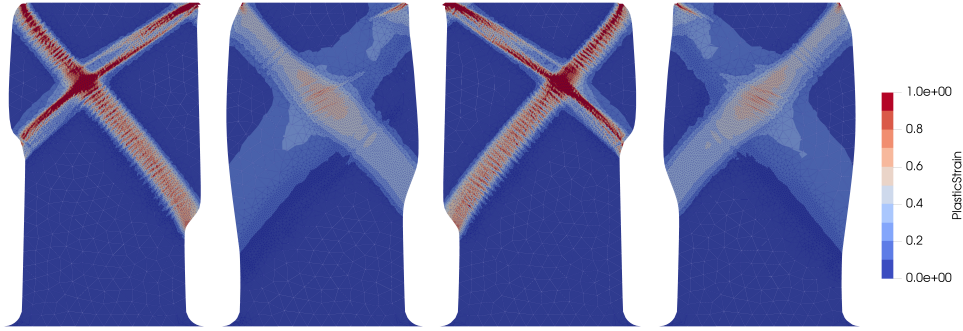
Figure 4.13: Pillar deformation for the self interaction model in case (i). The distribution of cumulated plastic strain at 11% of total deformation for different initial orientations of the crystal $\theta^0 =$: 35°; 65°; 145° and 115°.

reference configuration is set at an angle of 35°.

Alternatively, when the initial rotation angle is set as $\pi - \theta$, an intriguing shift in behavior is observed. The shearing direction is inverted relative to the shearing direction associated with the θ orientation, exhibiting mirror symmetry, as shown in Fig. 4.13. Irrespective of the specific initial angle θ^0 chosen, a consistent observation emerges: stable stationary shear bands form with an absolute angle between 45° and 55°.

4.3.3   Cross interaction computation

In this section, we explore the features captured by cross-interaction calculations and compare them to the results from self-interaction. We only consider the case (UC1) described previously and we remark that we observe similar results for the case (UC2).

(UC1) case

Notably, for the larger sample, the deformation process(i.e., the final shape) remains qualitatively unchanged, consistently exhibiting a hardening process characterized by diffusive overall deformation. However, a distinctive observation emerges in the case of the smaller sample ($D = 1\mu$m). Here, UC1 reveals aspects related to dislocation interactions between different systems that are not captured by the self-interaction model. The difference between UC1 and self-computation becomes evident in this context.

Compared to the softening process obtained from self-computation, the results imply that the smaller sample's deformation process follows a plateau, indicating a
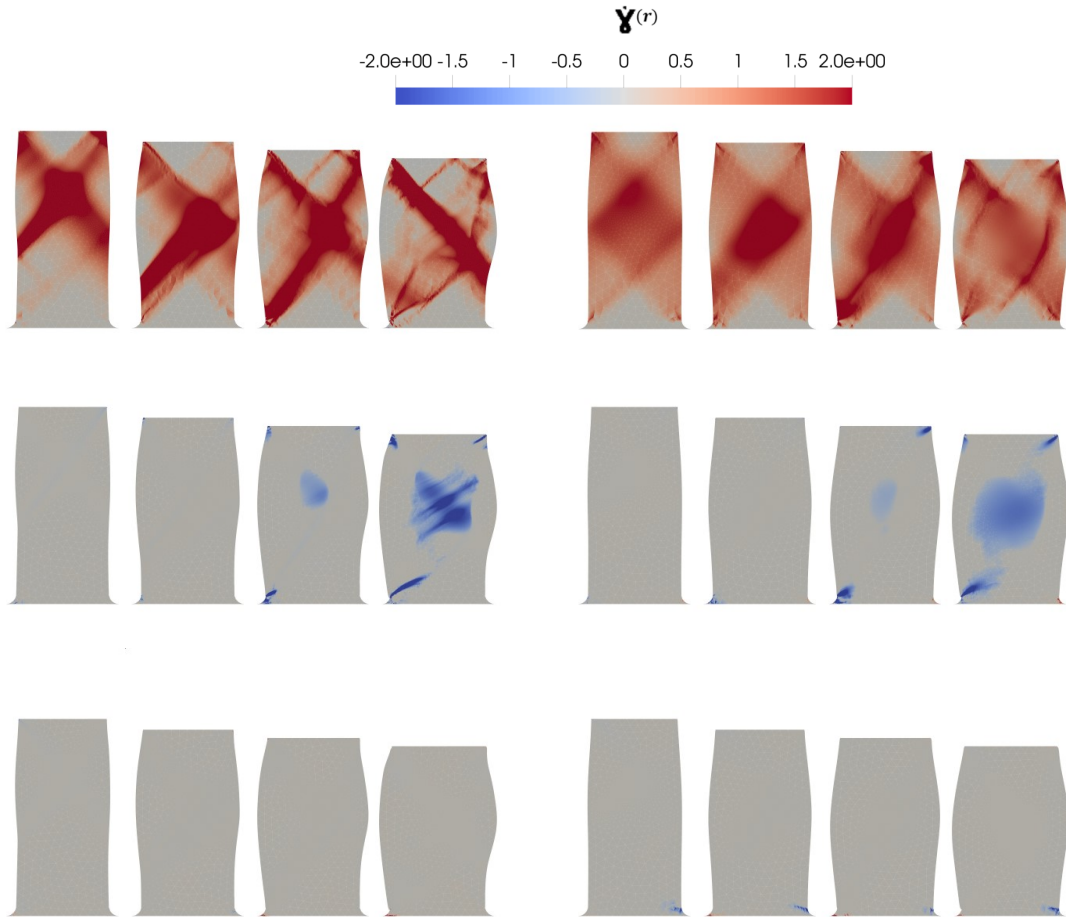
Figure 4.14: Simulation with the cross-interaction model (UC1). The slip rates $\dot{\gamma}_1$ (up),$\dot{\gamma}_2$ (middle) and $\dot{\gamma}_3$ (bottom) distribution at different levels of deformations(5%, 10%, 14% and 18%) for two sample diameters: 1 μm (left) and 20 μm (right).

shear yield strength between 37.75 and 38 MPa.

Examining Figure 4.14, which depicts the spatial slip rate distributions, we observe similarities between UC1 and self-interaction computations. In both samples, slip system 3 remains inactive during deformation, while slip system 1 consistently demonstrates activity.

Significantly, the activation of system 2, which occurs at a later deformation stage (greater than 14%), partly obstructs the activity of system 1, constituting an evident divergence between UC1 and self-interaction computations. In the UC1 computation, the slip motion orientation is no longer dictated by system 1, in contrast to the self-interaction model. Instead, the slip direction is influenced by both system 1 and system 2, with a bias towards system 1.

Finally, turning our attention to the spatial distributions of dislocation densities in the UC1 computation, shown in Fig. 4.15, none of the larger specimen systems

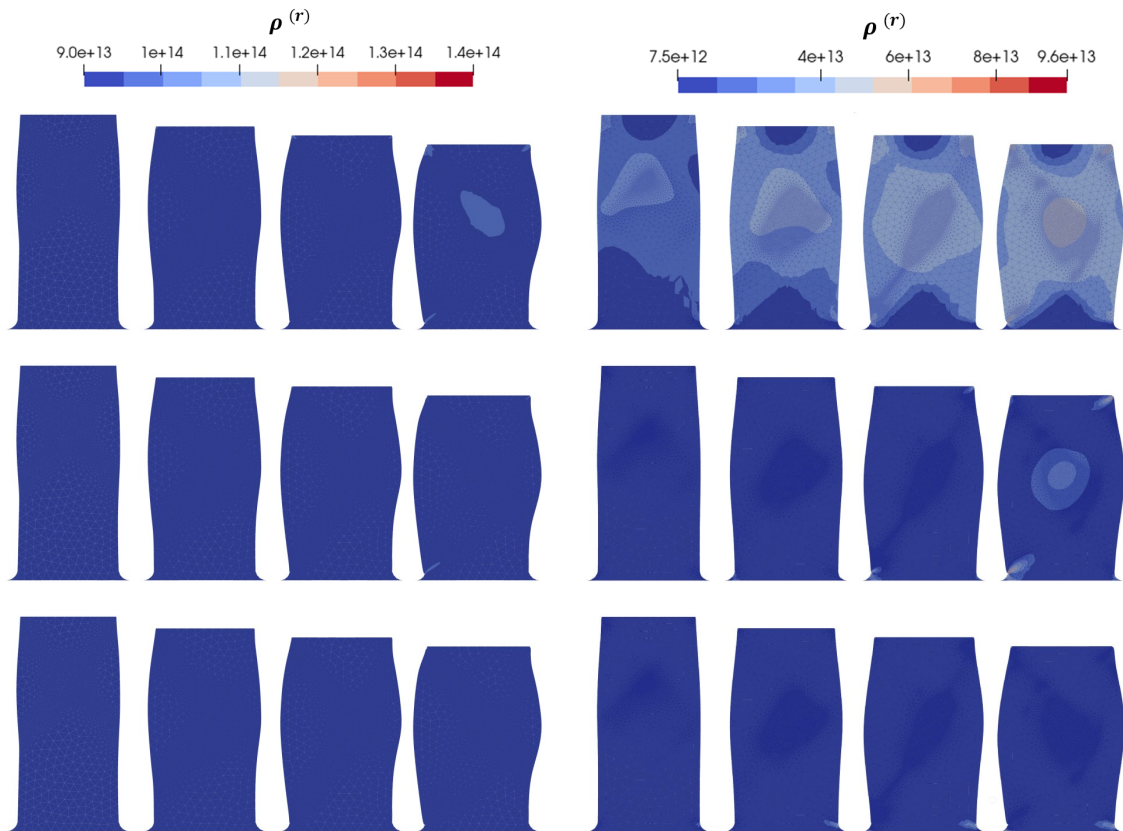Figure 4.15: Simulation with the cross-interaction model (UC1). Dislocation densities ρ^1 (up), ρ^2 (middle) and ρ^3 (bottom) distributions at different levels of deformations (5%, 10%, 14% and 18%) for two sample diameters: $1\mu m$ (left) and $20\mu m$ (right).
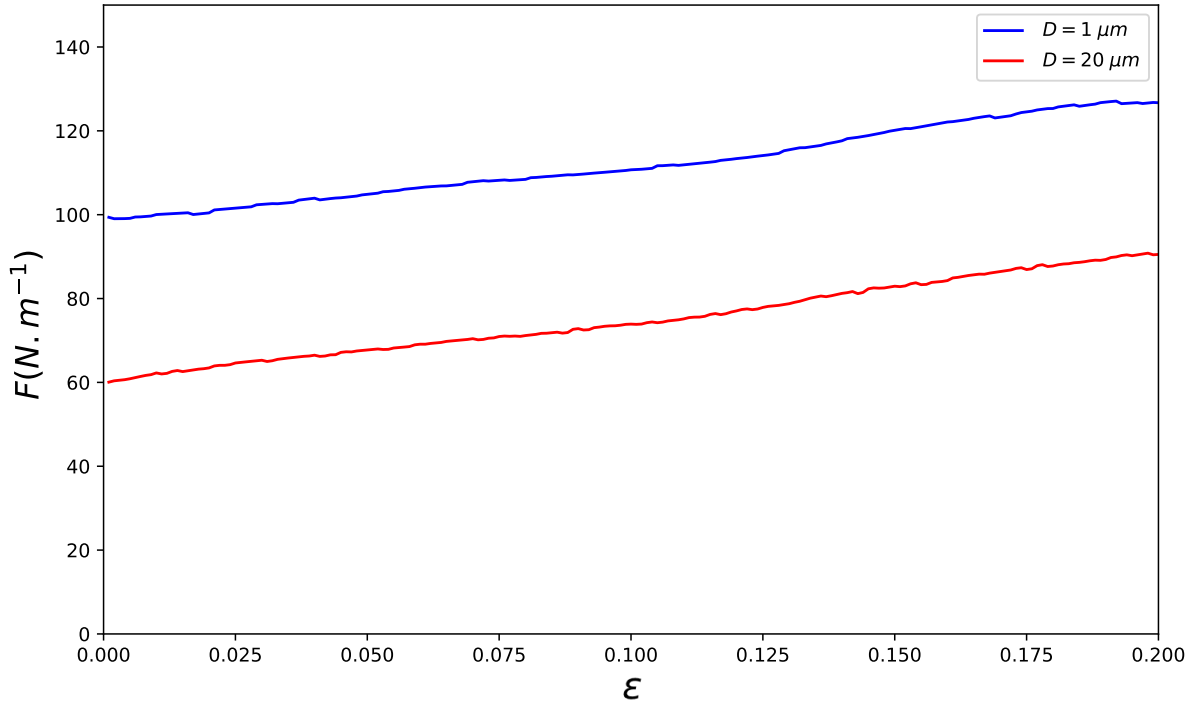
Figure 4.16: Pillar deformation for the cross interaction model(UC1). Linear Force vs plastic Strain : case (i) ($D = 1\mu$m) (Blue) and case (ii) ($D = 20\mu$m) (Red).

reach the uniform dislocation density saturation value. However, in the sample with a diameter of ($D = 1\mu$m), saturation occurs for both systems, namely system 1 and system 2. This can be attributed to the fact that the saturation value is three times higher than its self-interaction counterpart.

Regarding the load evolution in cross interaction computation (UC1) depicted in Fig.4.16, there are no new findings compared to the self-interaction computation for the larger sample previously discussed. However for smaller sample the less localization compared to the self interaction is reflected in an increase in load as plastic deformation progresses.

4.4   Conclusions

Dislocation-density based crystal plasticity models are introduced to account for the microstructral changes throughout the deformation process, enabling more quantitative predictions of the deformation process compared to slip-system resistance-based plasticity models. In this work, we presented a stability analysis of some established dislocation density-based models, including the Kocks and Mecking (KM) model and

its variants, aiming to identify conditions for stationary states in active slip systems and evaluate their linear stability. Our analysis can be generalized to any type of dislocation density model, providing a broader framework for understanding the stability of such systems. Interestingly, we uncover size-dependent effects manifesting through initial dislocation density variations, particularly in FIB-prepared samples, influencing the material's softening or hardening responses. Finally, we conducted numerical simulations of micro-pillar compression using an Eulerian crystal plasticity approach to address the behavior of materials at micro-scale dimensions. Our findings indicate that microstructural evolution in small-scale materials can be effectively modeled using dislocation-density based CP models, providing valuable insights for the design of miniaturized mechanical devices and advanced materials in the rapidly evolving field of nanotechnology.

Chapter 5

Intragranular void evolution in crystals

5.1 Introduction

The mechanisms of void growth and coalescence are key contributors to the ductile failure of crystalline materials, occurring through plastic flow around pre-existing voids or nucleated cavities at second-phase particles. These cavities can emerge on two distinct scales within polycrystalline material: at the grain scale (i.e., intragranular and intergranular porosities) and at the polycrystalline scale. The progression of void growth is highly dependent on the nature of the surrounding plastic deformation, which can be modeled through (i) crystal plasticity at the grain scale and (ii) isotropic or texture-induced anisotropic plasticity at the polycrystal scale. Thus, micromechanical modeling of void growth and coalescence must account for these varying local behaviors to adequately capture the influence of porosity on the overall macroscopic response. However, it is generally infeasible to derive comprehensive analytical models for the plasticity of ductile porous solids due to the involved complexity.

The aim of this chapter is to carry out an analysis of large defomation voids growth in single crystals (HCP, FCC) using an Eulerian crystal plasticity finite element simulations. This analysis is driven by previous work on the analytical homogenization of porous single crystals with internal cavities, as demonstrated in several models that address void growth [46, 99, 98, 86, 76, 118, 119, 65]. In particular, it extends the work of Paux et al. (2022), who contribute to the understanding of ductile failure in crystalline materials by addressing the anisotropic plastic be-

havior of single crystals using an innovative approach that involved a new class of piecewise constant velocity fields derived from FFT numerical analysis, which effectively improved the estimation of macroscopic yield stress, particularly in models with periodic void distributions in single crystals.

While the model proposed in [98] provides a robust framework for estimating yield criteria, it lacks the capability to predict the evolution of void shapes during deformation, a crucial factor in understanding the long-term behavior of materials under stress. To address this shortcoming, the present chapter makes use of an Eulerian numerical model that not only captures the onset of yielding but also accurately predicts the evolution of void shapes. We seek to extend the contributions of [98], offering a more comprehensive tool for analyzing ductile failure in crystalline materials. The model is applied to the well-known experimental study by [22], which observed that voids in an HCP crystal evolves into a polyhedral cavity, a prediction also made in the same study. In that work, void growth was successfully modeled using a finite element approach that incorporated elastic-plastic behavior and kinematic hardening, with growth rates associated with prismatic slip activation. In this context, the Eulerian rigid (visco) plastic proposed model offers an alternative or complementary approach for analyzing void evolution.

To further explore these mechanisms, we will use unit cell FEM computations, which have been proven effective for analyzing void-level processes across different geometries [55, 58, 120, 139], offering insights at a relatively low computational cost.

In the next two sections, the proposed model is evaluated under two distinct plane strain configurations involving intergranular porous crystals : (1) Growth evolution under radial loading (hydrostatic tension) applied on a hexagonal close-packed (HCP) crystal discussed in Section 2.7.2 and (2) Growth evolution under uniaxial loading (Tensile test) on a face-centered cubic (FCC) crystal, detailed in Section 2.7.1. These cases are chosen to illustrate the model's capability in different crystallographic structures and loading conditions, thereby demonstrating its broader applicability.

5.2   Void growth evolution under radial loading

In the present section, we present the numerical setting, including geometrical and material characteristics, initial and boundary conditions, followed by the results and
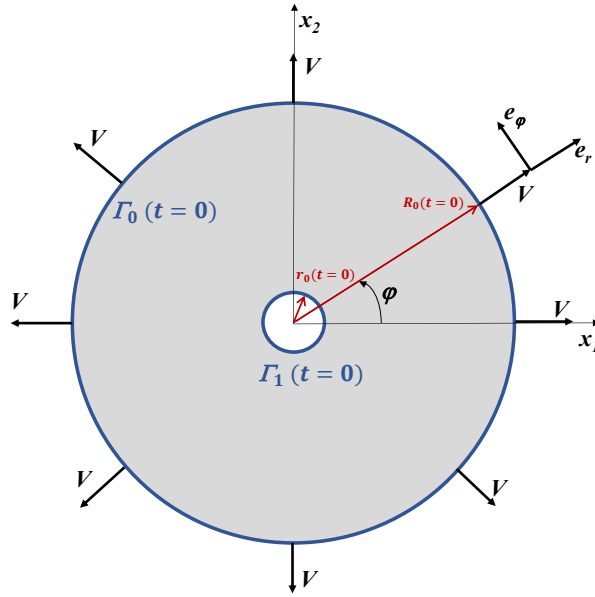
Figure 5.1: Schematic representation of a porous single-crystal disc unit cell with a single circular void at its center.

discussion of the 2D void growth simulations under plane strain in an HCP single crystal (see Section 2.7.2).

Fig. 5.1 shows the initial state of the one-void unit cell represented by a disc of radius R_0, containing an initially circular void at its center with a radius $r_0 = R_0/30$. This configuration results in an initial void fraction of $f_0 = \left(\dfrac{r_0}{R_0}\right)^2 = 0.111\%$.

On the external boundary, denoted by $\Gamma_0(t)$, we impose an expansion velocity V_0, corresponding to the in-compressible Eulerian velocity field $\boldsymbol{v}^* = \dfrac{V_0 R_0}{r}\boldsymbol{e}_r$, i.e.

$$\mathbf{V}(t)(x,y) = \frac{V_0 R_0}{x^2 + y^2}(x\boldsymbol{e}_1 + y\boldsymbol{e}_2), \quad \text{for } (x,y) \in \Gamma_0(t), \tag{5.1}$$

while the internal boundary, denoted by $\Gamma_1(t)$, is traction free (i.e. $\mathbf{S}(t) = 0$). The initial conditions in velocity and in the crystal orientation where chosen to be

$$\boldsymbol{v}^0(x,y) = \frac{V_0 R_0}{x^2 + y^2}(x\boldsymbol{e}_1 + y\boldsymbol{e}_2), \quad \theta^0(x,y) = \theta_0 \tag{5.2}$$

The expansion velocity V_0 was chosen to be small such that the process is expected to be quasi-static. By integration on the Eulerian coordinate r gives the external radius can be deduced to be $R^2(t) = R_0^2 + 2V_0 R_0 t$, which means that the engineering area deformation is given by

$$\epsilon^{eng}(t) = \frac{R(t)^2 - R_0^2}{R_0^2} = \frac{2V_0 t}{R_0}.$$

The time interval $[0, T]$, the velocity V_0 and the rayon R_0 where chosen such that the final engineering volume/area deformation is $\epsilon_{final}^{eng} = 1.32\%$. Note that even the final ϵ_{final}^{eng} is small the strains around the cavity are expected to be much larger. Based on the above formula of engineering area deformation we estimate it to be of order of $\epsilon_{final}^{eng} R_0 / r_0 = 30\epsilon_{final}^{eng} \approx 40\%$. The material parameter used in this quasi-static computation is not directly specific to a particular material but reflects the order of magnitude typically associated with hexagonal close-packed (HCP) crystals. The material parameters are: density $\rho = 3200\text{kg/m}^3$, slip resistance $\tau_c = 20\text{MPa}$ for all systems with no hardening, and a viscosity, η chosen for numerical reasons to be as small as possible (of order of 1% of $\tau_c R_0 / V_0$).

In the following subsections, we examine the evolution of slip bands around the cavity, from their initiation to large deformations under hydrostatic tension loading as predicted by the proposed model. Given the distinct phases observed in the deformation fields, the analysis is divided into two stages, each discussed in a separate subsection. The first stage focuses on small deformations, analyzing the onset of shear and kink bands and comparing the findings with existing models from the literature. The second stage explores the large deformation regime, following the evolution of the deformation patterns, described in the onset phase.

5.2.1   Onset of the shear/kink band deformation

At low deformation levels, although the size and morphology of the void show minor variations, slip lines are present, allowing for their characteristics to be analyzed. In Figure 5.2, we present a qualitative comparison of the equivalent von Mises strain distribution in a periodic hexagonal unit cell with aligned crystal orientation $\theta = 0°$, computed using the FFT method described in [98] with the deformation rate predicted by the current model. This comparison is particularly valid at low deformation levels where the two models are valid and where the difference between deformation and deformation rate is negligible. Despite the difference in cell microstructure, hexagonal in [98] and disk-shaped in the current model, this comparison remains justified at equivalent low porosity levels (0.111% and 0.24%, respectively), where edge effects are minimal and do not significantly impact the results around the cavity. All results are presented with an enlarged view around the void of the circular cell to clearly visualize the different fields. The zoomed region is shown as a rectangular area, with dimensions set to $26r_0$ in width and $19r_0$ in height, centered

on the void, where r_0 is the initial radius of the void.

At the onset of strain localization, a fractal network emerges as observed in strain spatial distribution and the strain rate, a (redundant) base pattern of twenty four slip lines, composed of two superimposed six-pointed stars with a 45-degree phase shift between them, recursively repeated with self-similarity from the exterior of the cell up to the void, forming successive layers.

The base pattern is made up of two types of lines: lines parallel to slip directions, known as classical slip bands, and lines parallel to the slip plane normals, referred to as kink bands.

A shear band is defined as a region characterized by high plastic strain and low crystallographic reorientation, with predominantly one slip system active, where the slip direction is parallel to the band. In contrast, a kink band is a region with high plastic strain and sharp crystallographic reorientation, also dominated by one slip system, but with the Burgers vector perpendicular to the band direction[134].

The consistent appearance of this twenty-four-slip-line pattern both models suggests that it is an intrinsic feature of the strain field in porous single crystals. Notably, there is a clear agreement between the two models in their description of the initiation of shear and kink bands.
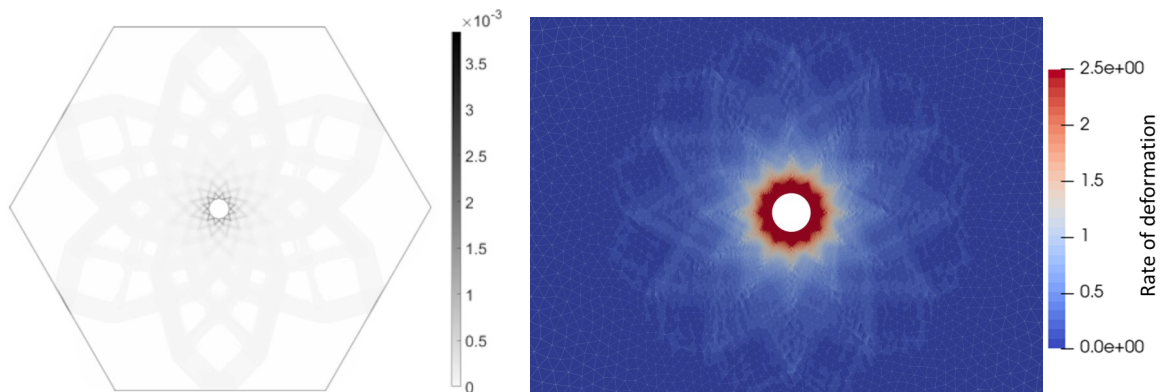
Figure 5.2: Onset of the deformation: qualitative comparison using two different approaches. Left: equivalent strain obtained under small strain hypothesis, as reported in [98]. Right: zoom of the equivalent strain rate at a low deformation level ($\epsilon_{vol}^{eng} = 0.0033\%$) obtained with the Eulerian model.

In this context of incipient plasticity, the three prismatic slip systems demonstrate equivalent amounts of glide, as shown in Fig. 5.3 (Top), with all slip systems being simultaneously active. Each opposite facet of the hexagonal cross-section is governed by the activity of a specific slip system; for example, the two horizontal

Figure 5.3: Onset of the deformation. The three slip systems of HCP crystal based on finite element simulation results : (left) $s = 1$, (middle) $s = 2$, and (right) $s = 3$. Top: slip deformation rates computed with the presented Eulerian model. Bottom: slips deformation computed with a strain gradient crystal plasticity model without hardening from [12].
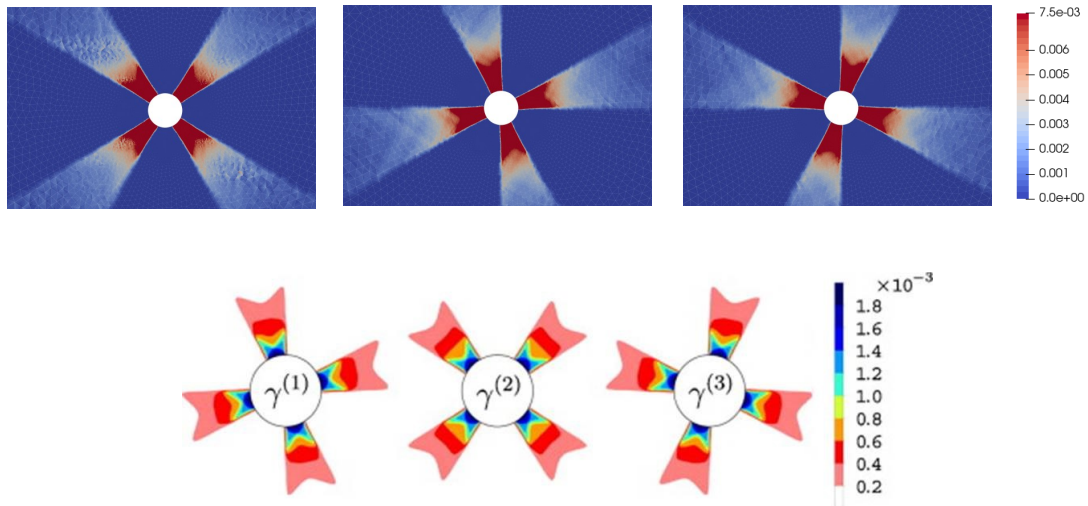
facets are controlled by the first slip system. This simultaneous slip activity contrasts with the findings of [22], where slip systems are activated in pairs. This difference in the current analysis likely results from the assumption of equal slip resistance across all systems and the absence of hardening on an active slip system that could induce its deactivation and the activation of another slip system. A similar finding as in the present model is reported by [12] (see Figure 5.3 bottom), where it is noted that slip contours are periodic with a period of 90°. Specifically, slip system one is predominantly active in the region $0 \leq \theta \leq 30°$, slip system two in $30 \leq \theta \leq 60°$, and slip system three in $60 \leq \theta \leq 90°$ of the upper right quadrant.

Having explored the initiation and early evolution of shear and kink bands at small deformation levels and seen an agreement between the present model and the model of Paux et. al. [98], we now shift our focus to the large deformation regime. In this stage, the behavior of the slip bands undergoes significant changes as deformation progresses, with noticeable effects on the microstructure and deformation patterns. The following section, using the model's response, examines how these patterns evolve under increasing strain, highlighting the transformation of slip lines and the eventual disappearance of shear bands and/or kink bands.

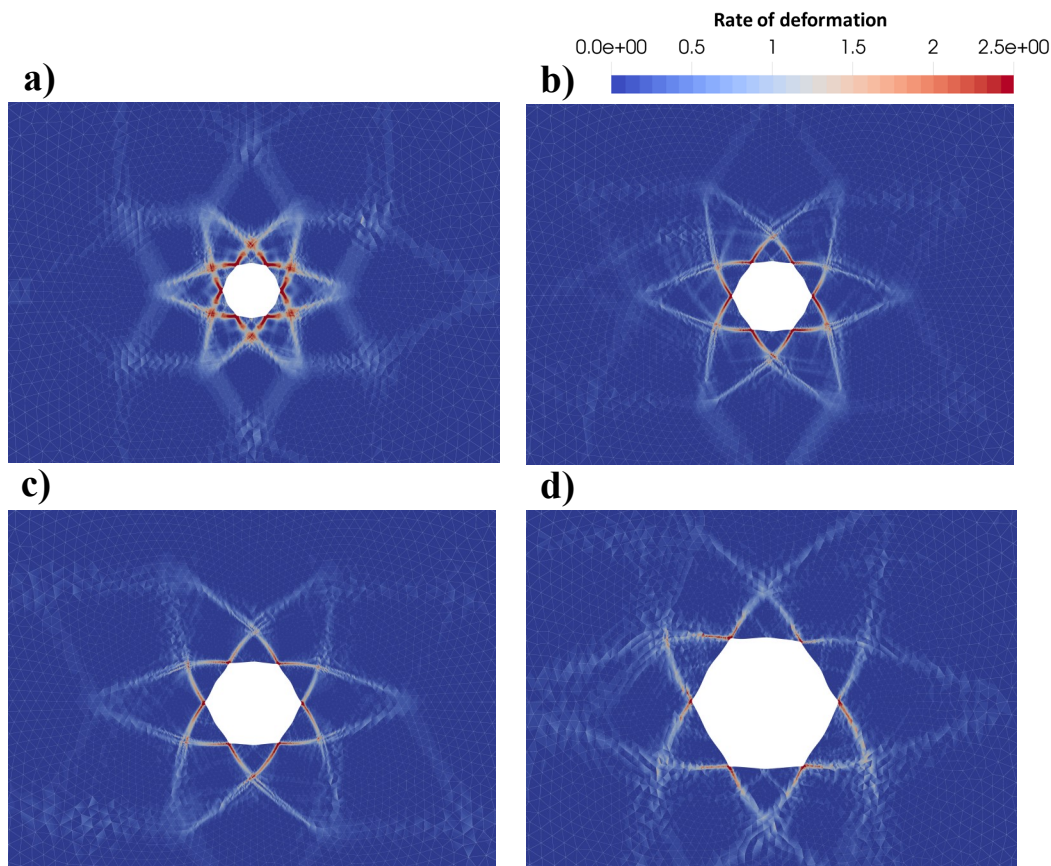## 5.2.2   Large deformations towards a hexagonal shape

Figure 5.4: Evolution of equivalent deformation strain rate and void morphology at different stages of the deformation: $\epsilon^{eng} = 0.2475\%$, $\epsilon^{eng} = 0.66\%$, $\epsilon^{eng} = 0.99\%$ and $\epsilon^{eng} = 1.32\%$.

Figure 5.4 illustrates the evolution of the deformation rate field within the cell and the corresponding changes in void shape at large local deformation for various intervals. As deformation progresses, the monocrystal shape loses its anisotropy, more slip bands appears, while the kink bands progressively lose activity and disappear. The persistent activity of the shear bands at elevated local deformation levels drives the transformation of the initially circular void into a hexagonal shape, with its facets aligning along the slip directions. As deformation advances further, as shown from (c) to (d) in Figure 5.4, the hexagonal void undergoes a relatively uniform expansion, with the shear band activity becoming less intense compared to the period between (a) and (b), allowing for greater morphological stability.

The final state corresponding to the deformation rate contour derived from Figure 5.4 (d) is again presented in Figure 5.5 (a), where we compare the final void
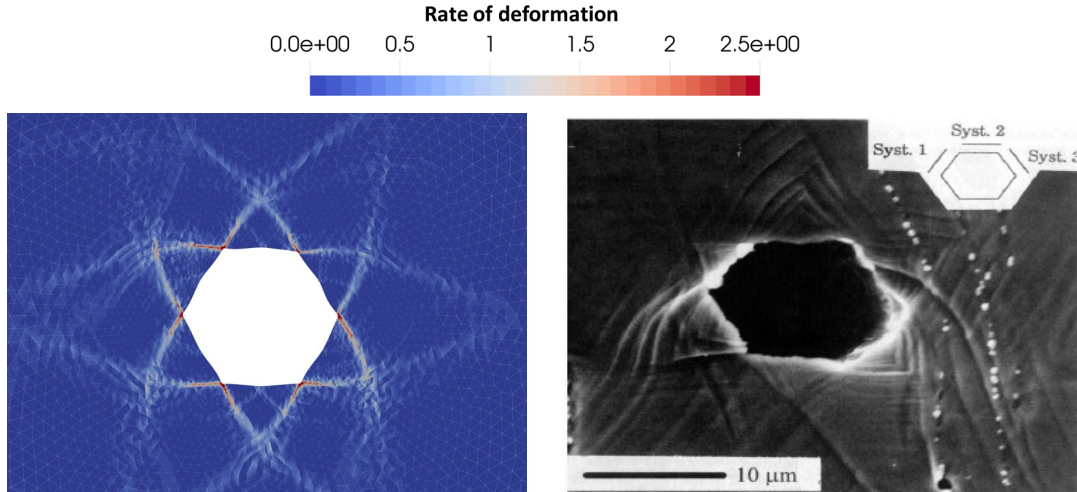
Figure 5.5: Qualitative comparison between the current model finite element computations and the experimental observations. (Left) Void morphology at $\epsilon^{eng} = 0.66\%$. (Right) SEM image of the hexagonal cross-section of the cavity observed on the sample surface, showing the three prismatic slip systems (1, 2, 3) as identified in [22].

shape from finite element simulation results (deformation rate) with experimental observations (accumulated plastic strain) reported by [22]. From a morphological perspective, both images exhibit a similar appearance of the void, with the exception of the slip traces that are present only in the experimental results. It is important to note that, according to [22], the slip traces observed in Figure 5.5 (b), which correspond to the accumulated plastic strain, are attributed to the imperfect orthogonality of the <c> axis with respect to the sample surface.

Although both the experimental and numerical model consider an HCP crystal with three prismatic systems, it is important to recognize that the loading conditions affecting the void may not be identical. The experimental method employs polycrystal specimens, making it challenging to determine the exact loading conditions applied in the vicinity of the void and complicate the direct comparaison between the simulation and experiment. Nonetheless, numerical simulations show a strong overall correlation with the experimental results, this validation is further reinforced by previous comparisons made at small deformation levels, where our model was assessed against Fast Fourier Transform (FFT) computations and finite element (FE) simulations. The consistency across these different methods highlights the model's reliability and its capacity to accurately predict material behavior under varying deformation conditions.

As noted earlier, at large deformations, the slip lines evolve into shear bands,

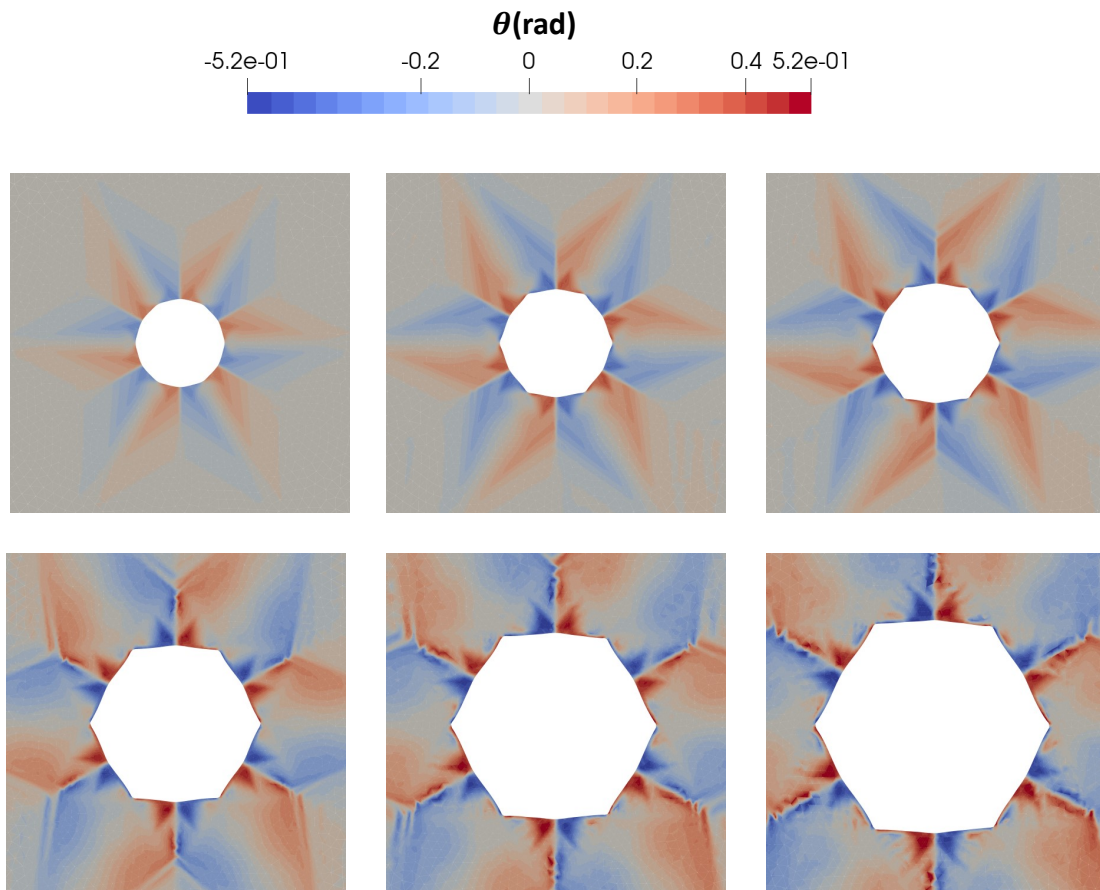Figure 5.6: Variations in circular cell microstructure orientation θ (expressed in radians) during hydrostatic tension loading in the basal plane of an HCP crystal, with the initial crystal orientation set to $\theta = 0°$ at : (a) $\epsilon^{eng} = 0.125\%$, (b) $\epsilon^{eng} = 0,2475\%$, (c) $\epsilon^{eng} = 0.33\%$ and (d) $\epsilon^{eng} = 0.66\%$. The color scale of the contour plot is customized.

while the kink bands, which are present at smaller deformations, cease to exist. Since kink bands play a key role in lattice rotation mechanisms, this transition prompts an investigation into how crystal orientation is affected. Figure 5.6 shows that, in regions far from the void, the crystal orientation remains unchanged (close to 0 degrees). However, near the void, the orientation distribution formed a star-like pattern with six identical branches, matching the six-star pattern associated with kink bands, which is expected. Within each branch, the orientation varies from $-10°$ to $10°$, with one half of the branch rotating positively and the other half negatively (see Chapter 2 for more details and explications related to the orientation attractors). This bidirectional rotation creates a repulsive effect that contributes to the kink bands fading and to the formation of the corners defining the angles of the hexagon, where the majority of the accumulated plastic strain and slip activity are concentrated. In these corner regions, the mono-crystal experiences a minimal rotation.

As we move closer to the cavity, the highest rotation level of $30°$ degrees appears at the center of each edge of the hexagon, represented by a small half branch motif mirrored on the opposite side. One half branch shows negative rotation, while the other exhibits positive rotation. The disappearance of kink bands at high deformation levels implies that the orientation contour plot shows no significant differences between small and large deformations. The only notable change is the emergence of a second star-like pattern at the final simulation stage, slightly farther from the first, indicating a continued propagation.

5.3   Void growth evolution under uniaxial loading

For FCC crystal under uniaxial loading, the one-void domain is represented by a rectangular section with $H_0 = 2L_0$, containing an initially circular void at the center of radius $r_0 = \frac{L_0}{30}$ (see Figure 5.7). This configuration results in an initial void fraction of $f_0 = \dfrac{\pi r_0^2}{H_0 L_0} = 0.1745\%$.

The pillars top is animated with a vertical velocity $\boldsymbol{V} = V\boldsymbol{e}_2$ (small enough to deal with a quasi-static loading), while the bottom part is kept fixed $\boldsymbol{V} = 0$. The lateral boundary $\Gamma_c(t)$ is stress free ($\boldsymbol{S} = 0$). The FCC single crystal has initially the orientation θ_0, i.e.
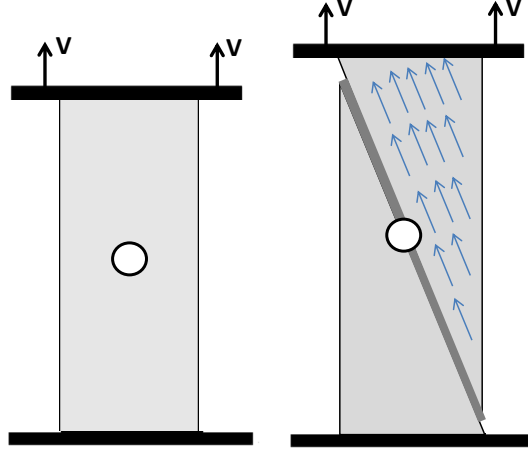
$$\theta(0, x, y) = \theta_0,$$

Figure 5.7: Schematic diagram of a tensile test. The micropillar specimen is a rectangular bar with a circular void at the center, subjected to tensile forces applied at the top, causing elongation. A diagonal shear band forms, indicating localized plastic deformation under the tensile loading conditions.

with three choices of $\theta_0 \in \{0°, \frac{\phi}{2} = \frac{54.7°}{2}, 65°\}$ which we help us to gain an understanding of the role played by the angle between the loading axis and the crystal lattice.

The engineering strain is given by

$$\epsilon^{eng}(t) = \frac{H(t) - H_0}{H_0},$$

where $H(t)$ is the current height of the pillar. The material parameters used for this simulation are : density $\rho^{mass} = 16650 kg/m^3$, slip resistance for all systems equal to $\tau_c = 220$ MPa with no hardening, and a viscosity, η chosen, for numerical reasons, to be as small as possible to assure that the system is rate-independent (around 1% of $\tau_c H_0/V$). The upper velocity V and the time interval $[0, T]$ where chosen such that the final engineering strain is $\epsilon^{eng}_{final} = 15\%$.

In this test, the top surface of the specimen remains fixed horizontally, ensuring that both the top and bottom surfaces stay parallel and retain the same horizontal coordinates at their extremities, despite significant deformation. The analysis focuses on how shear and kink bands influence the evolution of the void, which is affected by the initial crystallographic orientation of the micropillar.

In this study, we analyzed three cases that represent three different initial crys-

Figure 5.8: Accumulated plastic strain evolution of a FCC porous micropillar under tensile loading with three initial crystallographic orientations $\theta_0 = 0°$ (up), $\theta_0 = \dfrac{54.7°}{2}$ (middle) and $\theta_0 = 65°$(bottom) at four levels of engineering strains $\epsilon^{eng} = 0, 0.05, 0.1$ and $\epsilon^{eng} = 0.15$.
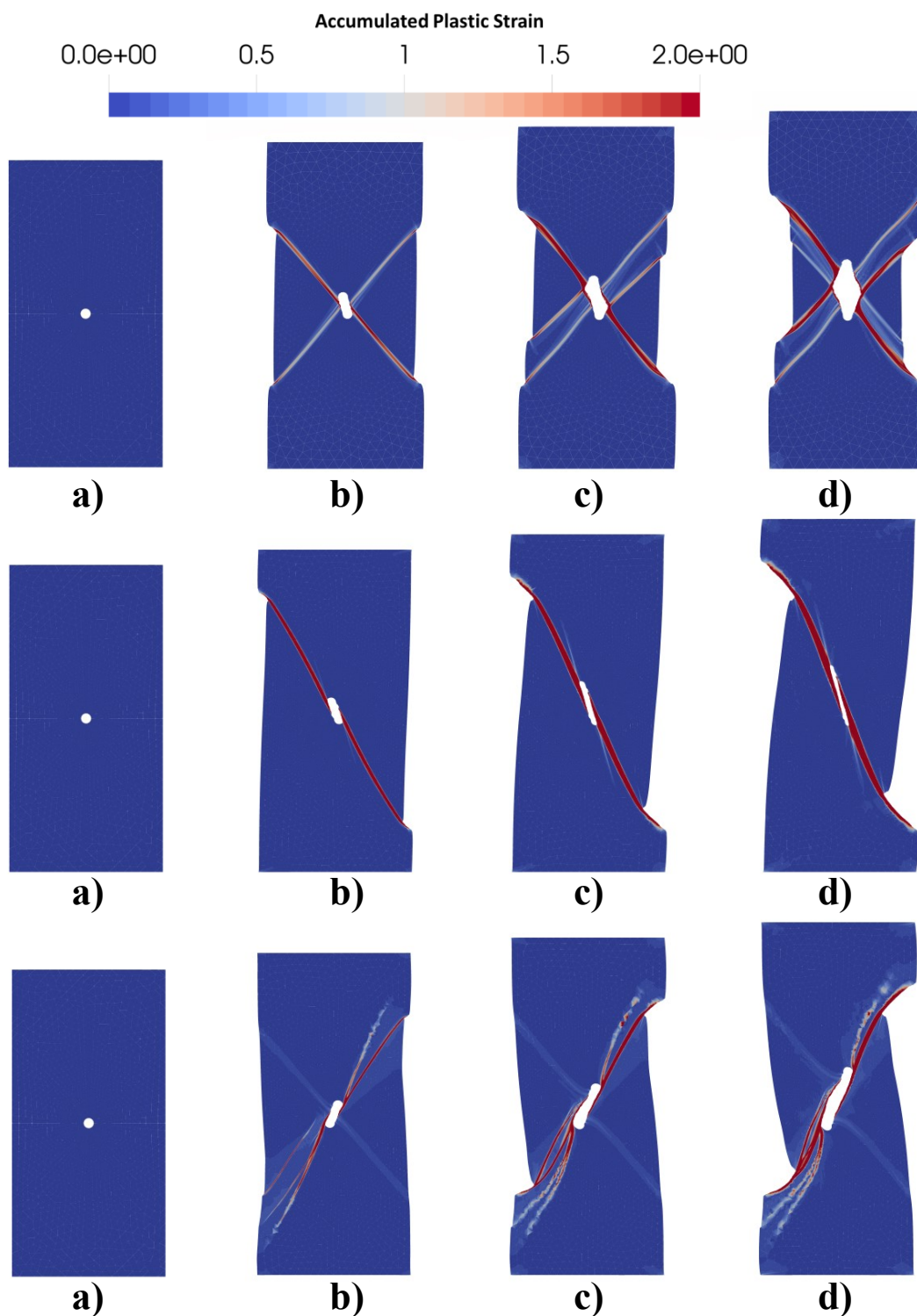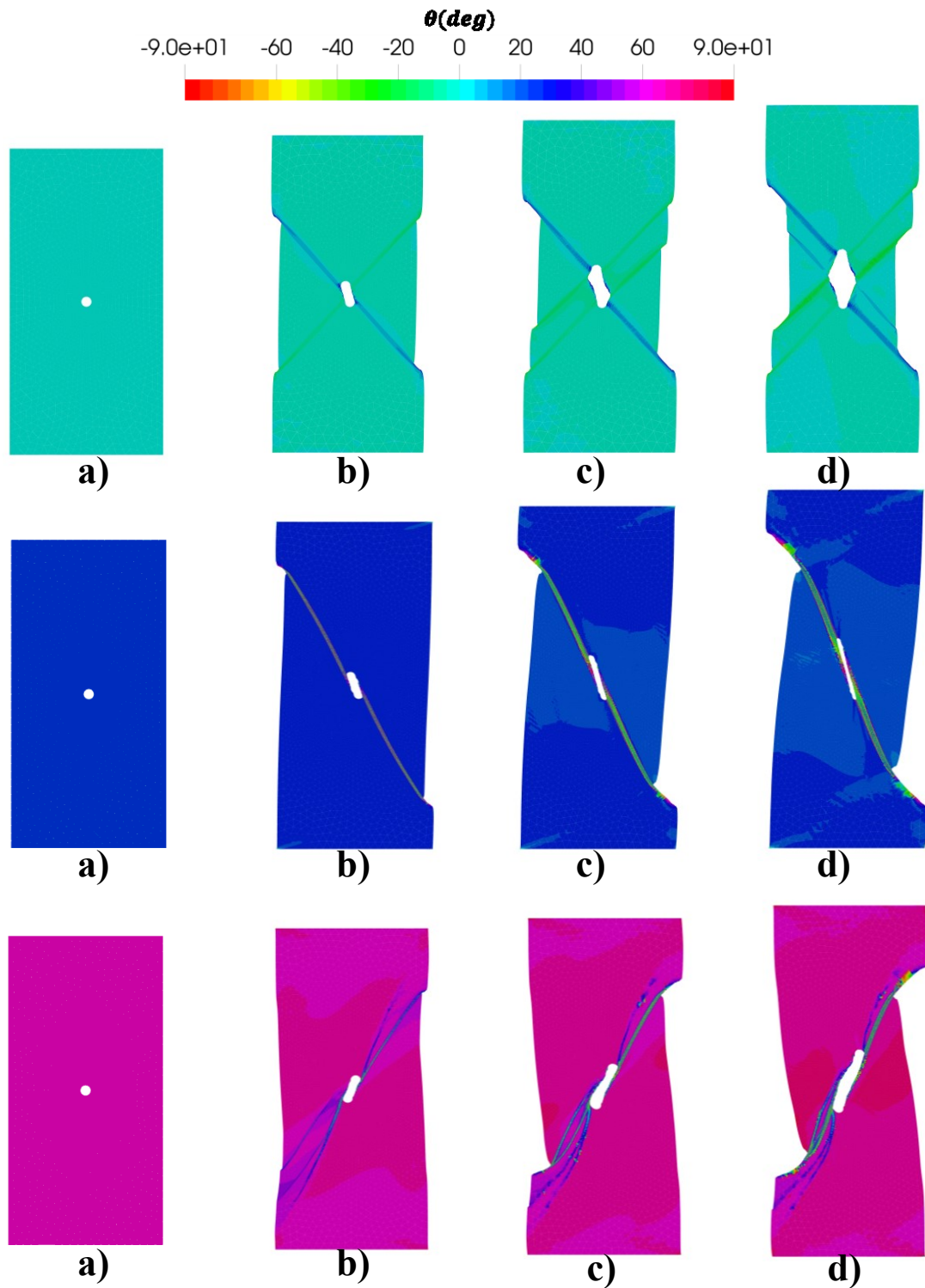
Figure 5.9: Lattice orientation evolution of a FCC porous micropillar under tensile loading with three initial crystallographic orientations $\theta_0 = 0°$ (up), $\theta_0 = \dfrac{54.7°}{2}$ (middle) and $\theta_0 = 65°$ (bottom) at four levels of engineering strains $\epsilon^{engn} = 0, 0.05, 0.1$ and $\epsilon^{engn} = 0.15$.

tallographic orientation of the micropillar :

- The first case corresponds to an orientation of $\theta_0 = 0°$, aligning with one of the three initial slip systems, namely the slip system 1.

- The second case involves an orientation of $\theta_0 = \frac{54.7°}{2}$, which lies between two slip systems, one at $0°$ and the other at $\theta_0 = 54.7°$.

- The third case considers an orientation of $\theta_0 = 65°$.

Figure 5.8, which illustrates the evolution of a central void in an FCC micropillar during tensile testing, plots the accumulated equivalent strain in the three cases. A general remark is that the deformation is very localized in the shear bands where we deal with more than 200% while the global strain is less than 15%.

Initial observations show that all voids are distorted under localized, but depending on the crystallographic orientation void either tend to collapse or to grows. While crystallographic orientation is crucial in determining this behavior, stress triaxiality also plays a significant role. As noted in [42], void deformation behavior varies considerably with stress triaxiality : at high triaxialities, voids tend to grow and coalesce, while at lower triaxialities, distortion, localized shearing, and collapse are more prevalent. Although the effect of stress triaxiality is not analyzed in detail here, it is important to note that the low triaxiality in the uniaxial tensile test favors void distortion, collapse, or closure. This is also reflected in our simulation of the radial growth case discussed earlier, where higher triaxiality leads to void growth rather than collapse.

Continuing from Fig. 5.8, the scenario of void collapse is seen in the middle panel of the figure, which correspond to an initial angle of $\theta_0 = \frac{54.7°}{2}$. Due to the single localized shearing, the circular void progressively flattens and becomes more elliptical with continued plastic deformation, eventually forming a highly elongated ellipse with a significantly reduced height (high eccentricity).

In contrast to the flattening behavior, void growth in this simulation occurs through double localized shearing. The presence of two orthogonal slip bands stretches the void along two directions, preventing one dimension from becoming disproportionately small relative to the other. The double shearing observed at $\theta_0 = 0°$ and $\theta_0 = 65°$, but in different manners:

- At $\theta_0 = 0°$, Fig. 5.8 (Top), double shearing initially appears as alternating

shear activity between two slip bands, which eventually progresses to simulta-
neous slip band activity in the final stage of deformation.

- At $\theta_0 = 65°$, Fig. 5.8 (bottom), the dominant band is active at the bottom of
  the left side and the top of the right side of cavity, while the second band is
  only active at the bottom of the left side of cavity.

With this general overview description of the potential void deformation scenarios
under uniaxial tension based on initial orientation, we will now examine each case
individually step by step giving more details.

In the case where $\theta_0 = 0°$, a continuous competition between the bands is ob-
served throughout the simulation, leading to constant changes in the shape of the
cavity. At stage (b), two intersecting bands initially form an X-shaped structure.
The bands are orthogonal, with one band forming a $\varphi_{sb} = 135°$ angle with the x-axis
(clockwise direction) and another forming a $\varphi_{sb} = 45°$ angle. The cavity exhibits
preferential deformation, aligning more with the slip direction of the band inclined at
$\varphi_{sb} = 135°$ rather than the one at $\varphi_{sb} = 45°$, as evidenced by the cavity's noticeable
tilt stretching to the left.

In stage (c), this preference of deformation along the band of $\varphi_{sb} = 135°$ shifts
sides, and the plasticity is accomodate by the band of $\varphi_{sb} = 45°$. However, the
deformation along the band at $\varphi_{sb} = 45°$ remains insufficient to redress the cavity
in the middle of the specimen. It is only in the final state (d) that an equivalence
between the overall contributions of the bands at $\varphi_{sb} = 135°$ and $\varphi_{sb} = 45°$ is
observed, resulting in a roughly symmetric cavity shape. This configuration suggests
a symmetric cavity evolution if further deformation occur.

For the case where $\theta_0 = \frac{54.7°}{2}$, there is a unique band that drives the evolution of
the cavity. In other words, there are no changes in slip activity to report between the
different stages of deformation, as this band remains active throughout the entire
deformation process, forming an angle of $\varphi_{sb} = 135°$ with the Ox-axis (clockwise
direction). Consequently, the initially circular void flattens and becomes increasingly
elliptical with progressive plastic deformation, elongating in the direction of this
band while compressing in the orthogonal direction. This process results in a very
elongated ellipse with a significantly reduced height (large eccentricity) and will
eventually lead to void closure with further deformation.

In the case of $\theta_0 = 65°$, we have a dominant band at $\varphi_{sb} = 45°$ that is responsible
to upward sliding of the upper half of the micropillar towards the right and causes

flattening of the right side of the cavity. The curvature of the left side of cavity have to do with another band with a secondary role in the deformation of cavity. This latter is a thin band that follows a curved path but is generally inclined at approximately $\varphi_{sb} = 60°$ to the Ox-axis. The second band together with the straight dominant band form an inclined X-shaped structure leaning to the right, somewhat resembling to a chromosome-like shape.

After discussing the evolution of cavity deformation, its relationship with slip localization and the initial crystal orientation, we now shift our focus to the rotation of lattice crystal depicted in Fig. 5.9. First, for micropillar with initial crystallographic orientation of $\theta_0 = 0°$, no rotation was observed outside of the bands. However, within the band oriented at $\theta = 135°$, globally a rotation of $-15°$ is observed, while the band at $\varphi_{sb} = 45°$ experiences a $15°$ rotation. This equivalent rotation of the bands offers an additional explanation for the symmetric shape of the void, complementing the previous explanation based on slip system activity. Since the band orientation forms a $15°$ angle with the glide direction, which is six times smaller than $90°$, it is much closer to the slip direction than to the normal of the slip direction. These rotations occur early in the deformation process and remain largely unchanged as deformation progresses. Based on this observation, the localized slip bands can be classified as shear bands.

Next, in the two remaining cases, the lattice rotation is much more pronounced, with a strong lattice rotation within the band with respect to the surrounding crystal. In case (2), within the single dominant band, a rotation of approximately $45°$ is observed by the end of the simulation. In case (3), the rotation reaches, or even exceeds, $90°$ in the dominant band. These large rotations suggest that the slip localization bands in these cases are better described as kink bands, given the higher degree of rotation compared to the shear bands observed in case (1).

The breakdown into slip/kink bands of a principal shear band was reported in [81] and related to strain-gradient plasticity models that incorporate softening effects. Although we employed here a classical crystal plasticity model, rather than a gradient plasticity model and did not introduce any explicit softening mechanisms, we nonetheless detected the formation of dense, intense, and parallel kink bands networks in the slip band (see the Fig.5.10 for a zoom of of Fig.5.9). While this phenomenon could be attributed to numerical instability, if not simply a computational artifact, it may instead represent localized plastic deformation occurring within the kink bands. The dense arrangement of parallel kink bands remains spatially con-
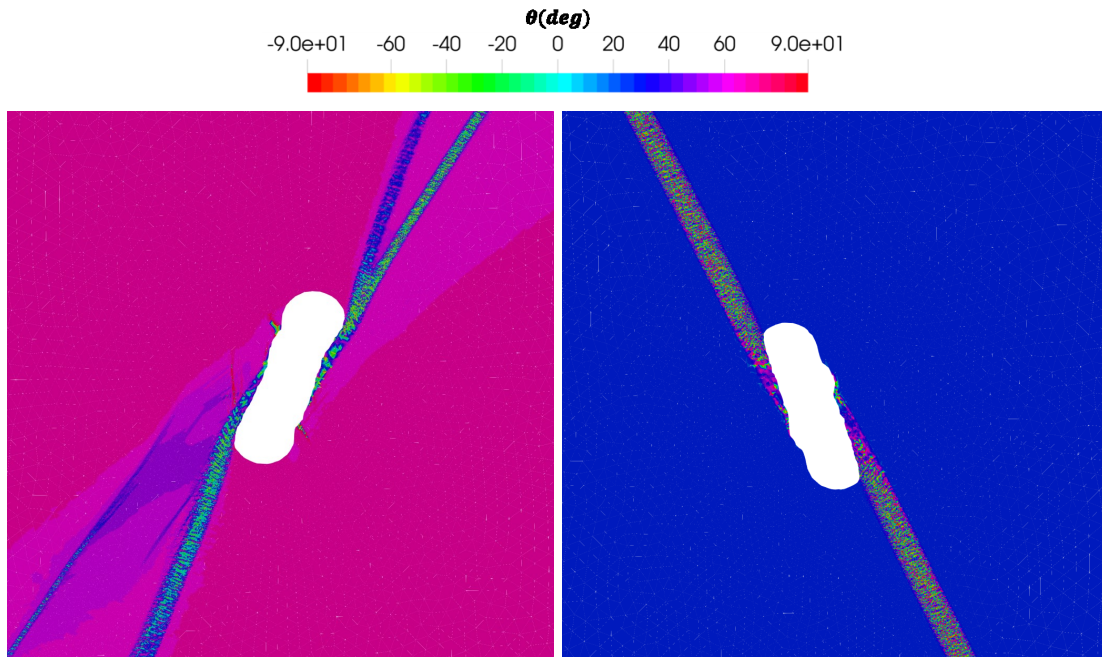
Figure 5.10: Zoomed view of the lattice orientation evolution around the deformed void for an FCC porous micropillar under tensile loading with initial crystallographic orientations $\theta_{ini} = 65°$ (left) and $\theta_{ini} = \dfrac{54.7°}{2}$ (right) at an engineering strain of $\epsilon^{engn} = 0.05$.

fined, concentrating slip activity. We have to note that this phenomenon, if it exists, is related to a three scale analysis: the sample scale, the shear band width scale and the kink bands width scale.

5.4   Conclusions

In this chapter the large deformations growth of voids in single crystals (as HCP, FCC) was investigated. An Eulerian crystal plasticity 2D model with 3 slip systems was used in finite element simulations. The voids deformation was analyzed under two types of loading: (i) radial and (ii) uni-axial. In both cases the voids, which have an initial circular shape, have a very different final shape. We have simplified our analysis to get a deeper understanding of complex phenomenon, by considering no hardening effects.

In case (i) we have analyzed firstly the onset of the deformation and compared our model with the other results (principally [98]) obtained with a small deformation Lagrangian model. We found a very good agreement by pointing out the formation of shear and kink bands. Secondly, we have pushed the computations for large

deformations and we found a final hexagonal shape of the void as reported in some experimental papers (see for instance [22]). We found that during the large strain evolution process the kink bands vanish and we deal with shear bands only. The orientation of the crystal around the void is given by the stability analysis presented in Chapter 3, with 6 lines of discontinuity but far from the void where accumulated deformations are not not large enough the crystal keeps its initial orientation. Due to the presence of the shear bands the stability analysis is not more valid very near the void, where the orientation is different from expected one.

In case (ii) we have considered three initial orientations of the crystal with respect to the loading axis. We get three different scenario of the void evolution. In all cases we deal with shear bands where the accumulated plastic strain is very large ($> 200\%$) even for moderate engineering strains ($< 15\%$). The presence of small kink/shear bands in the kink/shear bands could be the results of a computation artifact or a physical phenomenon acting at smaller scale than the shear band width. This needs further investigations with a FE code able to manage three scales: sample, shear band width and kink band width scales.

Chapter 6

Accounting for localized deformation: a simple computation of true stress in micropillar compression experiments

6.1 Introduction

Compression experiments conducted on pillars have proven to be a valuable method for analyzing the mechanical behavior of materials at the micro- and nano-scales. This approach involves the fabrication of micro-pillars (often with focused ion beam (FIB) techniques) followed by an uni-axial compression to study its mechanical response in a deformation process under displacement or load control. This method has been particularly useful for investigating the onset and evolution of plastic deformation in materials, by exploring the local deformation mechanism (when compression test are carried out in situ SEM), see for instance [126, 41, 93, 34, 66, 35, 137, 110, 136, 109, 23]. Specifically, micro-pillar compression experiments have revealed numerous new phenomena, including the transition from wild-to-mild plasticity [137], pristine-to-pristine plastic deformation [128], the "smaller is stronger" effect [73], size- and shape-dependent flow stresses [126, 79, 135] and, microstructural control of plastic flow [106], among others.

During such compression experiments, the material can undergo significant plastic deformation, which can manifest in either homogeneous deformation or slip/kink bands [43, 85, 10, 19, 92, 129, 94, 82, 138]. Homogeneous deformation occurs

when the material undergoes uniform deformation throughout its structure, while slip/kink bands result from localized deformation that can form along some preferred orientation [57, 37]. The resulting engineering strain-stress curve is related to a displacement-force experimental recording, but in order to accurately characterize the material's mechanical behavior, it is necessary to determine the Eulerian (true) stress that is exerted within the deformation zone. It is especially crucial to be able to accurately interpret the mechanical properties of engineered or designed materials using various methods to assess whether desired enhancements have been achieved [131, 38]. The significance of using true stress in assessing mechanical responses has been discussed in prior studies related to the mechanical behavior of metallic glass [47, 127]. However, of particular importance is the fact that, to the best of our knowledge, there is currently no established method to calculate the required load-bearing area to evaluate true stress, during plastic localization mechanisms.

In this context, the aim of this study is to derive simple formulas for calculating true stress in cases involving slip/kink band formation during mechanical loading while avoiding the need for lengthy and complex finite element computations that deal with large deformations of crystals. Specifically, we consider a localization, observed frequently in experiments as single band oriented in arbitrary directions with respect to the vertical axis of the pillar, for which we derive a formula and employ it to assess the reliability of previous experimental results. We have to mention here that the proposed formula is completely geometric. Contrary to Finite Elements computations, it does not need any material modeling setup, hence it could be very useful in choice of the constitutive law.

6.2   Simple modeling of pillars' deformation

After the initial loading process, which is associated with small-strain linear elastic behavior, the pillars undergo significant plastic deformation, making the elastic deformations negligible in comparison to the plastic ones. From these plastic deformation processes, two distinct scenarios emerge: homogeneous and slip/kink band, as illustrated schematically in Figure 6.1 and detailed subsequently. The Cauchy stress tensors corresponding to these two deformation mechanisms exhibit different patterns. In either scenario, the primary challenge is to determine the true stress σ^{true} within the uniaxial Cauchy stress tensor $\boldsymbol{\sigma} = -\sigma^{true}\boldsymbol{e}_z \otimes \boldsymbol{e}_z$, where $\boldsymbol{e}_i$ rep-
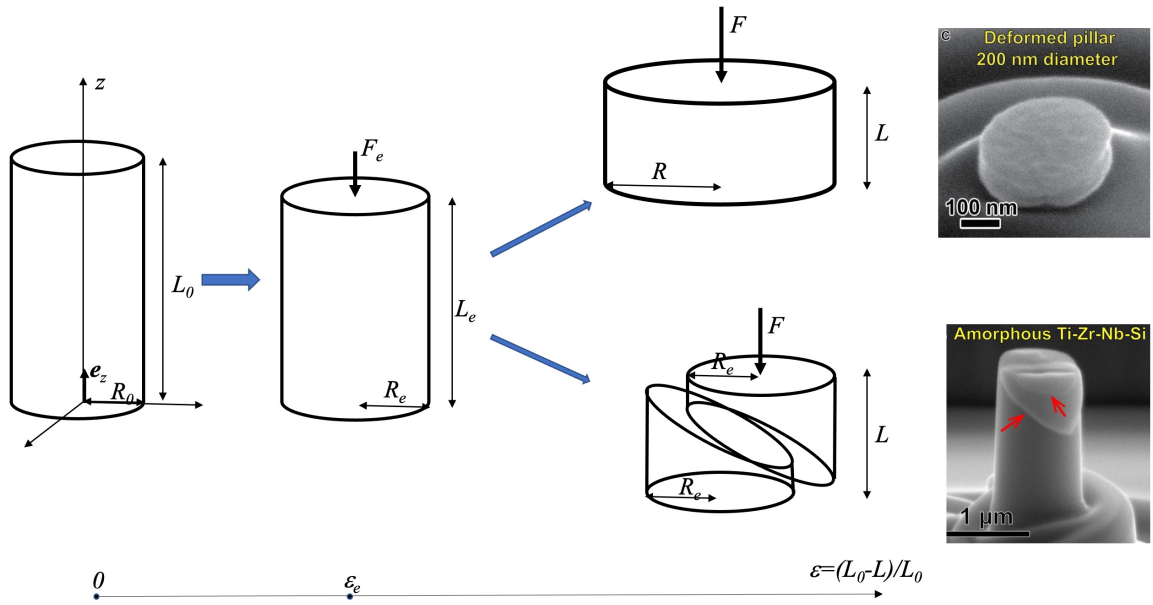
Figure 6.1: Schematic representation of the nano or micro-pillar deformation. The linear elastic regime, $\epsilon^{eng} < \epsilon_e$, is followed by one of the two types of plastic flow. Up: homogeneous deformation, Bottom: shear/kick band deformation (experimental illustration taken from [131]).

resents the elements of the orthonormal basis of the three-dimensional Euclidean vector space, acting on the active area A_u.

To be more specific, let R_0 and L_0 represent the initial (Lagrangian) radius and height of the cylindrical pillar, respectively, while R and L denote the current (Eulerian) dimensions during deformation, as shown in Fig. 6.1. Let $\epsilon^{eng} = (L_0 - L)/L_0$ denote the overall engineering strain. Let $\boldsymbol{F} = -F\boldsymbol{e}_z$ represent the force applied to the top of the pillar during deformation, where $F = \sigma^{true} A_u$, and let σ^{eng} denote the nominal (engineering) stress, i.e., $F = \sigma^{eng} A_0$, with $A_0 = \pi R_0^2$ is the original cross-sectional area.

We assume knowledge of the initial pillar shape, specifically the aspect ratio $f_0 = L_0/2R_0$, and have access to the engineering strain-stress curve, denoted as the function $\epsilon^{eng} \rightarrow \sigma^{eng}(\epsilon^{eng})$. The primary objective of this paper is to derive a simple formula for estimating the engineering strain-true stress curve, represented as $\epsilon^{eng} \rightarrow \sigma^{true}(\epsilon^{eng})$.
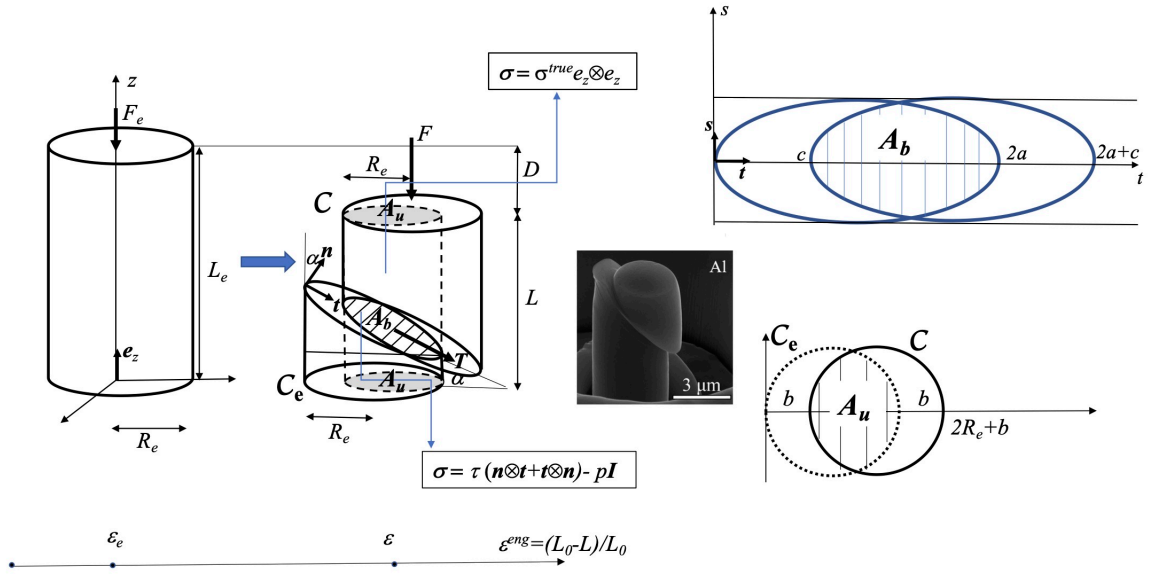
Figure 6.2: (Left): Schematic representation of localized plastic deformation following the elastic stage with the Cauchy stress tensor acting in different regions of the pillar. (Right, top): The plan of the shear band with its area A_b between two ellipses representing the upper and lower sections of the pillar. (Right, bottom) : Its projection on the horizontal plane (experimental image taken from [129]).

6.2.1 Elastic deformation

For $\epsilon^{eng} < \epsilon_e$ (or equivalently for $\sigma^{eng} < \sigma_e^{eng}$) the pillar exhibits a linear elastic behavior. Here, ϵ_e and $\sigma_e^{eng} = \sigma^{eng}(\epsilon_e)$ represent the strain and stress limits of elasticity, which can be easily identified in each stress-strain (or force-displacement) curve. Since the elastic strain limit ϵ_e, is usually small (less that 3%) the elastic linear theory can be accepted as a good approximation. If the deformed shape is also a cylinder and the stress is uniaxial throughout the pillar then $A_u = A = \pi R^2$, $F = \sigma^{true} \pi R^2$ and $\sigma^{eng} R_0^2 = \sigma^{true} R^2$. For anisotropic materials, such as monocrystals, during the elastic phase, the pillar is no longer a perfect cylinder. However, since the deformation is small, the deviation from a cylindrical shape can be neglected.

Following the Hooke's law the volumetric strain $\epsilon_V = (V_0 - V)/V_0 = (L_0 R_0^2 - LR^2)/L_0 R_0^2 = (1 - (1 - \epsilon^{eng})(R/R_0)^2)$ is related to the true stress through the compressibility modulus K by $\sigma^{true} = 3K\epsilon_V$. We get a second order algebraic

equation for $(R_0/R)^2$ to deduce that $(R_0/R)^2 = (1 - \sqrt{1 - 4\delta(1 - \epsilon^{eng})})/2\delta$, where $\delta = \sigma^{eng}/3K$. Finally we have

$$\sigma^{true} = \frac{3K - \sqrt{9K^2 - 12K\sigma^{eng}(1 - \epsilon^{eng})}}{2}, \quad \text{for } \epsilon^{eng} \leq \epsilon_e,$$

which for small values of $\delta_e = \sigma_e^{eng}/3K$ and ϵ_e, gives the well-known formula for true stress:

$$\sigma^{true} = \sigma^{eng}(1 - \epsilon^{eng}), \qquad \text{for } \epsilon^{eng} \leq \epsilon_e. \qquad (6.1)$$

Note that since $1 - \epsilon^{eng} \approx 1$ for $\epsilon^{eng} < \epsilon_e$ the difference between the true and engineering stress in not significant, and we can conclude that $\sigma^{true} \approx \sigma^{eng}$ during the elastic phase.

In most strain-stress curves, the elastic strain limit ϵ_e is usually easy to extract by considering the end of the linear behavior. In the following, ϵ_e will be considered as obtained from the experimental results, but this assumption will not imply any further considerations (i.e., ϵ_e) about the hardening or softening plastic behavior of the pillar.

6.2.2   Homogeneous uni-axial stress

For larger deformations, $\epsilon^{eng} > \epsilon_e$, in the first scenario the deformation is homogeneous and the stress throughout the entire pillar is assumed to be uni-axial, given by $\boldsymbol{\sigma} = -\sigma^{true}\boldsymbol{e}_z \otimes \boldsymbol{e}_z$, where $A_u = A = \pi R^2$. For materials modeled by a pressure-independent plasticity law, plastic deformation is isochoric and the volume is preserved. If the deformed shape remains a cylinder and we neglect the further elastic deformation of the volume then we get $V = \pi R^2 L = V_e = \pi R_e^2 L_e$, in which R_e and L_e are, respectively, the radius and length of the pillar at the end of elastic phase (i.e. fixed during post-elastic deformation). After some algebra we find

$$\sigma^{true} = \frac{\sigma_e^{true}}{\sigma_e^{eng}(1 - \epsilon_e)}\sigma^{eng}(1 - \epsilon^{eng}), \quad \text{for } \epsilon^{eng} > \epsilon_e.$$

Since for small values of $\delta_e = \sigma_e^{eng}/3K$ we have $\sigma_e^{true} = \sigma_e^{eng}(1 - \epsilon_e)$ we get the well known formula

$$\sigma^{true} = \sigma^{eng}(1 - \epsilon^{eng}), \quad \text{for } \epsilon^{eng} > \epsilon_e. \qquad (6.2)$$

However, for large values of ϵ^{eng}, using the nominal stress σ^{eng} instead of the Cauchy stress σ^{true} can significantly alter the behavior of the stress-strain diagram, giving a

false impression of overall hardening-like behavior.

Due to the boundary conditions on the top and bottom, the above assumption concerning the cylindrical shape of the deformed sample is not always valid. Indeed, barreling or bulging phenomena could occur, and the sample shape is given by two diameters (the middle one and the top/bottom one). If the minimum between the top/bottom and center radii, denoted by $R_m(\epsilon^{eng})$, could be measured during the experiment, then true stress can be directly computed through $\sigma^{true} = F/(\pi R_m^2(\epsilon^{eng}))$, and we do not need the above formula.

6.2.3   Slip/kink band plastic deformation

In the second scenario, for $\epsilon^{eng} > \epsilon_e$, deformation is localized in a narrow zone between two parallel planes with a normal vector $\boldsymbol{n}$, determined by the angle α with respect to the vertical axis $\boldsymbol{e}_z$, see Fig. 6.2.The Cauchy stress tensor acting in the shear band is given by $\boldsymbol{\sigma} = \tau(\boldsymbol{n} \otimes \boldsymbol{t} + \boldsymbol{t} \otimes \boldsymbol{n}) - p\boldsymbol{I}$, where $\boldsymbol{t}$ is the slip direction, τ is the shear stress and, $\boldsymbol{I}$ is the identity matrix, while in two cylindrical regions above and below the shear band it is assumed to be uniaxial, i.e., $\boldsymbol{\sigma} = \sigma^{true}\boldsymbol{e}_z \otimes \boldsymbol{e}_z$ (see Fig. 6.2). This assumption is a schematic representation of the stress distribution in the pillar with three non-vanishing uniform stress zones which allows analytic computations. Even if the stress distribution is expected to be much more complicate this assumption seems to be globally verified in FE computations (see for instance Fig 6.4 bottom).

From the above assumption we can deduce that the expression for shear stress τ, acting in the shear band, is proportional to the true stress:

$$\tau = \frac{1}{2}\sin(2\alpha)\sigma^{true}. \tag{6.3}$$

It should also be noted that if the true stress σ^{true} is known, then equation (6.3) enables the calculation of the shear stress τ as a function of the shear plastic strain γ_p, which is proportional to the plastic axial engineering strain and can be expressed as

$$\gamma_p = \frac{L_e - L}{\cos(\alpha)H_b} = \frac{(\epsilon^{eng} - \epsilon_e)L_0}{\cos(\alpha)H_b},$$

in which H_b represents the thickness of the shear band. The diagram of shear stress τ versus shear plastic strain γ_p is a very important tool in any discussion about the choice of the plastic model to be considered, both in crystal plasticity and for

amorphous materials.

Let us now compute the area A_u between the two disks (or equivalently $A_b = A_u/\cos(\alpha)$ the area between the two ellipses) $\mathcal{C}_e$ and $\mathcal{C}$ corresponding to the projection on the basal plane of the two cylinders (see Fig. 6.2). One of the circles is translated by a distance of $b = D \cot(\alpha)$, where $D = L_e - L$ is the vertical displacement of the upper pillar region. After some simple computations, one can find that the area A_u between the two regions is given by

$$A_u = R_e^2 \left[\pi - \frac{b}{R_e} \sqrt{1 - \frac{b^2}{4R_e^2}} - 2 \arcsin\left(\frac{b}{2R_e}\right) \right].$$

Denoting by $f_0 = L_0/2R_0$ the initial shape number and by $f_e = L_e/2R_e = (1 - \epsilon_e)^{3/2} f_0$ the shape number at the end of the elastic phase, and by $\epsilon_*^{eng} = (Le - L)/L_e = (\epsilon^{eng} - \epsilon_e)/(1 - \epsilon_e)$ the engineering (plastic) deformation with respect to the configuration at the end of the elastic phase, we get

$$A_u = R_e^2 \Phi(\epsilon_*^{eng} f_e \cot(\alpha)), \tag{6.4}$$

where we have denoted by

$$\Phi(s) = \pi - 2s\sqrt{1 - s^2} - 2 \arcsin(s).$$

Taking into account that $R_0^2/R_e^2 = (1 - \sqrt{1 - 4\delta_e(1 - \epsilon_e)})/2\delta_e$ we can deduce that:

$$\sigma^{true} = \frac{\sigma^{eng}\pi(1 - \sqrt{1 - 4\delta_e(1 - \epsilon_e)})}{2\delta_e\Phi((\epsilon^{eng} - \epsilon_e)f_e \cot(\alpha)/(1 - \epsilon_e))}, \quad \text{for } \epsilon^{eng} > \epsilon_e. \tag{6.5}$$

Bearing in mind that $\epsilon_*^{eng} f_e = (\epsilon^{eng} - \epsilon_e)f_0\sqrt{1 - \epsilon_e}$ for small values of ϵ_e and δ_e, we have $R_0^2/R_e^2 \approx 1 - \epsilon_e$ we can deduce a simplified formula for the true stress:

$$\sigma^{true} = \frac{\pi(1 - \epsilon_e)\sigma^{eng}}{\Phi((\epsilon^{eng} - \epsilon_e)f_0\sqrt{1 - \epsilon_e} \cot(\alpha))}, \quad \text{for } \epsilon^{eng} > \epsilon_e \tag{6.6}$$

Note that to use the simplified formula we only need to know the elastic limit ϵ_e, the shear band angle α and the initial aspect ratio f_0. However, the exact formula given in Eq. 6.5 requires also δ_e: the ratio between engineering stress σ_e^{eng} at the end of the elastic phase and the bulk modulus K.

In contrast to the homogeneous deformation scenario, here the true stress is larger than the engineering stress. Therefore, in many strain-stress diagrams, the

plateau or softening of the engineering stress should be viewed as a hardening of the true stress.

6.3   Comparison with 2-D FE computations

In the above model, the shear band thickness is assumed to be small relative to the specimen length (i.e., $H_b/L_0 \ll 1$), a condition verified in many situations. For experiments where this assumption is not verified, Eqs. (6.5) and (6.6) need to be revisited. Moreover, due to the Lagrangian description of large plastic deformations in the shear band, finite element simulations must contend with severe distortion of elements. Consequently, their results exhibit a shear band thickness that is unrealistically large, and computations are halted at intermediate strains (less than 20%). Consequently, a conclusive comparison between the above formulas and Lagrangian FE computations could not be made.

For this reason, we will use here an Eulerian approach in the FE computations, capable of describing thin shear bands. We will select an elastic perfectly plastic material (see the Appendix for the constitutive equation) with the Von-Mises yield limit σ_Y, such that the theoretical shear stress in the shear band is known ($\tau_{th} = \sigma_Y/\sqrt{3}$). From Equation (6.3), we can compute the theoretical true stress $\sigma_{th}^{true} = 2\sigma_Y/(\sqrt{3}\sin(2\alpha))$ for $\epsilon^{eng} > \epsilon_e$. Then, σ_{th}^{true} can be compared with the true stress σ^{true} computed from Equations (6.5) or (6.6) and the FE computations of the engineering stress σ^{eng}.

The ALE approaches of the shear bands, which require re-meshing at each time step, are computationally very expensive. Therefore, we have performed only 2-D computations here. For the two-dimensional case, the geometric true stress formula (Equation (6.6)) reads:

$$\sigma^{true} = \frac{(1 - \epsilon_e)\sigma^{eng}}{1 - (\epsilon^{eng} - \epsilon_e)f_0(1 - \epsilon_e)\cot(\alpha)}, \quad \text{for } \epsilon^{eng} > \epsilon_e. \qquad (6.7)$$

In Figure 6.3, we have plotted the evolution of the shear band in an elastic-perfectly plastic pillar of initial shape number $f_0 = 2$, with the following material constants: $E = 38235$ MPa, $\nu = 0.34$, $\sigma_Y = 1000$ MPa. We remark that the ALE computations of the Eulerian model were able to handle a thin shear band. The angle of the shear band is, as expected, $\alpha = 45$ at the beginning, but we observe a slight variation at the end of the deformation process. At the bottom of Fig.
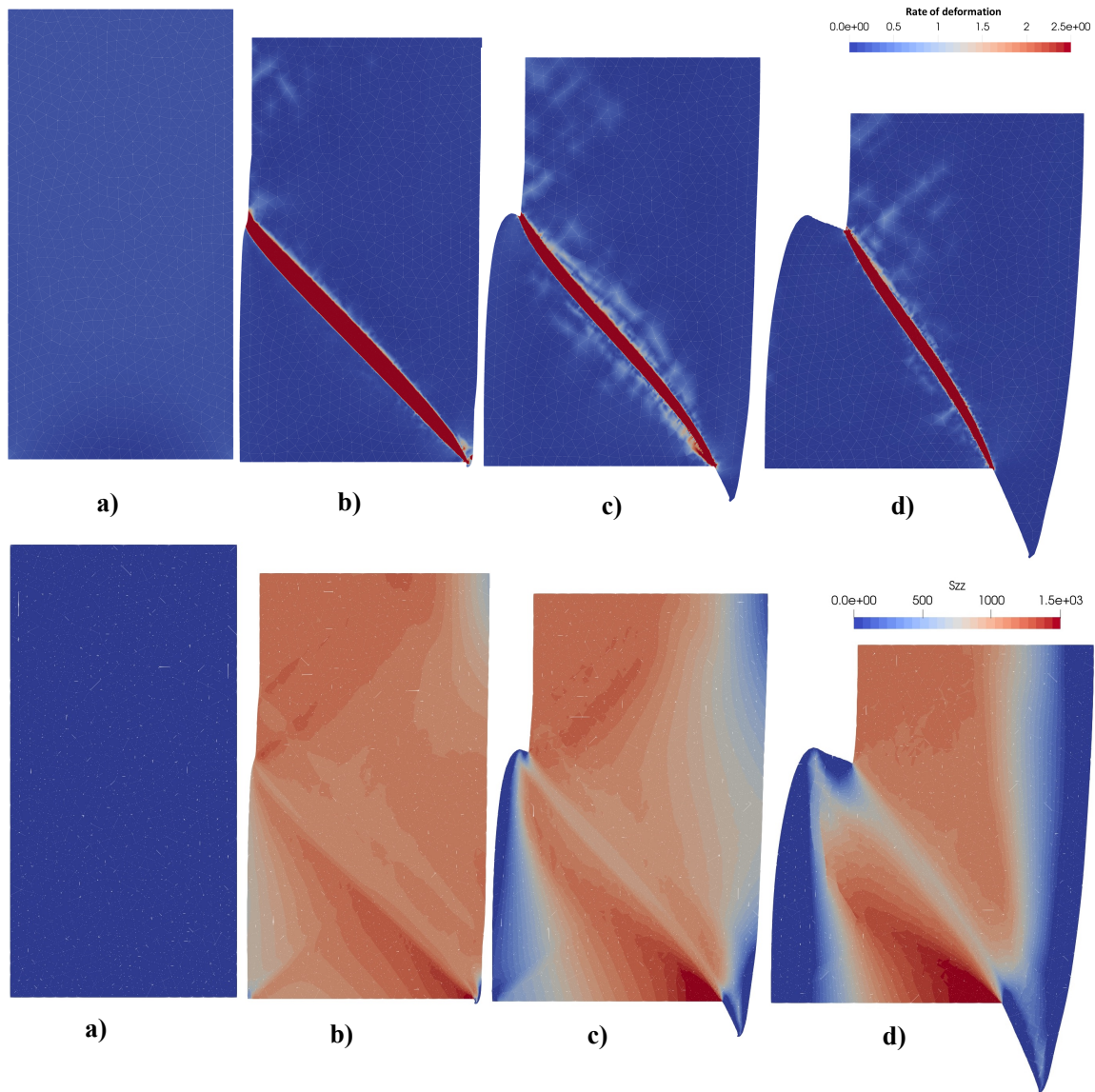
Figure 6.3: 2D Eulerian FE computation of the shear band localization in an elastic-perfectly plastic pillar with the plastic strain rate $\dot{\varepsilon}^p$ (up) and the Cauchy stress σ_{zz} (bottom) in color scale. Evolution for different values of ϵ^{eng}: 0% in (a), 5.5% in (b), 11% in (c) and 22% in (d).

6.3, the distribution of the Cauchy stress σ_{zz} is plotted. One can remark that this distribution has, globally, a good agreement with the schematic stress distribution plotted in Figure 6.2.

In Figure 6.4, we have plotted the engineering stress σ^{eng} (in orange) computed from the resultant force on the pillar's top of the FE simulations. From this curve, we obtain the elastic strain to be $\epsilon_e = 0.031$. In blue, we have plotted the theoretical true stress σ_{th}^{true} that we expect from the model, and in green, the true stress σ^{true} computed with Equation (6.7). We observe that the formula-based true stress closely aligns with the theoretical true stress up to $\epsilon^{eng} < 18\%$. After $\epsilon^{eng} = 18\%$, the true stress overestimates the theoretical one. This is due to the variation of the shear band angle α, which is larger at the end of the deformation process.
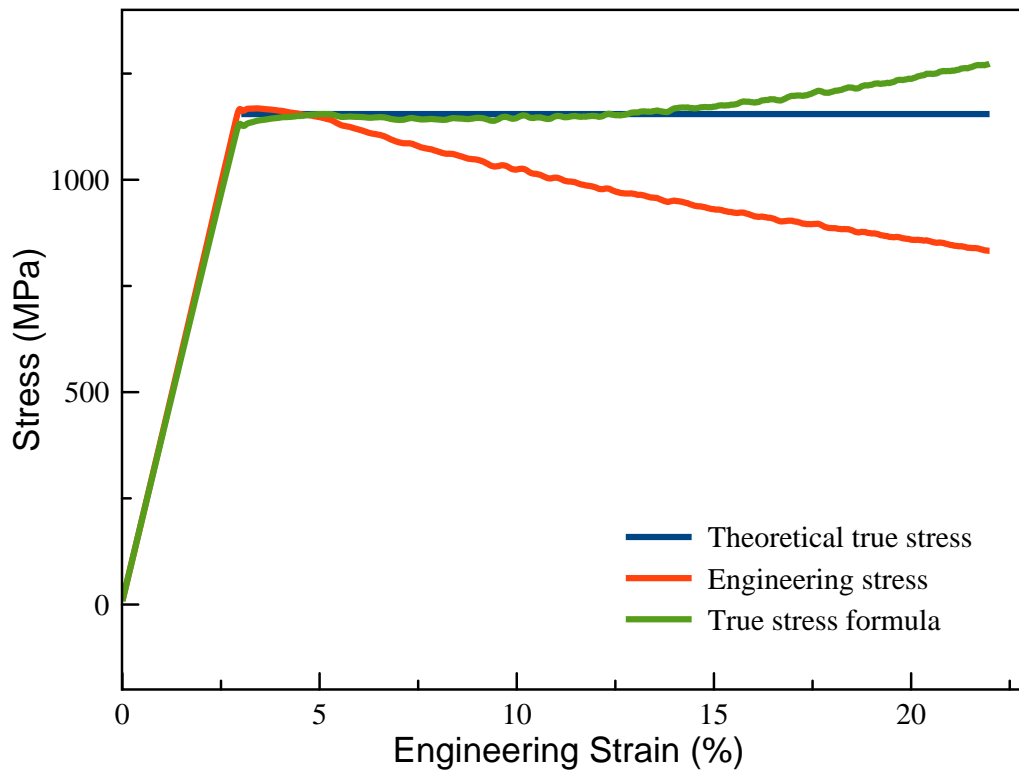

Figure 6.4: FE computations with an Eulerian elastic perfectly plastic model of the engineering stress σ^{eng} (in orange). In green the true stress σ^{true} computed with the formula (6.7) and in blue the theoretical true stress σ_{th}^{true} that we expect from the model.

6.4 True stress computation and re-interpretation of the stress-strain curves

In this section, we want to illustrate how the formulas deduced in the previous section alter some experimental engineering strain-stress curves reported in the literature.
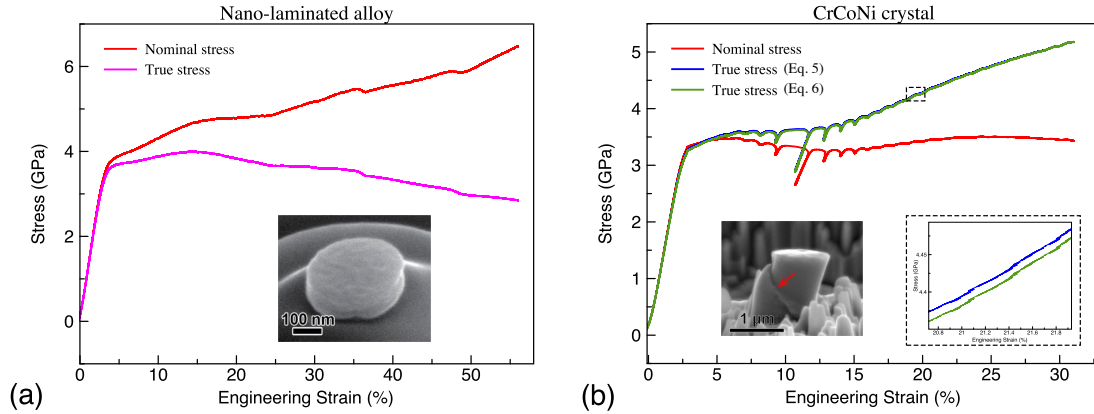

Figure 6.5: Engineering strain vs. nominal stress (red) and true stress (blue) curves. Nominal stress values are taken from [131]) and the calculated true stress curves are calculated using the formulas derived here. (a) homogeneous deformation of a crystal-glass nano-laminated alloy sample calculated with the classical formulas (6.1), (6.2); (b) single shear band deformation of a CrCoNi crystal calculated with formulas (6.1), (6.5) (blue) and simplified formula (6.6) (green). Insets show the final state of the pillar at the end of the loading.

As an example, we will reconsider the strain-stress behavior of a crystal-glass symbiotic alloy investigated in [131]. In this study, the authors plotted the engineering strain-stress curves to characterize the crystal-glass nano-laminated alloy sample's mechanical properties compared with its crystalline and amorphous counterparts. Interestingly, the authors found that the nano-laminated crystal-glass alloy appeared to be tougher than its individual components when analyzing the engineering stress data (see Fig. 4(a) in [131]). However, when we calculate the engineering strain vs. true stress curves for two cases: (i) the crystal-glass nano-laminated alloy undergoing homogeneous deformation using the conventional formula provided in (6.2); (ii) the CrCoNi crystal experiencing slip band deformation using (6.5) with $\alpha = \pi/4$, $f_0 = 1$, $\epsilon_e = 2.5\%$ and $\sigma_e^{eng} = 3.23$ GPa (or the simplified formula given in (6.6), we observe a contradictory outcome in both cases. Specifically, the nano-laminated alloy exhibits softening, as shown in Fig. 6.5(a), while the CrCoNi crystal demonstrates hardening, as depicted in Fig. 6.5(b). This finding emphasizes the significance of taking into account the current deformation state of the material, even

in the absence of a strong localization.

We have to notice that, for the nano-laminated crystal-glass alloy, we deal with a bulging deformation, and one could expect that the true stress obtained through (6.2) is slightly underestimated. Indeed, from the final shape of the pillar, we observe that the central radius R_m is less than 3% of the volume-preserving radius R, hence the underestimation of true stress is less than 6% at the end of the deformation. This is negligible with respect to the difference between engineering and true stress, plotted in Fig. 6.5(a), which is on the order of 100%, and cannot change the above conclusions.

Lastly, we emphasize that when comparing the true stress curves obtained using (6.5) and the simplified formulas provided in (6.6), as shown in Fig. 6.5(b), we observed minimal differences, even at high strains.

6.5   Conclusion

In conclusion, our study provides formulas for calculating true stress in cases where slip/kink bands form during mechanical loading in compression experiments on pillars. These formulas are simple and need only the engineering stress data, some geometric data (aspect ratio), and some mechanical data (elastic limit) which are easy to get from the experimental results. For slip/kink band plastic deformation the shear stress τ acting in the band can be recovered from the uniaxial true stress σ^{true}. The diagram shear plastic strain- shear stress is then the main information on the mechanical behavior of the material that can obtained from a pillar experiment with a shear band localization.

Of course, our formula does not consider bending and torsion, which cannot be easily traced by simple geometrical arguments. However, in our opinion, their effects will be of second-order. In a 2D finite element numerical simulation of Eulerian elasto-plastic pillar compression, we compared the formula-based true stress with the theoretical true stress and we found a good agreement.

A more precise alternative to these simple formulas could be very long and difficult FE computations involving large deformations. Moreover, the FE computations needs to know in advance the material type (mono-crystal, poly-crystal, isotropic), its behavior (hardening, softening, etc) and the constants that characterize the material. This means that when localization occurs, the proposed geometric formula gives the possibility to experimenters to interpret the data in a simple manner with-

out any preconceived notions about the choice of model.

However, using these formulas, we re-evaluated the robustness of previous experimental results and found that considering the current deformation state of engineered materials can be important for accurately interpreting their mechanical behavior at small scales. To be more precise, our analysis revealed that, in some cases, the true stress led to conclusions that were exactly opposite to those found using the engineering stress, while in other cases, the difference is mainly quantitative and the overall trend is similar. To conclude, our work provides a valuable tool for accurately interpreting the mechanical behavior of materials under compressive loads and for drawing appropriate conclusions based on the true stress values.

Chapter 7

Conclusion

The Lagrangian framework, which follows the particles, involves important theoretical and numerical difficulties for very large deformations. The Eulerian approach, which is particularly effective for simulating extreme deformations and uses a fixed grid which allows materials to flow through without distorting the mesh, making it ideal for analyzing complex material behavior during severe plastic deformation. That is why we have adopted here an Eulerian crystal plasticity model to provide a comprehensive analysis of the crystal evolution during large deformations.

During the deformation process we deal with both elastic and (visco-)plastic strains. Since elasticity needs a reference configuration, a Lagrangian description is more appropriated while for the plastic flow phenomena an Eulerian framework seem more adapted. That is why the elastic-(visco-)plastic model needs a permanent interplay between both descriptions. However, in applications involving large deformations of metals the elastic component of the deformation is small with respect to the inelastic one, and can be neglected by using a rigid-(visco)plastic approach (see for instance [56, 71, 69, 72]). This simplified model, used in this thesis, takes important theoretical and numerical advantages by using only one (Eulerian) configuration.

Understanding this stability of crystallographic orientations is essential for predicting material behavior under stress. Indeed, during deformation, lattice orientations tend to stabilize around specific configurations, often referred to as lattice orientation attractors. To theoretically address this issue we have considered here only velocity gradient driven processes without hardening or softening effects for the 2D model with three slip systems. The stable stationary orientations have been characterized with their attraction basins, Since the attractors are effective for large

slip strains this stability analysis, is not so useful for small strains. Two numerical simulations illustrate the theoretical results. In both cases the overall final orientation of the lattice is very close to the a priori attractors distribution predicted by the stability analysis. The first simulation concerns a homogeneous driven velocity gradient field with a nonhomegeous initial orientations, modeling the grains of a poly-cristal. The computed orientation is in a very good accord with the predicted one with a gap average (in L^2 norm) less than $4°$. In the second case a mono-crystal (homogeneous initial orientation) but with a driven non-homogeneous velocity gradient (void growth under radial loading) was considered. The numerical simulations point out that, accordingly with stability analysis, the orientation exhibits 6 discontinuity angles, as the attractor does. These discontinuities are present near the void, where the deformations are large enough, and vanish near the external boundary where the deformation is small and the attractor is not effective. Very close to the void, deformation process is much more complex (slip and kink bands appears) and the lattice orientation is not so sharply estimated by the attractor.

Dislocation-density based crystal plasticity models are introduced to account for the microstructral changes throughout the deformation process. The stability of the dislocation densities in slip rate driven processes was investigated in this thesis. Some established dislocation density-based models, including the Kocks and Mecking (KM) model and its variants, were considered to identify conditions for stationary states in active slip systems and evaluate their linear stability. The conclusions of this analysis could uncover size-dependent effects manifesting through initial dislocation density variations, influencing the material's softening or hardening responses. Numerical simulations of micro-pillar compression using an Eulerian crystal plasticity approach were done to address the behavior of materials at micro-scale dimensions. They indicate that microstructural evolution in small-scale materials can be effectively modeled using dislocation-density based CP models, providing valuable insights for the design of miniaturized mechanical devices and advanced materials in the rapidly evolving field of nanotechnology.

The mechanisms of void growth and coalescence are key contributors to the ductile failure of crystalline materials, occurring through plastic flow around pre-existing voids or nucleated cavities at second-phase particles. Even if there exists an important literature on the subject the large deformation of voids growth in single crystals, is less investigated. The 2D model with 3 slip systems, used in this thesis, to characterize the large deformation of voids and their shape evolution was used for

two types of loading: (i) radial and (ii) uni-axial. In both cases the voids, which have an initial circular shape, have a very different final shape. We have simplified our analysis to get a deeper understanding of complex phenomenon, by considering no hardening effects. In case (i) we have analyzed firstly the onset of the deformation and compared our model with the other results (principally [98]) obtained with a small deformation Lagrangian model. We found a very good agreement by pointing out the formation of shear kink bands. Secondly, we have pushed the computations for large deformations and we found a final hexagonal shape of the void as reported in some experimental papers (see for instance [22]). In case (ii) we have considered three initial orientations of the crystal with respect to the loading axis. We get three different scenario of the void evolution. In all cases we deal with shear bands where the accumulated plastic strain is very large ($> 200\%$) even for moderate engineering strains ($< 15\%$).

Compression experiments conducted on pillars have proven to be a valuable method for analyzing the mechanical behavior of materials at the micro- and nano-scales. The resulting engineering strain-stress curve is related to a displacement-force experimental recording, but in order to accurately characterize the material's mechanical behavior, it is necessary to determine the Eulerian (true) stress that is exerted within the deformation zone. Formulas for calculating true stress in cases where slip/kink bands form during mechanical loading in compression experiments on pillars, were obtained in this thesis. These formulas are simple and need only the engineering stress data, some geometric data (aspect ratio), and some mechanical data (elastic limit) which are easy to get from the experimental results. For slip/kink band plastic deformation the shear stress τ acting in the band can be recovered from the uniaxial true stress σ^{true}. The diagram shear plastic strain-shear stress is then the main information on the mechanical behavior of the material that can obtained from a pillar experiment with a shear band localization. In a 2D finite element numerical simulation of Eulerian elasto-plastic pillar compression, we compared the formula-based true stress with the theoretical true stress and we found a good agreement. Our analysis revealed that, in some cases, the true stress led to conclusions that were exactly opposite to those found using the engineering stress, while in other cases, the difference is mainly quantitative and the overall trend is similar.

Bibliography

[1] S. Agaram, A. K. Kanjarla, B. Bhuvaraghan, and S. M. Srinivasan. Dislocation density based crystal plasticity model incorporating the effect of precipitates in IN718 under monotonic and cyclic deformation. *Int. J. Plast.*, 141:102990, June 2021.

[2] A. Alankar, P. Eisenlohr, and D. Raabe. A dislocation density-based crystal plasticity constitutive model for prismatic slip in α-titanium. *Acta Mater.*, 59(18):7003–7009, Oct. 2011.

[3] J. Alcala, O. Casals, and J. Ocenasek. Micromechanics of pyramidal indentation in fcc metals: Single crystal plasticity finite element analysis. *Journal of the Mechanics and Physics of Solids*, 56(11):3277–3303, 2008.

[4] M. Ardeljan, M. Knezevic, T. Nizolek, I. J. Beyerlein, N. A. Mara, and T. M. Pollock. A study of microstructure-driven strain localizations in two-phase polycrystalline hcp/bcc composites using a multi-scale model. *International Journal of Plasticity*, 74:35–57, 2015.

[5] R. Asaro and A. Needleman. Overview no. 42 texture development and strain hardening in rate dependent polycrystals. *Acta Metallurgica*, 33(6):923–953, 1985.

[6] R. J. Asaro. Crystal plasticity. *J. Appl. Mech.*, 50(4b):921–934, Dec. 1983.

[7] R. J. Asaro and A. Needleman. Overview no. 42 texture development and strain hardening in rate dependent polycrystals. *Acta Metall.*, 33(6):923–953, June 1985.

[8] R. J. Asaro and J. R. Rice. Strain localization in ductile single crystals. *J. Mech. Phys. Solids*, 25(5):309–338, Oct. 1977.

[9] R. A. Austin and D. L. McDowell. A dislocation-based constitutive model for viscoplastic deformation of fcc metals at very high strain rates. *Int. J. Plast.*, 27(1):1–24, Jan. 2011.

[10] A. Basak, A. Pramanik, and C. Prakash. Deformation and strengthening of sic reinforced al-mmcs during in-situ micro-pillar compression. *Materials Science and Engineering: A*, 763:138141, 2019.

[11] H. Bei, S. Shim, E. George, M. Miller, E. Herbert, and G. Pharr. Compressive strengths of molybdenum alloy micro-pillars prepared using a new technique. *Scripta Materialia*, 57(5):397–400, 2007.

[12] U. Borg and J. W. Kysar. Strain gradient crystal plasticity analysis of a single crystal containing a cylindrical void. *International Journal of Solids and Structures*, 44(20):6382–6397, 2007.

[13] C. M. Byer and K. Ramesh. Effects of the initial dislocation density on size effects in single-crystal magnesium. *Acta Materialia*, 61(10):3808–3818, 2013.

[14] O. Cazacu and I. R. Ionescu. Augmented lagrangian method for eulerian modeling of viscoplastic crystals. *Computer Methods in Applied Mechanics and Engineering*, 199(9):689–699, 2010.

[15] O. Cazacu and I. R. Ionescu. Dynamic crystal plasticity: An eulerian approach. *J. Mech. Phys. Solids*, 58(6):844–859, June 2010.

[16] T. Chauve, M. Montagnat, F. Barou, K. Hidas, A. Tommasi, and D. Mainprice. Investigation of nucleation processes during dynamic recrystallization of ice using cryo-ebsd. *Philosophical Transactions of the Royal Society A: Mathematical, Physical and Engineering Sciences*, 375(2086):20150345, 2017.

[17] T. Chauve, M. Montagnat, V. Dansereau, P. Saramito, K. Fourteau, and A. Tommasi. A physically-based formulation for texture evolution during dynamic recrystallization. A case study of ice. *Comptes Rendus. Mécanique*, 352:99–134, 2024.

[18] T. Chauve, M. Montagnat, and P. Vacher. Strain field evolution during dynamic recrystallization nucleation; a case study on ice. *Acta Materialia*, 101:116–124, 2015.

[19] M. Chen, L. Pethö, A. Sologubenko, H. Ma, J. Michler, R. Spolenak, and J. Wheeler. Achieving micron-scale plasticity and theoretical strength in silicon. *Nature Communications*, 11:2681, 05 2020.

[20] Y. S. Chen, W. Choi, S. Papanikolaou, and J. P. Sethna. Bending crystals: emergence of fractal dislocation structures. *Phys. Rev. Lett.*, 105(10):105501, Sept. 2010.

[21] A. H. Cottrell. Commentary. a brief view of work hardening. In F. R. N. Nabarro and M. S. Duesbery, editors, *Dislocations in Solids*, volume 11, pages vii–xvii. Elsevier, Jan. 2002.

[22] J. Crepin, T. Bretheau, and D. Caldemaison. Cavity growth and rupture of β-treated zirconium: A crystallographic model. *Acta Materialia*, 44(12):4927–4935, 1996.

[23] Y. Cui, E. Aydogan, J. G. Gigax, Y. Wang, A. Misra, S. A. Maloy, and N. Li. In situ micro-pillar compression to examine radiation-induced hardening mechanisms of fecral alloys. *Acta Materialia*, 202:255–265, 2021.

[24] Y. Cui, P. Lin, Z. Liu, and Z. Zhuang. Theoretical and numerical investigations of single arm dislocation source controlled plastic flow in fcc micropillars. *International Journal of Plasticity*, 55:279–292, 2014.

[25] A. M. Cuitino and M. Ortiz. Computational modelling of single crystals. *Modell. Simul. Mater. Sci. Eng.*, 1(3):225, Apr. 1993.

[26] B. Devincre, T. Hoc, and L. Kubin. Dislocation mean free paths and strain hardening of crystals. *Science*, 320(5884):1745–1748, 2008.

[27] D. M. Dimiduk, C. Woodward, R. Lesar, and M. D. Uchic. Scale-free intermittent flow in crystal plasticity. *Science*, 312(5777):1188–1190, May 2006.

[28] F. Duarte, R. Gormaz, and S. Natesan. Arbitrary lagrangian–eulerian method for navier–stokes equations with moving boundaries. *Computer Methods in Applied Mechanics and Engineering*, 193(45-47):4819–4836, 2004.

[29] J. A. El-Awady, C. Woodward, D. M. Dimiduk, and N. M. Ghoniem. Effects of focused ion beam induced damage on the plasticity of micropillars. *Phys. Rev. B*, 80:104104, Sep 2009.

[30] Y. Estrin and H. Mecking. A unified phenomenological description of work hardening and creep based on one-parameter models. *Acta metallurgica*, 32(1):57–70, 1984.

[31] S. Forest. Modeling slip, kink and shear banding in classical and generalized single crystal plasticity. *Acta Mater.*, 46(9):3265–3281, May 1998.

[32] M. Fortin and R. Glowinski. *Méthodes de Lagrangien Augmentés: Application à la Résolution de Problèmes aux Limites*. Dunod, Paris, 1982.

[33] P. Franciosi, M. Berveiller, and A. Zaoui. Latent hardening in copper and aluminium single crystals. *Acta Metallurgica*, 28(3):273–283, 1980.

[34] C. Frick, B. Clark, S. Orso, A. Schneider, and E. Arzt. Size effect on strength and strain hardening of small-scale [111] nickel compression pillars. *Materials Science and Engineering: A*, 489(1):319–329, 2008.

[35] N. Friedman, A. T. Jennings, G. Tsekenis, J.-Y. Kim, M. Tao, J. T. Uhl, J. R. Greer, and K. A. Dahmen. Statistics of dislocation slip avalanches in nanosized single crystals show tuned critical behavior predicted by a simple mean field model. *Phys. Rev. Lett.*, 109(9):095507, Aug. 2012.

[36] F. Fritzen, S. Forest, T. Böhlke, D. Kondo, and T. Kanit. Computational homogenization of elasto-plastic porous metals. *International Journal of Plasticity*, 29:102–119, 2012.

[37] K. Gan, S. Zhu, S. Jiang, and Y. Huang. Study on stochastic nature of plasticity of cu/zr metallic glass micropillars. *Journal of Alloys and Compounds*, 831:154719, 2020.

[38] M. Ghidelli, A. Orekhov, A. L. Bassi, G. Terraneo, P. Djemia, G. Abadias, M. Nord, A. Béché, N. Gauquelin, J. Verbeeck, J.-P. Raskin, D. Schryvers, T. Pardoen, and H. Idrissi. Novel class of nanostructured metallic glass films with superior and tunable mechanical properties. *Acta Materialia*, 213:116955, 2021.

[39] R. Glowinski and O. Pironneau. Finite element methods for navier-stokes equations. *Annual Review of Fluid Mechanics*, 24(Volume 24, 1992):167–204, 1992.

[40] R. Glowinski and P. L. Tallec. *Augmented Lagrangian and Operator Splitting Methods in Nonlinear Mechanics*. SIAM Studies in Applied Mathematics. Society for Industrial and Applied Mathematics (SIAM), Philadelphia, PA, 1989.

[41] J. R. Greer, W. C. Oliver, and W. D. Nix. Size dependence of mechanical properties of gold at the micron scale in the absence of strain gradients. *Acta Mater.*, 53(6):1821–1830, Apr. 2005.

[42] H.-J. Guo, C. Ling, E. P. Busso, Z. Zhong, and D.-F. Li. Crystal plasticity based investigation of micro-void evolution under multi-axial loading conditions. *International Journal of Plasticity*, 129:102673, 2020.

[43] K. Hagihara, T. Mayama, M. Honnami, M. Yamasaki, H. Izuno, T. Okamoto, T. Ohashi, T. Nakano, and Y. Kawamura. Orientation dependence of the deformation kink band formation behavior in zn single crystal. *International Journal of Plasticity*, 77:174–191, 2016.

[44] M. Hajian, M. Khajeh Salehani, and A. Assempour. Prediction of ideal orientations and lattice rotations of fcc crystals in the equibiaxial tension loading: a rate-dependent crystal plasticity approach. *Mathematics and Mechanics of Solids*, 21(10):1247–1259, 2016.

[45] M. Hajian, M. Khajeh Salehani, A. Assempour, and H. Mehdigholi. Deformation mode dependency of stable orientations: from plane strain compression to equibiaxial tension. *Philosophical Magazine*, 95(7):794–803, 2015.

[46] X. Han, J. Besson, S. Forest, B. Tanguy, and S. Bugat. A yield function for single crystals containing voids. *International Journal of Solids and Structures*, 50(14):2115–2131, 2013.

[47] Z. Han, H. Yang, W. F. Wu, and Y. Li. Invariant critical stress for shear banding in a bulk metallic glass. *Applied Physics Letters*, 93(23):231912, 12 2008.

[48] S. Harren, H. Dève, and R. Asaro. Shear band formation in plane strain compression. *Acta Metall.*, 36(9):2435–2480, Sept. 1988.

[49] F. Hecht. New development in freefem++. *J. Numer. Math.*, 20(3-4):251–265, 2012.

[50] R. Hill. Generalized constitutive relations for incremental deformation of metal crystals by multislip. *J. Mech. Phys. Solids*, 14(2):95–102, Mar. 1966.

[51] R. Hill and J. R. Rice. Constitutive analysis of elastic-plastic crystals at arbitrary strain. *J. Mech. Phys. Solids*, 20(6):401–413, Dec. 1972.

[52] D. Hu, Z. Guo, N. Grilli, A. Tay, Z. Lu, and W. Yan. Understanding the strain localization in additively manufactured materials: Micro-scale tensile tests and crystal plasticity modeling. *International Journal of Plasticity*, 177:103981, 2024.

[53] J. Hu, Z. Zhuang, F. Liu, X. Liu, and Z. Liu. Investigation of grain boundary and orientation effects in polycrystalline metals by a dislocation-based crystal plasticity model. *Computational Materials Science*, 159:86–94, 2019.

[54] T. J. Hughes, W. K. Liu, and T. K. Zimmermann. Lagrangian-eulerian finite element formulation for incompressible viscous flows. *Computer methods in applied mechanics and engineering*, 29(3):329–349, 1981.

[55] J. Hure. A coalescence criterion for porous single crystals. *Journal of the Mechanics and Physics of Solids*, 124:505–525, 2019.

[56] J. W. Hutchinson. Bounds and self-consistent estimates for creep of poly-crystalline materials. *Proceedings of the Royal Society of London. Series A, Mathematical and Physical Sciences*, 348(1652):101–127, 1976.

[57] T. Inamura. Geometry of kink microstructure analysed by rank-1 connection. *Acta Materialia*, 173:270–280, 2019.

[58] P. P. Indurkar, S. P. Joshi, and A. A. Benzerga. On the micromechanics of void mediated failure in hcp crystals. *Journal of the Mechanics and Physics of Solids*, 165:104923, 2022.

[59] I. R. Ionescu. Onset and dynamic shallow flow of a viscoplastic fluid on a plane slope. *Journal of non-newtonian fluid mechanics*, 165(19-20):1328–1341, 2010.

[60] I. R. Ionescu. Augmented lagrangian for shallow viscoplastic flow with topography. *Journal of Computational Physics*, 242:544–560, 2013.

[61] A. Irastorza-Landa, H. Van Swygenhoven, S. Van Petegem, N. Grilli, A. Boll-halder, S. Brandstetter, and D. Grolimund. Following dislocation patterning during fatigue. *Acta Mater.*, 112:184–193, June 2016.

[62] A. T. Jennings, M. J. Burek, and J. R. Greer. Microstructure versus size: Mechanical properties of electroplated single crystalline cu nanopillars. *Phys. Rev. Lett.*, 104(13):135503, Apr. 2010.

[63] T. Kameda and M. Zikry. Three dimensional dislocation-based crystalline constitutive formulation for ordered intermetallics. *Scripta Materialia*, 38(4):631–636, 1998.

[64] M. Khajeh Salehani, M. Hajian, and A. Assempour. Ideal orientations of bcc crystals under equibiaxial tension loading. *Mathematics and Mechanics of Solids*, 21(8):1026–1042, 2016.

[65] P. H. Khavasad and S. M. Keralavarma. Effective yield criterion for a porous single crystal accounting for void size effects. *Mechanics of Materials*, 160:103950, 2021.

[66] D. Kiener, P. Guruprasad, S. Keralavarma, G. Dehm, and A. Benzerga. Work hardening in micropillar compression: In situ experiments and modeling. *Acta Materialia*, 59(10):3825–3840, 2011.

[67] D. Kiener, C. Motz, M. Rester, M. Jenko, and G. Dehm. Fib damage of cu and possible consequences for miniaturized mechanical tests. *Materials Science and Engineering: A*, 459(1):262–272, 2007.

[68] M. Knezevic, B. Drach, M. Ardeljan, and I. J. Beyerlein. Three dimensional predictions of grain scale plasticity and grain boundaries using crystal plasticity finite element models. *Computer Methods in Applied Mechanics and Engineering*, 277:239–259, 2014.

[69] S. Kok, A. Beaudoin, and D. Tortorelli. A polycrystal plasticity model based on the mechanical threshold. *International Journal of Plasticity*, 18(5):715–741, 2002.

[70] L. Kubin, B. Devincre, and T. Hoc. Modeling dislocation storage rates and mean free paths in face-centered cubic crystals. *Acta materialia*, 56(20):6040–6049, 2008.

[71] R. Lebensohn and C. Tomé. A self-consistent anisotropic approach for the simulation of plastic deformation and texture development of polycrystals: Application to zirconium alloys. *Acta Metallurgica et Materialia*, 41(9):2611–2624, 1993.

[72] R. A. Lebensohn, C. Tomé, and P. Maudlin. A selfconsistent formulation for the prediction of the anisotropic behavior of viscoplastic polycrystals with voids. *Journal of the Mechanics and Physics of Solids*, 52(2):249–278, 2004.

[73] S.-W. Lee, S. M. Han, and W. D. Nix. Uniaxial compression of fcc au nanopillars on an mgo substrate: The effects of prestraining and annealing. *Acta Materialia*, 57(15):4404–4415, 2009.

[74] J. Li, H. Proudhon, A. Roos, V. Chiaruttini, and S. Forest. Crystal plasticity finite element simulation of crack growth in single crystals. *Computational Materials Science*, 94:191–197, 2014. IWCMM23 Special Issue.

[75] S. Li. Orientation stability in equal channel angular extrusion. part i: Face-centered cubic and body-centered cubic materials. *Acta materialia*, 56(5):1018–1030, 2008.

[76] C. Ling, J. Besson, S. Forest, B. Tanguy, F. Latourte, and E. Bosso. An elasto-viscoplastic model for porous single crystals at finite strains and its assessment based on unit cell simulations. *International Journal of Plasticity*, 84:58–87, 2016.

[77] A. Ma, F. Roters, and D. Raabe. A dislocation density based constitutive model for crystal plasticity FEM including geometrically necessary dislocations. *Acta Mater.*, 54(8):2169–2179, May 2006.

[78] A. Ma, F. Roters, and D. Raabe. On the consideration of interactions between dislocations and grain boundaries in crystal plasticity finite element modeling – theory, experiments, and simulations. *Acta Mater.*, 54(8):2181–2194, May 2006.

[79] R. Maaß, L. Meza, B. Gan, S. Tin, and J. Greer. Ultrahigh strength of dislocation-free ni3al nanocubes. *Small*, 8(12):1869–1875, 2012.

[80] J. Mandel. Plasticite classique et viscoplasticite: course held... udine, September-October 1971, 1972.

[81] A. Marano, L. Gélébart, and S. Forest. Fft-based simulations of slip and kink bands formation in 3d polycrystals: Influence of strain gradient crystal plasticity. *Journal of the Mechanics and Physics of Solids*, 149:104295, 2021.

[82] A. Marano, L. Gelebart, and S. Forest. Fft-based simulations of slip and kink bands formation in 3d polycrystals: Influence of strain gradient crystal plasticity. *Journal of the Mechanics and Physics of Solids*, 149:104295, 2021.

[83] V. Maronnier, M. Picasso, and J. Rappaz. Numerical simulation of three-dimensional free surface flows. *International journal for numerical methods in fluids*, 42(7):697–716, 2003.

[84] B. Maury. Characteristics ale method for the unsteady 3d navier-stokes equations with a free surface. *International Journal of Computational Fluid Dynamics*, 6(3):175–188, 1996.

[85] C. Mayer, L. Yang, S. Singh, J. Llorca, J. Molina-Aldareguia, Y. Shen, and N. Chawla. Anisotropy, size, and aspect ratio effects on micropillar compression of alsic nanolaminate composites. *Acta Materialia*, 114:25–32, 2016.

[86] A. Mbiakop, A. Constantinescu, and K. Danas. An analytical model for porous single crystals with ellipsoidal voids. *Journal of the Mechanics and Physics of Solids*, 84:436–467, 2015.

[87] P. E. McHugh. Introduction to crystal plasticity theory. In H. J. Böhm, editor, *Mechanics of Microstructured Materials*, pages 125–171. Springer Vienna, Vienna, 2004.

[88] P. E. McHugh, R. J. Asaro, and C. F. Shih. Computational modeling of metal matrix composite materials—i. isothermal deformation patterns in ideal microstructures. *Acta Metall. Mater.*, 41(5):1461–1476, May 1993.

[89] H. Mecking and K. Lucke. A new aspect of the theory of flow stress of metals. *Scripta Metallurgica*, 4(6):427–432, 1970.

[90] K. M. Min, H. Lee, H.-D. Joo, H. N. Han, and M.-G. Lee. Numerical modeling of shear band effect on goss grain recrystallization in electrical steels: Crystal plasticity finite element and phase field modeling. *International Journal of Plasticity*, 180:104049, 2024.

[91] M. Montagnat, T. Chauve, F. Barou, A. Tommasi, B. Beausir, and C. Fressengeas. Analysis of dynamic recrystallization of ice from EBSD orientation mapping. *Frontiers in Earth Science*, 3:81, Dec. 2015.

[92] S. H. Nandam, R. Schwaiger, A. Kobler, C. Kübel, C. Wang, Y. Ivanisenko, and H. Hahn. Controlling shear band instability by nanoscale heterogeneities in metallic nanoglasses. *Journal of Materials Research*, 36(14):2903–2914, 2021.

[93] K. Ng and A. Ngan. Stochastic nature of plasticity of aluminum micro-pillars. *Acta Materialia*, 56(8):1712–1720, 2008.

[94] T. J. Nizolek, T. M. Pollock, and R. M. McMeeking. Kink band and shear band localization in anisotropic perfectly plastic solids. *Journal of the Mechanics and Physics of Solids*, 146:104183, 2021.

[95] D. Norfleet, D. Dimiduk, S. Polasik, M. Uchic, and M. Mills. Dislocation structures and their relationship to strength in deformed nickel microcrystals. *Acta Materialia*, 56(13):2988–3001, 2008.

[96] Y. Pan, H. Wu, X. Wang, Q. Sun, L. Xiao, X. Ding, J. Sun, and E. K. H. Salje. Rotatable precipitates change the scale-free to scale dependent statistics in compressed ti nano-pillars. *Sci. Rep.*, 9(1):3778, Mar. 2019.

[97] T. A. Parthasarathy, S. I. Rao, D. M. Dimiduk, M. D. Uchic, and D. R. Trinkle. Contribution to size effect of yield strength from the stochastics of dislocation source lengths in finite samples. *Scripta Materialia*, 56(4):313–316, 2007.

[98] J. Paux, L. Morin, and R. Brenner. A model of porous plastic single crystals based on fractal slip lines distribution. *Journal of the Mechanics and Physics of Solids*, 167:104948, 2022.

[99] J. Paux, L. Morin, R. Brenner, and D. Kondo. An approximate yield criterion for porous single crystals. *European Journal of Mechanics - A/Solids*, 51:1–10, 2015.

[100] D. Peirce, R. J. Asaro, and A. Needleman. Material rate dependence and localized deformation in crystalline solids. *Acta Metall.*, 31(12):1951–1976, Dec. 1983.

[101] V. Phalke, S. Forest, H.-J. Chang, and A. Roos. Adiabatic shear banding in fcc metallic single and poly-crystals using a micromorphic crystal plasticity approach. *Mechanics of Materials*, 169:104288, 2022.

[102] E. Renner, A. Bourceret, Y. Gaillard, F. Amiot, P. Delobelle, and F. Richard. Identifiability of single crystal plasticity parameters from residual topographies in berkovich nanoindentation on fcc nickel. *Journal of the Mechanics and Physics of Solids*, 138:103916, 2020.

[103] H. Resk, L. Delannay, M. Bernacki, T. Coupez, and R. Logé. Adaptive mesh refinement and automatic remeshing in crystal plasticity finite element simulations. *Modelling and Simulation in Materials Science and Engineering*, 17(7):075012, 2009.

[104] J. Rice. Inelastic constitutive relations for solids: An internal-variable theory and its application to metal plasticity. *Journal of the Mechanics and Physics of Solids*, 19(6):433–455, 1971.

[105] A. Rinaldi, P. Peralta, K. Sieradzki, E. Traversa, and S. Licoccia. Role of dislocation density on the sample-size effect in nanoscale plastic yielding. *Journal of Nanomechanics and Micromechanics*, 2(3):42–48, 2012.

[106] Q. Rizzardi, P. M. Derlet, and R. Maaß. Intermittent microplasticity in the presence of a complex microstructure. *Phys. Rev. Mater.*, 6:073602, Jul 2022.

[107] F. Roters, P. Eisenlohr, L. Hantcherli, D. D. Tjahjanto, T. R. Bieler, and D. Raabe. Overview of constitutive laws, kinematics, homogenization and multiscale methods in crystal plasticity finite-element modeling: Theory, experiments, applications. *Acta Mater.*, 58(4):1152–1211, Feb. 2010.

[108] A. M. Roy, R. Arróyave, and V. Sundararaghavan. Incorporating dynamic recrystallization into a crystal plasticity model for high-temperature deformation of ti-6al-4v. *Materials Science and Engineering: A*, 880:145211, 2023.

[109] O. U. Salman, R. Baggio, B. Bacroix, G. Zanzotto, N. Gorbushin, and L. Truskinovsky. Discontinuous yielding of pristine micro-crystals. *Comptes Rendus. Physique*, 22(S3):201–248, 2021.

[110] O. U. Salman and I. R. Ionescu. Tempering the mechanical response of FCC micro-pillars: An eulerian plasticity approach. *Mech. Res. Commun.*, 114(103665):103665, June 2021.

[111] R. Sartorti, W. Garhuom, and A. Düster. Remeshing and eigenvalue stabilization in the finite cell method for structures undergoing large elastoplastic deformations. *Archive of Applied Mechanics*, 94(9):2745–2768, 2024.

[112] J. Schwiedrzik, R. Raghavan, M. Rüggeberg, S. Hansen, J. Wehrs, R. B. Adusumalli, T. Zimmermann, and J. Michler. Identification of polymer matrix yield stress in the wood cell wall based on micropillar compression and micromechanical modelling. *Philosophical Magazine*, 96(32-34):3461–3478, 2016.

[113] K. Sedighiani, V. Shah, K. Traka, M. Diehl, F. Roters, J. Sietsma, and D. Raabe. Large-deformation crystal plasticity simulation of microstructure and microtexture evolution through adaptive remeshing. *International Journal of Plasticity*, 146:103078, 2021.

[114] K. Sedighiani, K. Traka, F. Roters, J. Sietsma, D. Raabe, and M. Diehl. Crystal plasticity simulation of in-grain microstructural evolution during large deformation of if-steel. *Acta Materialia*, 237:118167, 2022.

[115] K. Sedighiani, K. Traka, F. Roters, J. Sietsma, D. Raabe, and M. Diehl. Crystal plasticity simulation of in-grain microstructural evolution during large deformation of if-steel. *Acta Materialia*, 237:118167, 2022.

[116] J. C. Simo and T. J. Hughes. *Computational inelasticity*, volume 7. Springer Science & Business Media, 2006.

[117] J. Smiri, O. U. Salman, M. Ghidelli, and I. R. Ionescu. Accounting for localized deformation: a simple computation of true stress in micropillar compression experiments. *Experimental Mechanics*, pages 1–8, 2024.

[118] D. Song and P. Ponte Castañeda. A finite-strain homogenization model for viscoplastic porous single crystals: I – theory. *Journal of the Mechanics and Physics of Solids*, 107:560–579, 2017.

[119] A. Srivastava, B. Revil-Baudard, O. Cazacu, and A. Needleman. A model for creep of porous crystals with cubic symmetry. *International Journal of Solids and Structures*, 110-111:67–79, 2017.

[120] C. Sénac, J. Hure, and B. Tanguy. Yield surface for void growth and coalescence of porous anisotropic materials under axisymmetric loading. *Journal of the Mechanics and Physics of Solids*, 179:105365, 2023.

[121] G. I. Taylor. The mechanism of plastic deformation of crystals. part i.—theoretical. *Proceedings of the Royal Society of London. Series A, Containing Papers of a Mathematical and Physical Character*, 145(855):362–387, 1934.

[122] R. Temam. *Navier–Stokes Equations: Theory and Numerical Analysis*. North-Holland, Amsterdam, 1979.

[123] C. Teodosiu. *Elastic Models of Crystal Defects*. Springer Science & Business Media, June 2013.

[124] C. Teodosiu, J. Raphanel, and L. Tabourot. *Finite element simulation of the large elastoplastic deformation of multicrystals*. Proceedings of the international seminar MECAMAT'91, Fontainebleau, 08 1991.

[125] C. Teodosiu and F. Sidoroff. A theory of finite elastoviscoplasticity of single crystals. *International Journal of Engineering Science*, 14(2):165–176, 1976.

[126] M. D. Uchic, D. M. Dimiduk, J. N. Florando, and W. D. Nix. Sample dimensions influence strength and crystal plasticity. *Science*, 305(5686):986–989, 2004.

[127] J. Wang, Y. Hu, P. Guan, K. Song, L. Wang, G. Wang, Y. Pan, B. Sarac, and J. Eckert. Hardening of shear band in metallic glass. *Scientific Reports*, 7, 08 2017.

[128] Z.-J. Wang, Z.-W. Shan, J. Li, J. Sun, and E. Ma. Pristine-to-pristine regime of plastic deformation in submicron-sized single crystal gold particles. *Acta Materialia*, 60(3):1368–1377, Feb. 2012.

[129] J. Weiss, P. Zhang, O. U. Salman, G. Liu, and L. Truskinovsky. Fluctuations in crystalline plasticity. *Comptes Rendus. Physique*, 22(S3):1–37, 2021.

[130] A. H. Wilson and R. Smoluchowski. The theory of metals. *Am. J. Phys.*, Jan. 1953.

[131] G. Wu, C. Liu, A. Brognara, M. Ghidelli, Y. Bao, S. Liu, X. Wu, W. Xia, H. Zhao, J. Rao, D. Ponge, V. Devulapalli, W. Lu, G. Dehm, D. Raabe, and Z. Li. Symbiotic crystal-glass alloys via dynamic chemical partitioning. *Materials Today*, 51:6–14, 2021.

[132] I. Yasnikov, Y. Kaneko, M. Uchida, and A. Vinogradov. The grain size effect on strain hardening and necking instability revisited from the dislocation density evolution approach. *Materials Science and Engineering: A*, 831:142330, 2022.

[133] C. Ye, G. Liu, K. Chen, J. Liu, J. Hu, Y. Yu, Y. Mao, and Y. Shen. Unified crystal plasticity model for fcc metals: From quasistatic to shock loading. *Phys. Rev. B Condens. Matter*, 107(2):024105, Jan. 2023.

[134] M. Zecevic, R. A. Lebensohn, and L. Capolungo. New large-strain fft-based formulation and its application to model strain localization in nano-metallic laminates and other strongly anisotropic crystalline materials. *Mechanics of Materials*, 166:104208, 2022.

[135] J. Zhang, K. Kishida, and H. Inui. Specimen size and shape dependent yield strength in micropillar compression deformation of mo single crystals. *International Journal of Plasticity*, 03 2017.

[136] P. Zhang, O. U. Salman, J. Weiss, and L. Truskinovsky. Variety of scaling behaviors in nanocrystalline plasticity. *Phys. Rev. E*, 102:023006, Aug 2020.

[137] P. Zhang, O. U. Salman, J.-Y. Zhang, G. Liu, J. Weiss, L. Truskinovsky, and J. Sun. Taming intermittent plasticity at small scales. *Acta Materialia*, Oct. 2016.

[138] Y. Zhang, N. Li, M. Schneider, T. Nizolek, L. Capolungo, and R. McCabe. Kink mechanism in cu/nb nanolaminates explored by in situ pillar compression. *Acta Materialia*, 237, 07 2022.

[139] C. Zheng, H. Wang, Y. Jiang, and G. Li. On the yield criterion of porous materials by the homogenization approach and steigmann–ogden surface model. *Scientific Reports*, 13(1):10951, 2023.

Chapter 8

Appendix

8.1 Numerical scheme used for the simulations

The main goal of this section is to recall the Eulerian numerical strategy proposed in [15] for the rigid-visco-plastic crystal model used in this thesis.

Use of a time implicit (backward) Euler scheme for time discretization gives a set of nonlinear equations for the velocities $\boldsymbol{v}$ and lattice orientation $\boldsymbol{R}$ (or θ for the simplified model). At each iteration in time, an iterative algorithm is developed to solve these nonlinear equations. Specifically, a mixed finite-element and Galerkin discontinuous strategy is proposed. The variational formulation for the velocity field is discretized using the finite element method, while a Galerkin discontinuouse method with an upwind choice of the flux is adopted for solving the hyperbolic equations that describe the evolution of the lattice orientation. It is to be noted that in the case of the rigid-viscoplastic model studied in this thesis, additional difficulties arise from the non-differentiability of the plastic terms. That means that we cannot simply make use of the finite element techniques developed for Navier-Stokes fluids (see for instance [39, 122]). To overcome these difficulties the iterative decomposition-coordination formulation coupled with the augmented Lagrangian method (introduced in [40, 32]) was modified. The reason for this modification is that, in the crystal model there is non co-axiality between the stress deviator and the rate of deformation in contrast with the von-Mises model for which the original method was proposed (see [40, 32]). This type of algorithm permits also to solve alternatively, at each iteration, the equations for the velocity field and for the unit vectors that define the lattice orientation.

For vanishing viscosity, the adopted visco-plastic model contains as a limit case

the inviscid Schmid law. Even that Schmid model is very stiff, for small viscosities (as for metals) and moderate strain rates the iterative decomposition coordination formulation coupled with the augmented Lagrangian method works very well and no instabilities are presents. However, for small viscosities and large velocities (more then 100m/s) with large Reynolds numbers (Re > 1000) the above algorithm is converging very slowly. In this last case, other techniques, coming from gas dynamics, have to be included.

To include frictional effects in the algorithm, we first regularize the friction law (2.44). This can be done (see also [59, 60]) by introducing a small frictional viscosity in the Coulomb friction law and writing (2.44) as

$$
\boldsymbol{v}_{rT} = -\frac{1}{\eta_f} \left[1 - \frac{\mu_f [-\sigma_n]_+}{|\boldsymbol{\sigma}_T|} \right]_+ \boldsymbol{\sigma}_T. \tag{8.1}
$$

Note that using this regularization, the friction law has the same mathematical structure as the viscoplastic constitutive equation and we can use the same iterative decomposition-coordination formulation.

If the Eulerian domain $\mathcal{D}$ has time variations then the above algorithm has been adapted to an ALE (Arbitrary Eulerian-Lagrangian) description of the crystal evolution. In this case is more convenient to have the same finite element Galerkin discontinous meshes. This avoid the interpolation of the lattice orientation on the deformed mesh. As a matter of fact, the numerical algorithm proposed here deals only with a Stokes-type problem at each time step and the implementation of the Navier-Stokes equations in an ALE formulation is rather standard (see for instance [54, 84, 83, 28]).

For the sake of simplicity we shall present here the numerical scheme for the simplified $N = 3$ slips systems in 2D, described in Section 2.7.

8.1.1   Time discretization

Having in mind the initial and boundary value problem, stated in Section BVP, let Δt be the time step and let us denote by $\boldsymbol{v}^k$, $\boldsymbol{\sigma}^k$, p^k, θ^k and ρ_s^k the values of the unknowns $\boldsymbol{v}(k\Delta t)$, $\boldsymbol{\sigma}(k\Delta t)$, $p(k\Delta t)$, $\theta(k\Delta t)$ and $\rho^s(k\Delta t)$. Suppose that we have computed all these variables at time $t = (k-1)\Delta t$. Let also denote by $\mathbf{V}^k = \mathbf{V}(k\Delta t), \mathbf{S}^k = \mathbf{S}(k\Delta t), \theta_{in}^k = \theta_{in}(k\Delta t), \rho_{in}^{sk} = \rho_{in}^s(k\Delta t)$ the boundary conditions at $t = k\Delta t$.

The time implicit (backward) Euler scheme for the field equations of the initial and boundary value problem gives the following nonlinear equations for $\boldsymbol{v}^k$, $\boldsymbol{\sigma}^k$, θ_s^k and ρ^{sk}

$$\rho^{mass}\frac{\boldsymbol{v}^k - \boldsymbol{v}^{k-1}}{\Delta t} + \boldsymbol{v}^k \cdot \boldsymbol{\nabla}\boldsymbol{v}^k - \mathbf{div}\,\boldsymbol{\sigma}'^k + \nabla p^k = \rho\boldsymbol{f} \quad \text{in } \mathcal{D}, \tag{8.2}$$

$$\mathrm{div}(\boldsymbol{v}^k) = 0 \quad \text{in } \mathcal{D}, \tag{8.3}$$

$$\boldsymbol{D}(\boldsymbol{v}^k) = \sum_{s=1}^N \dot{\gamma}_s^k \boldsymbol{M}_s^k, \qquad \dot{\gamma}_s^k = \frac{1}{\eta_s}\left[1 - \frac{\tau_0^{sk}}{\left|\boldsymbol{\sigma}^k : \boldsymbol{M}_s^k\right|}\right]_+ \left(\boldsymbol{\sigma}^k : \boldsymbol{M}_s^k\right), \tag{8.4}$$

$$\frac{\theta^k - \theta^{k-1}}{\Delta t} + \boldsymbol{v}^k \cdot \boldsymbol{\nabla}\theta^k = \frac{1}{2}\left(\sum_{s=1}^N \dot{\gamma}_s^k - (\frac{\partial v_1^k}{\partial x_2} - \frac{\partial v_2^k}{\partial x_1})\right), \tag{8.5}$$

$$\frac{\rho_s^k - \rho_s^{k-1}}{\Delta t} + \boldsymbol{v}^k \cdot \boldsymbol{\nabla}\rho_s^k = \frac{1}{b}\left(\mathcal{M}^s(\boldsymbol{\rho}^k) - \mathcal{A}^s(\boldsymbol{\rho}^k)\right)|\dot{\gamma}_s^k|, \tag{8.6}$$

$$\boldsymbol{\tau}_0^k = \boldsymbol{\mathcal{T}}_0(\boldsymbol{\rho}^k). \tag{8.7}$$

while the boundary conditions read

$$\boldsymbol{v}^k = \mathbf{V}^k \text{ on } \Gamma_v, \quad \boldsymbol{\sigma}^k\boldsymbol{n} = \mathbf{S}^k \text{ on } \Gamma_s, \quad \theta_s^k = \theta_{in}^k, \quad \rho_s^k = \rho_{in}^{sk} \quad \text{on } \partial_{in}\mathcal{D}. \tag{8.8}$$

If we deal with bilateral frictional contact on a part of the boundary, denoted Γ_c, with a rigid body which has the velocity $\boldsymbol{V}^g$ then the boundary conditions (8.1) read

$$\boldsymbol{v}_r^k \cdot \boldsymbol{n} = 0, \quad \boldsymbol{v}_{rT}^k = -\frac{1}{\eta_f}\left[1 - \frac{\mu_f[-\sigma_n^k]_+}{\left|\boldsymbol{\sigma}_T^k\right|}\right]_+ \boldsymbol{\sigma}_T^k, \quad \text{on} \quad \Gamma_c. \tag{8.9}$$

where we have denoted by $\boldsymbol{v}_r^k = \boldsymbol{v}^k - \boldsymbol{V}^g(k\Delta t)$ the relative velocity, by $\sigma_n^k = \boldsymbol{\sigma}^k\boldsymbol{n} \cdot \boldsymbol{n}$ the normal stress, by $\boldsymbol{v}_{rT}^k = \boldsymbol{v}_r^k - (\boldsymbol{v}_r^k \cdot \boldsymbol{n})\boldsymbol{n}$ the tangential relative velocity and by $\boldsymbol{\sigma}_T^k = \boldsymbol{\sigma}^k\boldsymbol{n} - \sigma_n^k\boldsymbol{n}$ the tangential stress.

8.1.2   The algorithm at each time step

Let us fix the iteration in time, k. An iterative decomposition-coordination formulation coupled with the augmented method (see [40, 32]) will be adapted here for the crystal plasticty model. This type of algorithm permits to solve alternatively, at each iteration n, equations (8.2-8.4) for the velocity field and (8.5)-(8.6) for the latice orientation and dislocation densities. The convergence is achieved when the difference between $\boldsymbol{v}^{k,n}, \boldsymbol{\sigma}^{k,n}, \theta_s^{k,n}, \rho_s^{k,n}$ and $\boldsymbol{v}^{k,n-1}, \boldsymbol{\sigma}^{k,n-1}, \theta_s^{k,n-1}, \rho_s^{k,n-1}$ is small enough.

In order to describe the algorithm let $r > 0$ be the augmented Lagrangian step

and let $\mathcal{D}$ be discretized by using a family of triangulations $(\mathcal{T}_h)_h$ made of finite elements (here $h > 0$ is the discretization parameter representing the greatest diameter of a triangle in $\mathcal{T}_h$). We denote by V_h the FE space for the velocity field $\boldsymbol{v}^k$, by W_h the FE space for the pressures field p and by Q_h the Galerkin discontinous space for the stresses deviators $\boldsymbol{\sigma}'$, for lattice orientations θ and dislocation densities ρ_s).

We put $\boldsymbol{v}^{k,0} = \boldsymbol{v}^{k-1}, \boldsymbol{\sigma}'^{k,0} =: \boldsymbol{\sigma}'^{k-1}, \theta_s^{k,0} = \theta_s^{k-1}, \rho_s^{k,0} = \rho_s^{k-1}, \dot{\delta}_s^{k,0} = \dot{\gamma}_s^{k-1}$ and we suppose that $\boldsymbol{v}^{k,n-1}, \boldsymbol{\sigma}'^{k,n-1}$ and $\theta_s^{k,n-1}, \rho_s^{k,n-1}, \dot{\delta}_s^{k,n-1}$ are known.

Step 1.) The first step consists in solving the following linear equation of Stokes type for the velocity field $\boldsymbol{v}^{k,n}$ and the pressure $p^{k,n}$:

$$\rho^{mass} \left(\frac{\boldsymbol{v}^{k,n} - \boldsymbol{v}^{k-1}}{\Delta t} + \boldsymbol{v}^{k,n-1} \cdot \nabla \boldsymbol{v}^{k,n-1} \right) - \mathbf{div}\left(r\boldsymbol{D}(\boldsymbol{v}^{k,n}) \right) + \nabla p^{k,n} =$$
$$\mathbf{div}\,\tilde{\boldsymbol{\sigma}}^{k,n-1} + \rho^{mass}\boldsymbol{f}, \qquad \mathrm{div}(\boldsymbol{v}^{k,n}) = 0, \quad (8.10)$$

with the boundary conditions

$$\boldsymbol{v}^{kn} = \mathbf{V}^k \text{ on } \Gamma_v, \quad \left(r\boldsymbol{D}(\boldsymbol{v}^{k,n}) - p^{k,n}\boldsymbol{I} + \tilde{\boldsymbol{\sigma}}^{k,n-1} \right) \boldsymbol{n} = \mathbf{S}^k \quad \text{on} \quad \Gamma_s.$$

where we have denoted by

$$\tilde{\boldsymbol{\sigma}}^{k,n-1} = \boldsymbol{\sigma}'^{k,n-1} - r \sum_{s=1}^{N} \dot{\delta}_s^{k,n-1} \boldsymbol{M}_s^{k,n-1}.$$

The above problem is a standard one in fluid mechanics and there exists many technics to solve it. In all the computations presented in this thesis, we have used a Lagrangian formulation with a [continuous P2, continuous P1] choice for finite element spaces (V_h, W_h) associated to the velocities and pressures.

If we deal with the bilateral friction then we have to add the boundary conditions

$$\boldsymbol{v}^{k,n} \cdot \boldsymbol{n} = 0, \quad \left(r\boldsymbol{D}(\boldsymbol{v}^{k,n}) + \tilde{\boldsymbol{\sigma}}^{k,n-1} \right)_T = -r_f \boldsymbol{v}_{rT}^{k,n} + r_f \alpha^{k,n-1} + \boldsymbol{\sigma}_T^{k,n-1}, \quad \text{on} \quad \Gamma_c,$$

where $\alpha^{k,n-1}$ are the Lagrange multipliers for the tangential relative velocity and $r_f > 0$ is the frictional augmented Lagrangian step.

Step 2.) The second step consists in finding the decomposition of the global rate of deformation $\boldsymbol{D}(\boldsymbol{v}^{k,n})$, into the slip rates $\dot{\gamma}_s^{k,n} \in Q_h$, according to (8.4). This

can be done using the analytic formula (2.37) which provide directly the slip rates $\dot{\gamma}_s^{k,n}$ from the expression of $\boldsymbol{D}(\boldsymbol{v}^{k,n})$ and of the yield limit $\tau_0^{sk,n-1}$.

Note that the finite element spaces for the velocity fields $\boldsymbol{v}^{k,n}$ and that for the slip rates $\dot{\gamma}_s^{k,n}$ cannot be chosen independently. For instance if $V_h = $ [continuous P2] then we have to choose $Q_h =$ [discontinuous P1]. This is the choice in all simulations presented in this thesis.

Step 3.) We introduce now the slip rate multipliers $\dot{\delta}_s^{k,n} : \mathcal{D} \to \mathbb{R}$, belonging to Q_h, computed according to the decomposition-coordination formulation coupled with the augmented method for each slip system:

$$\dot{\delta}_s^{k,n} = \frac{1}{\eta_s + r} \left[1 - \frac{\tau_0^{sk,n-1}}{|\boldsymbol{\sigma}^{k,n-1} : \boldsymbol{M}_s^{k,n-1} + r\dot{\gamma}_s^{k,n}|} \right]_+ (\boldsymbol{\sigma}^{k,n-1} : \boldsymbol{M}_s^{k,n-1} + r\dot{\gamma}_s^{k,n}). \quad (8.11)$$

Then the deviator stress field is updated:

$$\boldsymbol{\sigma}'^{k,n} = \boldsymbol{\sigma}'^{k,n-1} + r \left(\boldsymbol{D}(\boldsymbol{v}^{k,n}) - \sum_{s=1}^N \dot{\delta}_s^{k,n} \boldsymbol{M}_s^{k,n-1} \right). \quad (8.12)$$

If we deal with the bilateral friction then we have to add

$$\alpha^{k,n} = -\frac{1}{\eta_f + r_f} \left[1 - \frac{\mu_f[-\sigma_n^{k,n-1}]_+}{|\boldsymbol{\sigma}_T^{k,n-1} - r_f \boldsymbol{v}_{rT}^{k,n}|} \right]_+ (\boldsymbol{\sigma}_T^{k,n-1} - r_f \boldsymbol{v}_{rT}^{k,n}), \quad (8.13)$$

and then to update $\boldsymbol{\sigma}_T^{k,n}$ as

$$\boldsymbol{\sigma}_T^{k,n} = \boldsymbol{\sigma}_T^{k,n-1} - r_f(\boldsymbol{v}_{rT}^{k,n} - \alpha^{k,n}).$$

Step 4.) In this step, we compute the latice orientation from the linear hyperbolic equation for $\theta^{k,n}$

$$\frac{\theta^{k,n} - \theta^{k-1}}{\Delta t} + \boldsymbol{v}^{k,n} \cdot \boldsymbol{\nabla}\theta^{k,n} = \frac{1}{2} \left(\sum_{s=1}^N \dot{\gamma}_s^{k,n} - (\frac{\partial v_1^{k,,n}}{\partial x_2} - \frac{\partial v_2^{kn}}{\partial x_1}) \right), \quad (8.14)$$

whith the boundary conditions

$$\theta^{k,n} = \theta_{in}^k, \quad \text{on } \partial_{in}\mathcal{D}.$$

After that we compute the dislocation densities from the linear hyperbolic equation for $\rho_s^{k,n}$:

$$\frac{\rho_s^{k,n} - \rho_s^{k-1}}{\Delta t} + \boldsymbol{v}^{k,n} \cdot \boldsymbol{\nabla} \rho_s^{k,n} = \frac{1}{b} \left(\mathcal{M}^s(\boldsymbol{\rho}^{k,n-1}) - \mathcal{A}^s(\boldsymbol{\rho}^{k,n-1}) \right) |\dot{\gamma}_s^{k,n}|, \qquad (8.15)$$

with the boundary conditions

$$\rho_s^{k,n} = \rho_{in}^{sk} \quad \text{on } \partial_{in}\mathcal{D}.$$

To solve the linear systems (8.14) and (8.15) we have adopted here a Galerkin discontinous strategy with an "upwind" choice of the flux. In the numerical applications presented in this paper we have chosen the finite volume mesh to be the finite element triangulation $\mathcal{T}_h$, and the finite volume space to be Q_h=[discontinous P1].

Finally we update the yield limits $\tau_c^{k,n}$, $s = 1, ... N$ though

$$\boldsymbol{\tau}_c^{k,n} = \boldsymbol{\mathcal{T}}_c(\boldsymbol{\rho}^{k,n}). \qquad (8.16)$$

8.1.3   The algorithm in an ALE method

If the domain $\mathcal{D}$ occupied by the single crystal (or poly-crystals) varies in time, then an arbitrary Eulerian-Lagrangean (ALE) description was adopted. We want to point out here how the above algorithm have to be changed if it is used coupled with an ALE method. For that we have to have in mind that the passage from time iteration $k-1$ to k involves the frame velocity $\boldsymbol{v}_{fr}^{k-1}$. Since in the ALE formulation $\boldsymbol{v}_{fr}^{k-1} \cdot \boldsymbol{n} = \boldsymbol{v}^{k-1} \cdot \boldsymbol{n}$ the income boundary $\partial_{in}\mathcal{D}(t)$ is always empty. There are only three equations from the above algorithm which have to be changed: equation (8.10) with

$$\rho^{mass} \left(\frac{\boldsymbol{v}^{k,n} - \boldsymbol{v}^{k-1}}{\Delta t} + (\boldsymbol{v}^{k,n-1} - \boldsymbol{v}_{fr}^{k-1}) \cdot \nabla \boldsymbol{v}^{k,n-1} \right) - \mathbf{div} \left(r \boldsymbol{D}(\boldsymbol{v}^{k,n}) \right) + \nabla p^{k,n} =$$
$$\mathbf{div}\, \tilde{\boldsymbol{\sigma}}^{k,n-1} + \rho^{mass} \boldsymbol{f}, \quad \text{div}(\boldsymbol{v}^{k,n}) = 0 \quad (8.17)$$

equation (8.14) with

$$\frac{\theta^{k,n} - \theta^{k-1}}{\Delta t} + (\boldsymbol{v}^{k,n} - \boldsymbol{v}_{fr}^{k-1}) \cdot \boldsymbol{\nabla} \theta^{k,n} = \frac{1}{2} \left(\sum_{s=1}^{N} \dot{\gamma}_s^{kn} - (\frac{\partial v_1^{k,n}}{\partial x_2} - \frac{\partial v_2^{k,n}}{\partial x_1}) \right), \quad (8.18)$$

and equation (8.15) with

$$\frac{\rho_s^{k,n} - \rho_s^{k-1}}{\Delta t} + (\boldsymbol{v}^{k,n} - \boldsymbol{v}_{fr}^{k-1}) \cdot \boldsymbol{\nabla} \rho_s^{k,n} = \frac{1}{b} \left(\mathcal{M}^s(\boldsymbol{\rho}^{k,n-1}) - \mathcal{A}^s(\boldsymbol{\rho}^{k,n-1}) \right) |\dot{\gamma}_s^{k,n}|. \quad (8.19)$$

8.2   Remeshing procedure

The quality of the simulation results in mesh based approaches very much depends upon the characteristics of the mesh. A poor mesh quality impacts the computational efficiency, increases the computational time and may lead to unstable solutions[49]. Meshing can be either uniform or non-uniform. Adaptive meshing is a type of non-uniform mesh scheme widely used in FEM based approaches see [113]. It is characterized by a mesh density that varies across different regions. We employ a remeshing technique to address mesh distortion issues in crystal plasticity simulations. This method involves replacing distorted meshes with new, undistorted ones [111]. The variables from the deformed configuration are transferred to the new mesh using a nearest-neighbor mapping algorithm. The simulation is then restarted with the initial state set based on the most recent deformation state. During large deformations, the aspect ratio of the elements—defined as the ratio between element size in the stretching versus compression directions—can become excessively large. This can introduce errors and hinder strain localization. To mitigate this, a multi-step mesh refinement strategy is applied at each remeshing stage, adjusting the mesh density as the deformation progresses. The key idea is to maintain a constant number of elements in the compression direction while increasing the number of elements in the stretching direction to preserve a near-cubic element shape. This gradual mesh refinement enhances simulation resolution during deformation while minimizing information loss and avoiding a significant increase in computational points (cost) see [103].

In our adaptive meshing approach for monocrystal and polycrystal simulations, we apply three combined criteria: strain gradient, orientation gradient, and accumulative plastic strain.

- Strain Gradient Criterion: The strain gradient serves as a crucial indicator of regions experiencing significant deformation. Areas with steep strain gradients often correspond to locations of localized plasticity, such as near grain boundaries or in regions undergoing shear band formation. By refining the mesh in

these high-gradient areas, we ensure that the simulation can accurately model the material's response to applied loads and capture critical features of the deformation process.

- Orientation Gradient Criterion: The orientation gradient is equally important in polycrystal simulations, as it reflects the variation in crystallographic orientation across the material. Changes in orientation can significantly influence mechanical behavior, particularly in materials exhibiting anisotropic properties. By monitoring the orientation gradient, we can identify regions where the crystal orientations change rapidly, necessitating a finer mesh to resolve the interactions between grains and accurately capture the evolution of microstructural features.

- Accumulative Plastic Strain Criterion: This additional criterion targets areas of high plastic strain to minimize mesh distortion during ongoing deformation. Finer meshing in these zones helps maintain element integrity, reduce numerical artifacts, and enhance stability.

Combining these criteria allows for a more nuanced adaptive meshing strategy. In regions where both the strain and orientation gradients are high, the mesh density is significantly increased, ensuring precise resolution of complex interactions and behaviors. Conversely, in areas where both gradients are low, the mesh can be coarsened to optimize computational efficiency without sacrificing accuracy.

These criteria adaptive meshing approach not only enhances the fidelity of our simulations but also minimizes computational costs by focusing resources where they are most needed. As the simulation progresses, the mesh dynamically adapts to the evolving deformation field and microstructural characteristics, resulting in improved simulation accuracy for crystalline materials under large deformations.

While this multi-criteria strategy generally captures complex deformation behaviors in polycrystalline materials and improves accuracy, using all three criteria simultaneously is not always necessary or efficient. For instance, when orientation gradients are weak, a dual-criterion approach using strain gradient and accumulative plastic strain may suffice. Additionally, when strain gradient and accumulative plastic strain are both significant within the same region, the strain gradient criterion alone may be used to capture the essential deformation characteristics.

To illustrate the effectiveness of our adaptive meshing strategy, mesh refinement patterns derived from various simulations discussed in the preceding chapters (3, 4, 5,

6) are presented. The figures illustrate the adaptive meshing process across different simulations of single- and polycrystal structures under various loading conditions and strain levels. Each figure demonstrates how the mesh adjusts to capture deformation characteristics specific to the crystal type, initial orientation, and applied strain. Key observations are as follows :

Polycrystal in Channel Compression, Chapter 3

In Figure 8.1, adaptive meshing for the polycrystal under channel compression considers both orientation and deformation gradients, especially near grain boundaries. The mesh dynamically refines around these boundaries to capture variations in lattice orientation and strain localization accurately.

FCC Ni Monocrystal under Compression, Chapter 4

Figure 8.2 Depicts meshing evolution for an FCC Ni monocrystal in micropillar compression. The mesh adapts to capture detailed strain localization as engineering strain rises.

Circular Void in Monocrystal under Radial Loading, Chapter 3 and 5

Mesh adaptation is used for a monocrystal with a circular void under radial loading computations, the computation are illustrated in Chapters 3 and 5. The difference between computation in the two chapters is the initial radius of cavity in computation of chapter 3 is 3 times higher than the computation of chapter 5.

In Figure 8.3, coresponding to chapter 3, initial mesh refinement focuses on regions with high deformation gradients. As deformation advances, the orientation gradient criterion activates, creating a dual-criterion adaptive meshing approach that considers both deformation and orientation gradients. The refinement pattern associated with the orientation gradient is especially prominent where orientation shows discontinuities at angles $\varphi = \pi/6 + k\pi/3$, particularly around the void, where deformations are highest, compared to areas closer to the outer boundary.

In Figure 8.4 which corespond to chapter 5, the mesh begins with a dense refinement around the void, forming two overlapping star-like structures: one defined by kink bands and the other by slip bands. As deformation progresses, the kink-band structure gradually diminishes, leaving only the star pattern formed by shear bands. This evolution in mesh refinement effectively captures the localized deformation and the transition in dominant band structures surrounding the void.

FCC Porous Micropillar under Tension with Varying initial Orientations, Chapter 5

Figures 8.5 - 8.7 : Illustrate meshing in an FCC porous micropillar under tensile

loading with different crystallographic orientations ($\theta_0 = 0°$, $\theta_0 = \frac{54.7°}{2}$, and $\theta_0 = 65°$). Each orientation exhibits unique deformation responses, with mesh adaptation reflecting evolving strain distribution at each strain level.

8.3   Elastic perfectly plastic Eulerian model

We describe here the model used for the computations in Section 6.3. The movement (flow) in the Eulerian description is given by the velocity field, denoted $\boldsymbol{v}(t, \cdot)$: $\mathcal{D}_t \to R^d$ (here $\mathcal{D}_t$ is the Eulerian domain occupied by the elasto-plastic body at time t). The rate of deformation and the spin rate are denoted by $\boldsymbol{D} = \boldsymbol{D}(\boldsymbol{v}) = (\nabla\boldsymbol{v} + \nabla^T\boldsymbol{v})/2$ and by $\boldsymbol{W} = \boldsymbol{W}(\boldsymbol{v}) = (\nabla\boldsymbol{v} - \nabla^T\boldsymbol{v})/2$, respectively while the Cauchy stress tensor is $\boldsymbol{\sigma}(t, \cdot) : \mathcal{D}_t \to R_S^{d \times d}$. To describe the elasto-plastic model we consider the additive decomposition of the rate deformation tensor into the elastic $\boldsymbol{D}^e$ and plastic rates $\boldsymbol{D}^p$ of deformation

$$\boldsymbol{D} = \boldsymbol{D}^e + \boldsymbol{D}^p.$$

For the elastic range we considered the generalization of Hooke's law written in terms of the Jaumann rate of the Cauchy stress tensor $\boldsymbol{\sigma}^\nabla = \dot{\boldsymbol{\sigma}} - \boldsymbol{W}\boldsymbol{\sigma} - \boldsymbol{\sigma}\boldsymbol{W}$ (here $\dot{\boldsymbol{\sigma}} = \partial_t\boldsymbol{\sigma} + \boldsymbol{v} \cdot \nabla\boldsymbol{\sigma}$ is the total derivative) given by

$$\boldsymbol{\sigma}^\nabla(t) = \lambda \text{trace}(\boldsymbol{D}^e)\boldsymbol{I} + 2\mu\boldsymbol{D}^e, \quad \text{in } \boldsymbol{D}_t,$$

where λ, μ are the Lamé elastic coefficients. The plastic rate of deformation is related to the Cauchy stress tensor through the flow rule associated to the classical Von-Mises yield criterion with no hardening (perfectly plastic material). To be more precise, let $\mathcal{F}(\boldsymbol{\sigma}) = \sigma_{eq} - \sigma_Y$ be the yield function, with σ_Y the yield limit and $\sigma_{eq} = \sqrt{\frac{3}{2}}|\boldsymbol{\sigma}'|$ the Von-Mises stress ($\boldsymbol{\sigma}' = \boldsymbol{\sigma} - \frac{1}{3}\text{trace}(\boldsymbol{\sigma})\boldsymbol{I}$ is the stress deviator). If we denote the accumulated plastic strain by ε^p (given through the differential equation $\dot{\varepsilon}^p = \sqrt{\frac{3}{2}}|\boldsymbol{D}^p|$), then the flow rule and the loading-unloading conditions read

$$\boldsymbol{D}^p = \frac{\dot{\varepsilon}^p}{\sigma_{eq}}\boldsymbol{\sigma}', \quad \dot{\varepsilon}^p \geq 0, \quad \mathcal{F}(\boldsymbol{\sigma}) \leq 0, \quad \dot{\varepsilon}^p\mathcal{F}(\boldsymbol{\sigma}) = 0.$$
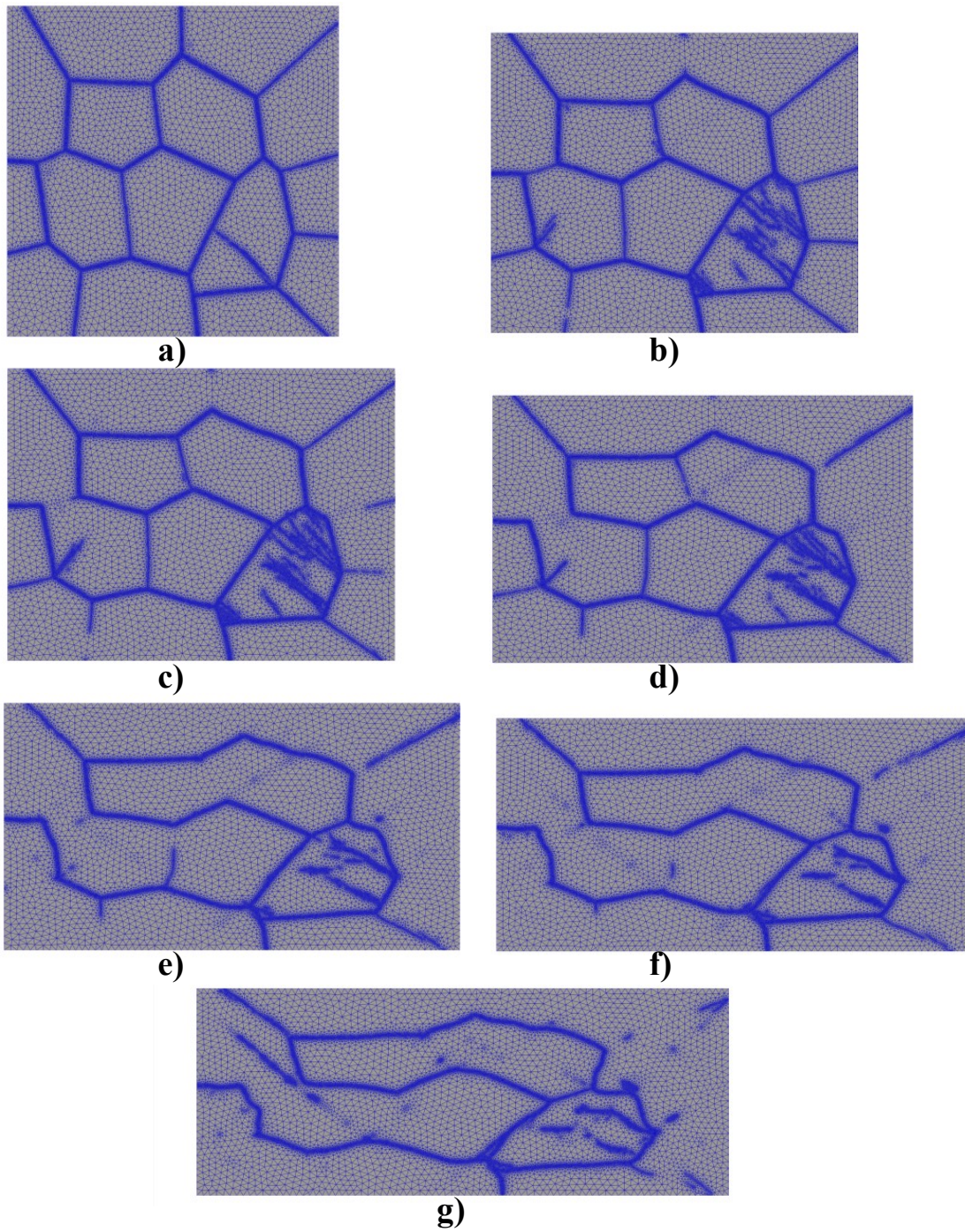
Figure 8.1: Adaptive meshing evolution for a HPC poly-crystal under a homogeneous gradient velocity loading (channel compression), see Chapter 3. The distributions correspond to $t = T/20$ ($\epsilon^{eng} = 0.025$), $t = T/4$ ($\epsilon^{eng} = 0.125$), $t = T/3$ ($\epsilon^{eng} = 0.166$), $t = T/2$ ($\epsilon^{eng} = 0.25$), $t = 2T/3$ ($\epsilon^{eng} = 0.33$) and $t = T$ ($\epsilon^{eng} = 0.5$).
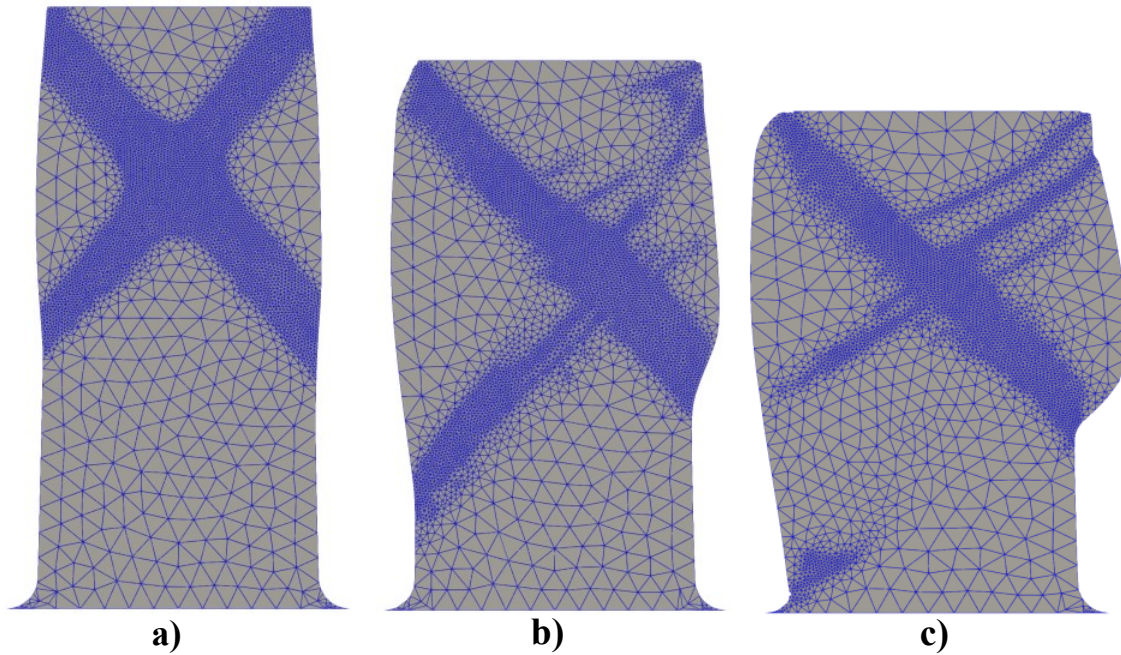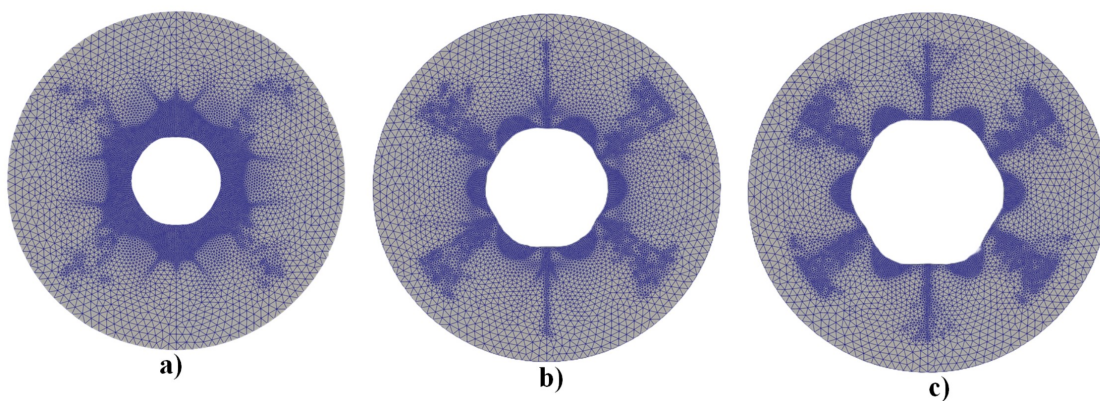
Figure 8.2: Adaptive meshing evolution in FCC Ni monocrystal micropillar compression simulation, see Chapter 4. The distributions correspond to (a) $t = T/5$ ($\epsilon^{eng} = 0.04$), (b)$t = 3T/5$ ($\epsilon^{eng} = 0.12$) and (c) $t = T$ ($\epsilon^{eng} = 0.2$).

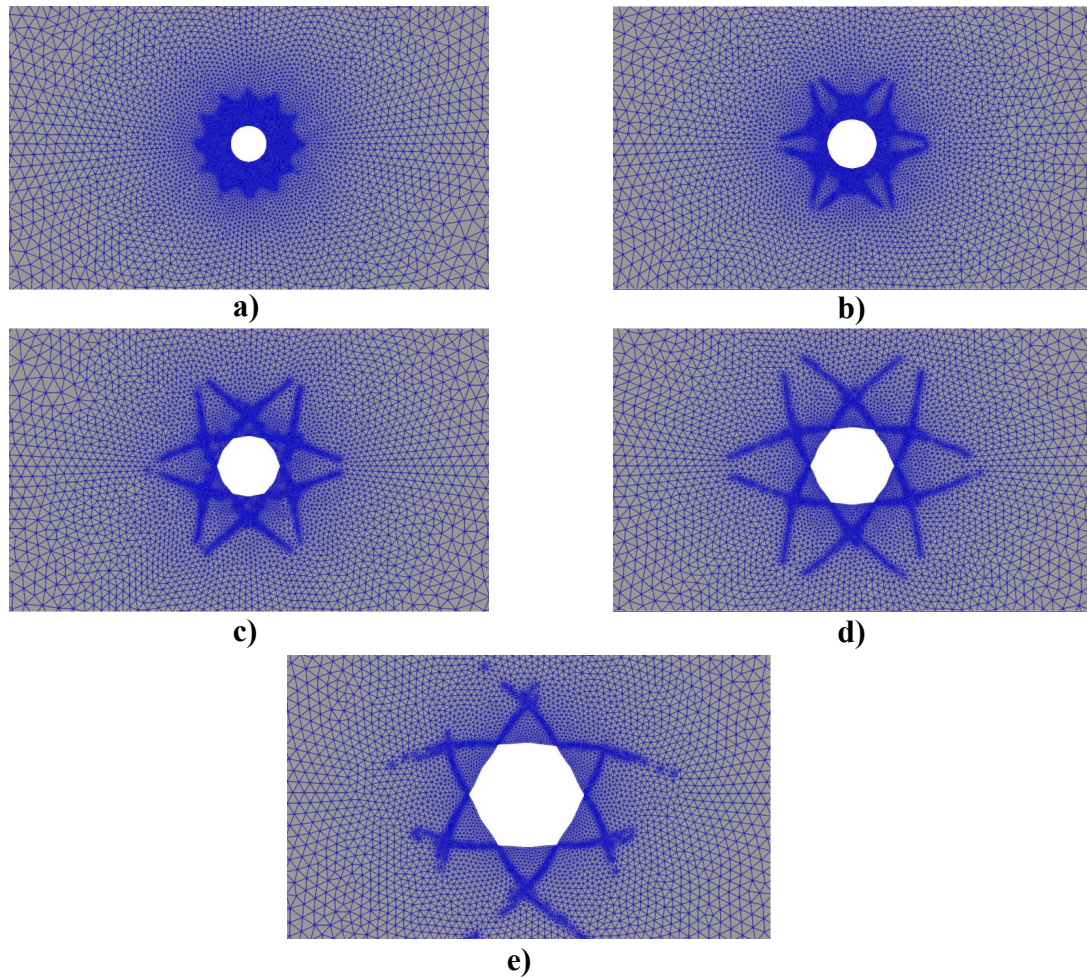Figure 8.3: Single-crystal with a circular void at its center under a radial velocity loading, see Chapter 3. The mesh distributions correspond to (a) $t = T/3$ ($\epsilon^{eng} = 0.0625$), (b) $t = 2T/3$ ($\epsilon^{eng} = 0.125$) and (c) $t = T$ ($\epsilon^{eng} = 0.1875$).

Figure 8.4: Adaptive meshing evolution for a disc unit cell with a single circular void at its center (monocrystal HPC) under radial loading simulations, see Chapter 5. The mesh distributions correspond to (a) $t = T/80$ ($\epsilon^{eng} = 0.0165\%$), (b) $t = T/10$ ($\epsilon^{eng} = 0.132\%$), (c) $t = T/5$ ($\epsilon^{eng} = 0.264\%$), $t = 2T/5$ ($\epsilon^{eng} = 0.528\%$) and (d) $t = 4T/5$ ($\epsilon^{eng} = 1.056\%$).
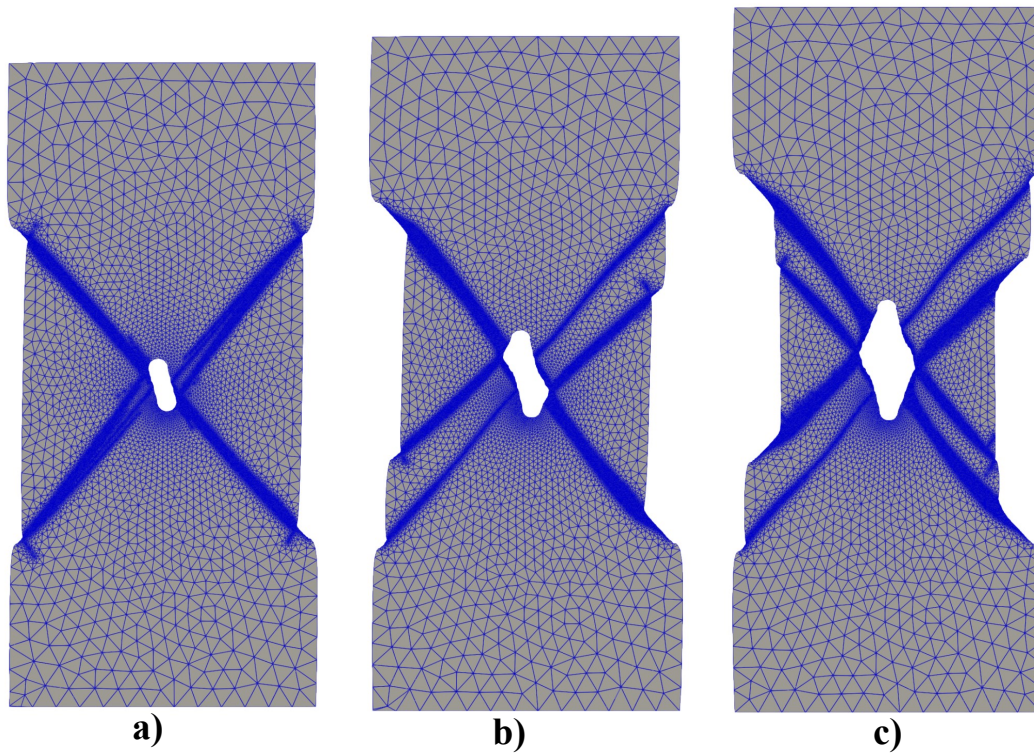
Figure 8.5: Adaptive meshing evolution of a FCC porous micropillar under tensile loading, see Chapter 5 with initial crystallographic orientations $\theta_0 = 0°$ at three levels of engineering strains : (a) $\epsilon^{eng} = 0.05$, (b) $\epsilon^{eng} = 0.1$ and (c) $\epsilon^{eng} = 0.15$.
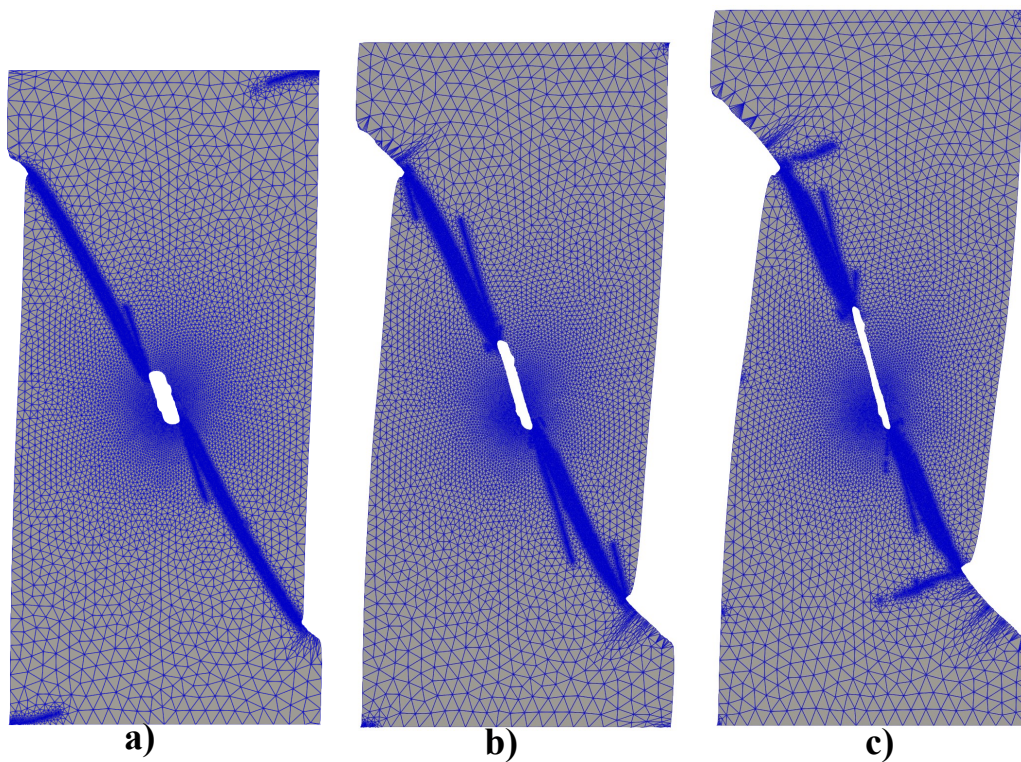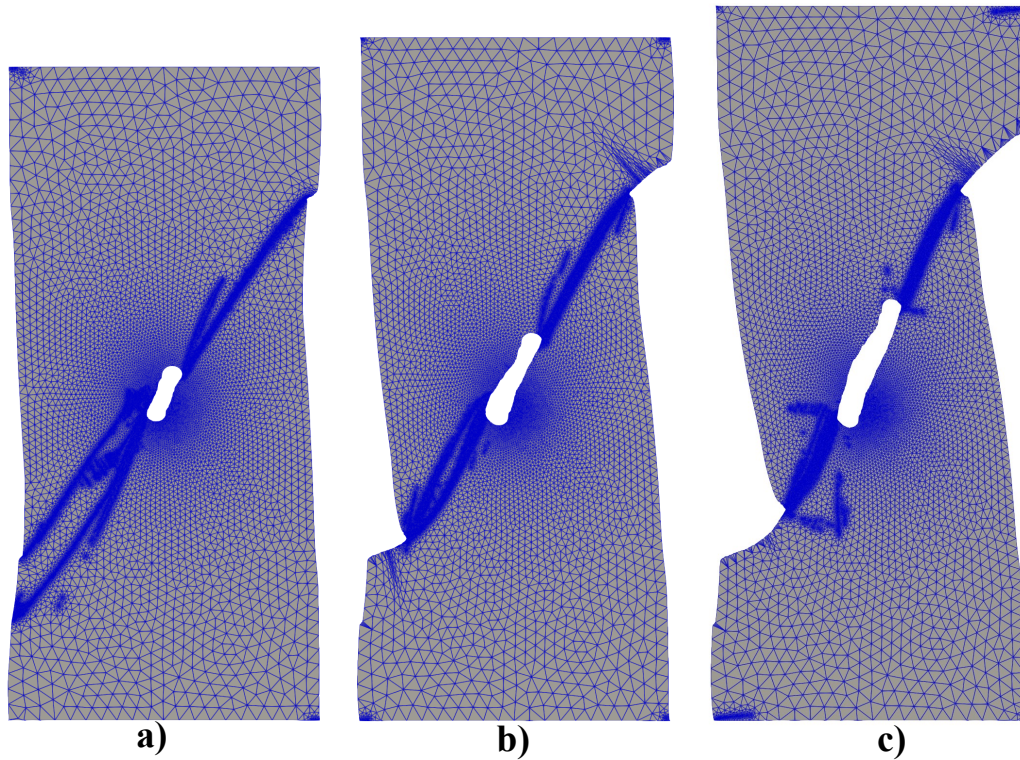

Figure 8.6: Adaptive meshing evolution of a FCC porous micropillar under tensile loading with initial crystallographic orientations $\theta_0 = \frac{54.7°}{2}$ at three levels of engineering strains : (a) $\epsilon^{eng} = 0.05$, (b) $\epsilon^{eng} = 0.1$ and (c) $\epsilon^{eng} = 0.15$.

Figure 8.7: Adaptive meshing evolution of a FCC porous micropillar under tensile loading with initial crystallographic orientations $\theta_0 = 65°$ at three levels of engineering strains : (a) $\epsilon^{eng} = 0.05$, (b) $\epsilon^{eng} = 0.1$ and (c) $\epsilon^{eng} = 0.15$.
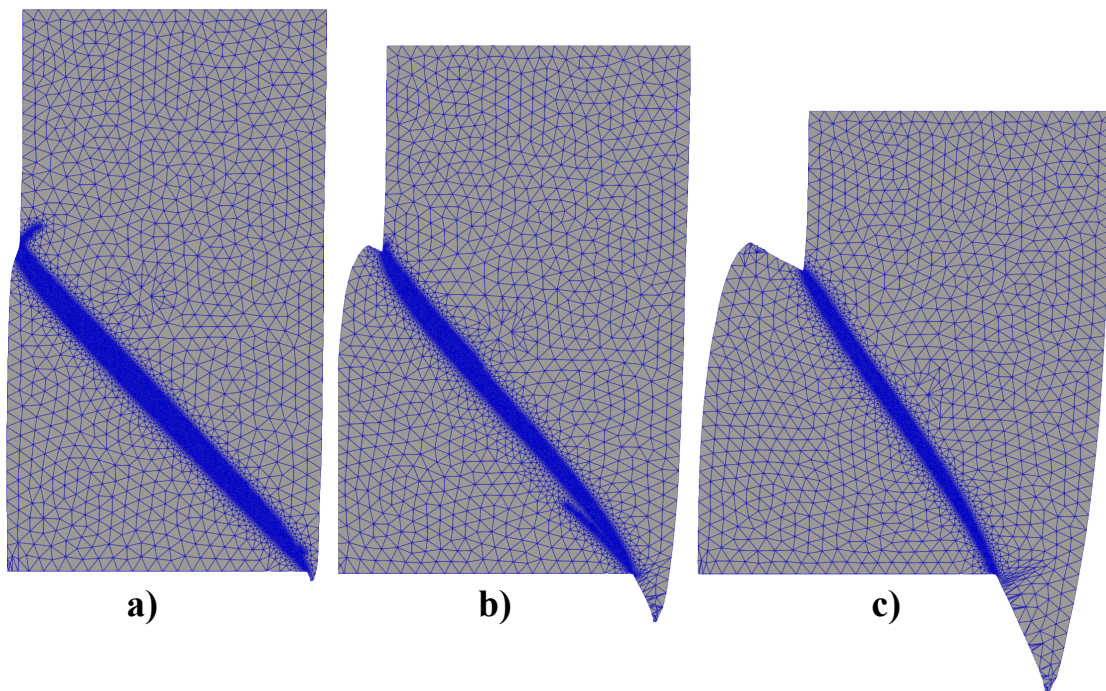

Figure 8.8: 2D Eulerian FE computation of the shear band localization in an elastic-perfectly plastic pillar, see Chapter 6. Evolution for different values of ϵ^{eng}: 5.5% in (a), 11% in (b) and 22% in (c).